

1 **Using BGC-Argo floats for the assessment of marine biogeochemical**  
2 **models: a case study with CMEMS global forecast system**

3  
4 Alexandre Mignot<sup>1</sup>, Hervé Claustre<sup>2,3</sup>, Gianpiero Cossarini<sup>4</sup>, Fabrizio D’Ortenzio<sup>2,3</sup>, Elodie  
5 Gutknecht<sup>1</sup>, Julien Lamouroux<sup>1</sup>, Paolo Lazzari<sup>4</sup>, Coralie Perruche<sup>1</sup>, Stefano Salon<sup>4</sup>, Raphaelle  
6 Sauzède<sup>3</sup>, Vincent Taillandier<sup>2,3</sup>, Anna Teruzzi<sup>4</sup>

7  
8 <sup>1</sup>Mercator Océan International, Toulouse, France  
9 <sup>2</sup>Laboratoire d’Océanographie de Villefranche-sur-Mer, Villefranche-sur-Mer, CNRS and  
10 Sorbonne Université, 06230 Villefranche-sur-Mer, France  
11 <sup>3</sup>Institut de la Mer de Villefranche, CNRS and Sorbonne Université, 06230 Villefranche-sur-  
12 Mer, France  
13 <sup>4</sup>National Institute of Oceanography and Applied Geophysics - OGS, Trieste, Italy

14  
15  
16 Numerical models of ocean biogeochemistry are becoming a major tool to detect and predict  
17 the impact of climate change on marine resources and monitor ocean health. Classically, the  
18 validation of such models relies on comparison with surface quantities from satellite (such as  
19 chlorophyll-*a* concentrations), climatologies, or sparse *in situ* data (such as cruises  
20 observations, and permanent fixed oceanic stations). However, these datasets are not fully  
21 suitable to assess how models represent many climate-relevant biogeochemical  
22 processes. These limitations now begin to be overcome with the availability of a large  
23 number of vertical profiles of light, pH, oxygen, nitrate, chlorophyll-*a* concentrations and  
24 particulate backscattering acquired by the Biogeochemical-Argo (BGC-Argo) floats network.  
25 Additionally, other key biogeochemical variables such as dissolved inorganic carbon and  
26 alkalinity, not measured by floats, can be predicted by machine learning-based methods  
27 applied to float oxygen concentrations. Here, we demonstrate the use of the global  
28 array of BGC-Argo floats for the assessment of biogeochemical models through a  
29 concise evaluation of the Copernicus Marine Environment Marine Service (CMEMS) global  
30 forecasting system. We first detail the handling of the BGC-Argo data set for model  
31 assessment purposes, then we present 22 assessment metrics to quantify the consistency of  
32 BGC model simulations with respect to BGC-Argo data. The metrics evaluate either the  
33 model state accuracy or the skill of the model in capturing emergent properties, such as the

- Deleted: Defining
- Formatted: Font colour: Text 1
- Deleted: -based metrics
- Formatted: Font colour: Text 1
- Deleted: ocean health and
- Formatted: Font colour: Text 1
- Deleted: functioning for the evaluation of
- Formatted: Font colour: Text 1
- Deleted: ocean models
- Formatted: Font colour: Text 1
- Deleted: ¶
- Formatted: Font colour: Text 1
- Deleted: Ramonville-Saint-Agne
- Formatted: Font colour: Text 1
- Deleted: Science-
- Formatted: Font colour: Text 1
- Formatted: Font colour: Text 1
- Deleted:
- Formatted: Font colour: Text 1
- Deleted:
- Formatted: Font colour: Text 1
- Deleted:
- Formatted: Font colour: Text 1
- Deleted: validation
- Formatted: Font colour: Text 1
- Deleted: at
- Formatted: Indent: First line: 0 cm, Don't adjust space between Latin and Asian text, Don't adjust space between Asian text and numbers
- Formatted: Font colour: Text 1
- Formatted: Font colour: Text 1
- Deleted: scale.
- Formatted: Font colour: Text 1
- Formatted: Font colour: Text 1
- Deleted: 18 key
- Formatted: Font colour: Text 1
- Deleted: of ocean health and biogeochemical functioning
- Formatted: Font colour: Text 1
- Deleted: success
- Formatted: Font colour: Text 1
- Deleted: .

1 Deep Chlorophyll Maximums (DCMs) or Oxygen Minimum Zones (OMZs). These metrics  
2 are associated with the air-sea CO<sub>2</sub> flux, the biological carbon pump, and the oceanic pH, and  
3 oxygen levels. We also suggest four diagnostic plots for displaying such metrics.

## 4 1. Introduction

7 Since pre-industrial times, the ocean had taken up ~36 % of the CO<sub>2</sub> emitted by the  
8 combustion of fossil fuel (Friedlingstein et al., 2019), leading to dramatic change in the  
9 ocean's biogeochemical (BGC) cycles, such as ocean acidification (Iida et al., 2020).  
10 Moreover, deoxygenation (Breitburg et al., 2018), and change in the biological carbon pump  
11 are now manifesting on a global scale (Capuzzo et al., 2018; Osman et al., 2019; Roxy et al.,  
12 2016). Together with plastic pollution (Eriksen et al., 2014) and an increase in fisheries  
13 pressure (Crowder et al., 2008), major changes are therefore occurring in marine ecosystems  
14 at the global scale. In order to monitor these ongoing changes, derive climate projections and  
15 develop better mitigation strategies, realistic numerical simulations of the oceans' BGC state  
16 are required.

18 Numerical models of ocean biogeochemistry represent a prime tool to address these issues  
19 because they produce three dimensional estimates of a large number of chemical and  
20 biological variables that are dynamically consistent with the ocean circulation (Fennel et al.,  
21 2019). They can assess past and current states of the biogeochemical ocean, produce short-  
22 term to seasonal forecasts as well as climate projections. However, these models are far from  
23 being flawless, mostly because there are still huge knowledge gaps in the understanding of  
24 key biogeochemical processes and, as a result, the mathematical functions that describe BGC  
25 fluxes and ecosystems dynamics are too simplistic (Schartau et al., 2017). For instance, most  
26 models do not include a radiative component for the penetration of solar radiation in the  
27 ocean. It has been nevertheless shown that coupling such a component with a BGC model  
28 improves the representation of the dynamics of phytoplankton in the lower euphotic zone  
29 (Dutkiewicz et al., 2015). Additionally, the parameterisation of the mathematical functions  
30 generally results from laboratory experiments on few *a priori* expected representative species  
31 and may not be suitable for extrapolation to ocean simulations that need to represent the large  
32 range of organisms present in oceanic ecosystems (Schartau et al., 2017; Ward et al., 2010).  
33 Furthermore, the assimilation of physical data in coupled physical-BGC models that improves

- Formatted: Font colour: Text 1
- Formatted: Font: 7 pt, Font colour: Text 1, Not Superscript/ Subscript
- Deleted: ,
- Formatted: Font: 7 pt, Font colour: Text 1
- Formatted: Font colour: Text 1
- Formatted: Font colour: Text 1
- Formatted: Font colour: Text 1
- Deleted: and Oxygen Minimum Zones (OMZs). The metrics are either a depth-averaged quantity or correspond to the depth of a particular feature
- Formatted: Font colour: Text 1
- Formatted: Indent: First line: 0 cm
- Formatted: Font colour: Text 1
- Formatted: Font colour: Text 1
- Formatted: Font colour: Text 1
- Formatted: Font colour: Text 1
- Formatted: Font colour: Text 1
- Formatted: Font colour: Text 1
- Formatted: Font colour: Text 1
- Formatted: Font colour: Text 1
- Formatted: Font colour: Text 1
- Formatted: Font colour: Text 1
- Deleted:
- Formatted: Font colour: Text 1
- Formatted: Indent: First line: 0 cm
- Formatted: Font colour: Text 1
- Formatted: Font colour: Text 1
- Deleted:
- Formatted: Font colour: Text 1
- Formatted: Font colour: Text 1
- Formatted: Font colour: Text 1
- Formatted: Font colour: Text 1
- Deleted: result
- Formatted: Font colour: Text 1
- Formatted: Font: Italic, Font colour: Text 1
- Formatted: Font colour: Text 1
- Formatted: Font colour: Text 1
- Formatted: Font colour: Text 1

1 the physical ocean state can paradoxically degrade the simulation of the BGC state of the  
2 ocean (Fennel et al., 2019; Park et al., 2018; Gasparin et al., 2021). A rigorous validation of  
3 BGC models is thus essential to test their predictive skills, their ability to reproduce BGC  
4 processes and estimate confidence intervals on model predictions (Doney et al., 2009; Stow et  
5 al., 2009).

Deleted: (Fennel et al., 2019; Park et al., 2018).

Formatted: Font colour: Text 1

Formatted: Font colour: Text 1

Formatted: Font colour: Text 1

6  
7 However, the validation of BGC models is presently limited by the availability of data. It  
8 relies principally on comparison with surface quantities from satellite (such as chlorophyll-*a*  
9 concentrations), cruises observations, and few permanent oceanic stations (e.g., Doney et al.,  
10 2009; Dutkiewicz et al., 2015; Lazzari et al., 2012, 2016; Lynch et al., 2009; Séférian et al.,  
11 2013; Stow et al., 2009). All these datasets neither have a sufficient vertical or temporal  
12 resolution, nor a synoptic view, nor can provide all variables necessary to evaluate how  
13 models represent climate-relevant processes such as the air-sea CO<sub>2</sub> fluxes, the biological  
14 carbon pump, ocean acidification or deoxygenation.

Formatted: Indent: First line: 0 cm

Formatted: Font colour: Text 1

Formatted: Font colour: Text 1

Formatted: Font colour: Text 1

15  
16 In 2016, the Biogeochemical-Argo (BGC-Argo) program was launched with the goal to  
17 operate a global array of 1000 BGC-Argo floats equipped with oxygen (O<sub>2</sub>), chlorophyll *a*  
18 (Chl*a*) and nitrate (NO<sub>3</sub>) concentrations, particulate backscattering (b<sub>bp</sub>), pH and downwelling  
19 irradiance sensors (Biogeochemical-Argo Planning Group, 2016; Claustre et al., 2020).

Deleted: -

Formatted: Font colour: Text 1

Formatted: Font colour: Text 1

Formatted: Font colour: Text 1

Deleted: ;

Formatted: Font colour: Text 1

Deleted:

Formatted: Font colour: Text 1

Formatted: Font colour: Text 1

Formatted: Font colour: Text 1

Formatted: Font colour: Text 1

Formatted: Font colour: Text 1

Deleted: have

Formatted: Font colour: Text 1

Deleted: an unprecedented temporal and vertical resolution of key variables acquired simultaneously as well as

Formatted: Font colour: Text 1

Formatted: Font colour: Text 1

Formatted: Font colour: Text 1

Deleted:

Formatted: Font colour: Text 1

Formatted: Font colour: Text 1

Formatted: Font colour: Text 1

Deleted: ,

Formatted: Font colour: Text 1

Deleted:

20 Although the planned number of 1000 floats has not been reached yet, the BGC-Argo  
21 program has already provided a large number of quality-controlled vertical profiles of O<sub>2</sub>,  
22 Chl*a*, NO<sub>3</sub>, b<sub>bp</sub>, and pH (Fig. 1). With respect to O<sub>2</sub>, Chl*a*, NO<sub>3</sub>, and b<sub>bp</sub>, the North Atlantic  
23 and the Southern Ocean are reasonably well sampled whereas pH is so far essentially sampled  
24 in the Southern Ocean. At regional scale, the Mediterranean Sea is also fairly well sampled by  
25 BGC-Argo floats (Salon et al., 2019; Terzić et al., 2019). However, there are still, large  
26 under-sampled areas, like the subtropical gyres or the sub-polar North Pacific. Nevertheless,  
27 the number of quality-controlled observations collected by the BGC-Argo fleet is already  
28 greater than any other data set (Claustre et al., 2020). The BGC-Argo data also have a  
29 satisfactory level of accuracy and stability over time (Johnson et al., 2017; Mignot et al.,  
30 2019). Thanks to machine learning based methods (Bittig et al., 2018; Sauzède et al., 2017),  
31 floats equipped with O<sub>2</sub> sensors can be additionally used to derive vertical profiles of NO<sub>3</sub>,  
32 phosphate (PO<sub>4</sub>), silicate (Si), alkalinity (Alk), dissolved inorganic carbon (DIC), pH and  
33 pCO<sub>2</sub>. All these specificities overcome the limitations of previous data sets, in terms of

1 vertical and temporal resolution, from now and open new perspectives for the validation of  
2 BGC models (Gutknecht et al., 2019; Salon et al., 2019; Terzić et al., 2019).

3  
4 The BGC-Argo data set represent a significant improvement for the assessment of models  
5 comparing to large databases such as the World Ocean Atlas (WOA) or the World Ocean  
6 Database (WOD). One of the issues of large databases such as WOD is the interoperability of  
7 the data that compose it, which, ultimately, affects their overall accuracy (Snowden et al.,  
8 2019). Using the BGC-Argo dataset separately is a way to ensure consistent accuracy as it is  
9 an interoperable homogenous data set with strict data QC procedures. The BGC-Argo floats  
10 also provide observations at high vertical and temporal resolutions and for long periods of  
11 time providing nearly continuous time series of the vertical distribution of a number of  
12 biogeochemical variables. This is not possible with discrete vertical samplings provided by  
13 cruise cast *in situ* measurements or from climatological values derived from the WOA.

14  
15 We aim to demonstrate the use of the BGC-Argo global array for the assessment of BGC  
16 models at the global scale. To that end, we performed a concise evaluation of Copernicus  
17 Marine Environment Marine Service (CMEMS) global BGC forecasting system using the  
18 global fleet of BGC-Argo floats. We expect that the methodology employed here (from the  
19 data handling to the use of assessment metrics) would be useful and informative for other  
20 research teams interested in model evaluation with BGC-Argo floats. In this study, the BGC-  
21 Argo dataset is used in conjunction with the model evaluation framework developed by  
22 Hipsey et al. (2020). In particular, they propose three levels of assessment metrics to evaluate  
23 the skill of a model simulation: state variables validation (e.g., Chl $a$ , NO $_3$ , O $_2$ , etc...), mass  
24 fluxes and process rates validation (e.g., primary production or division rates), and emergent  
25 properties validation (e.g., deep chlorophyll maximum, or oxygen minimum zones). In this  
26 study we present 22 metrics for the assessment of a model simulation with BGC-Argo data.  
27 Most of them evaluate the model state accuracy through the comparison of simulated state  
28 variables with BGC-Argo observations in the mixed layer or at fixed depth. In addition, some  
29 of the metrics assess the skill of the model in capturing emergent properties. These metrics are  
30 associated with the air-sea CO $_2$  flux, the biological carbon pump, the oceanic pH, and oxygen  
31 levels and Oxygen Minimum Zones (OMZs). Further, our validation framework could, in  
32 principle, include the second level of assessment metrics (i.e., flux and process). Indeed,  
33 recent works demonstrated the feasibility of calculation at basin scale, from BGC-Argo  
34 observations, of mass fluxes and process rates, such as primary production, phytoplankton

Formatted: Font colour: Text 1

Formatted: Font colour: Text 1

Formatted: Font colour: Text 1

**Deleted:** We aim to demonstrate the use of the BGC-Argo global array for the validation of BGC models at the global scale. In regional seas or enclosed basins, where a limited number of floats have been so far deployed, point-by-point model-observation comparison is possible (Gutknecht et al., 2019; Salon et al., 2019). However, at the global scale, the BGC-Argo dataset provides a massive and ever-growing amount of data, and it can be difficult to manipulate this large data set, especially when it comes to evaluate a 3-D time-varying model simulation for about ten variables. In such cases, it is useful to define observationally-based metrics that are able to quantify the skill of a model to represent key oceanic processes (Russell et al., 2018). These metrics are quantities that summarize a particular process into a single number [e.g., the amplitude or the depth of an Oxygen Minimum Zone (OMZ)]. In this study, we present 18 metrics of ocean health and biogeochemical functioning for the assessment of a BGC model simulation. The metrics are either a depth-averaged quantity (e.g. nutrients concentration, Chl $a$ , ...) or correspond to the depth of a particular feature (e.g., nitracline). These metrics are associated with the air-sea CO $_2$  flux, the biological carbon pump, oceanic pH, oxygen levels and Oxygen Minimum Zones (OMZs).<sup>¶</sup>

<sup>¶</sup> The paper is organised as follow: section 2 presents the data sets used in the study. In section 3, we define the metrics necessary to compare the model to floats' observations. In section 4, we show examples of diagnostic plots for displaying the metrics. In section 5, we discuss metrics relative to optical properties in the water column. Finally, section 6 summarizes and concludes the study.<sup>¶</sup>

**Data**<sup>¶</sup>

**BGC-Argo floats observations**<sup>¶</sup>

<sup>¶</sup> The float data were downloaded from the Argo Coriolis Global Data Assembly Centre in France (<ftp://ftp.ifremer.fr/argo>). The CTD and trajectory data were quality controlled using the standard Argo protocol (Wong et al., 2015). The raw BGC signals were transformed to biogeochemical variables and quality-controlled according to international BGC-Argo protocols (Johnson et al., 2018b, 2018a; Schmechtig et al., 2015, 2018; Thierry et al., 2018; Thierry and Bittig, 2018).<sup>¶</sup>

1 division and accumulation rates (Yang et al., 2021; Mignot et al., 2018), net community  
2 production (Plant et al., 2016), and carbon export (Dall’Olmo and Mork, 2014). However, it  
3 would be arduous to achieve such estimations on the global BGC-Argo dataset as it requires  
4 *ad hoc* calibration that cannot be easily defined. Consequently, the evaluation of simulated  
5 process rates with BGC-Argo data is not addressed in this study.

6  
7 The paper is organised as follow: section 2 presents the data sets used in the study. In section  
8 3, we define the metrics necessary to compare the model to floats’ observations. In section 4,  
9 we show examples of diagnostic plots for displaying the metrics. In section 5, we discuss  
10 metrics relative to optical properties in the water column. Finally, section 6 summarizes and  
11 concludes the study.

## 12 2. Data

### 13 a. BGC-Argo floats observations

14  
15 The float data were downloaded from the Argo Coriolis Global Data Assembly Centre in  
16 France (<ftp://ftp.ifremer.fr/argo>). The CTD and trajectory data were quality controlled using  
17 the standard Argo protocol (Wong et al., 2015). The raw BGC signals were transformed to  
18 biogeochemical variables (i.e., O<sub>2</sub>, Chl<sub>a</sub>, NO<sub>3</sub>, b<sub>bp</sub>, and pH) and quality-controlled according  
19 to international BGC-Argo protocols (Johnson et al., 2018b, a; Schmechtig et al., 2015, 2018;  
20 Thierry et al., 2018; Thierry and Bittig, 2018).

21  
22 In the Argo data-system, the data are available in three data modes: “Real-Time”, “Adjusted”  
23 and “Delayed” (Bittig et al., 2019). In the “Real-time” mode, the raw data are converted into  
24 state variable and an automatic quality-control is applied to “flag” gross outliers. In the  
25 “Adjusted” mode, the “Real-time” data receive a calibration adjustment in an automated  
26 manner. In the “Delayed” mode, the “Adjusted” data are adjusted and validated by a scientific  
27 expert. While the “Real-Time” and “Adjusted” data are considered acceptable for operational  
28 application (data assimilation), the “Delayed” mode” is designed for scientific exploitation  
29 and represent the highest quality of data with the ultimate goal, when time-series with  
30 sufficient duration will have been acquired, to possibly extract climate-related trends.  
31 However, for some variables, only a limited fraction of data is accessible in “Delayed-Mode”.

Formatted: Font colour: Text 1

Formatted: Font colour: Text 1

Formatted: Indent: First line: 0 cm, Don't adjust space between Latin and Asian text, Don't adjust space between Asian text and numbers

Deleted: ,

Formatted: Font colour: Text 1

Formatted: Font colour: Text 1

Deleted: has been

Formatted: Font colour: Text 1

Deleted: trend

Formatted: Font colour: Text 1

Deleted: parameters

Formatted: Font colour: Text 1

1 Consequently, for each variable, we selected the highest data modes, where at least 80 % of  
2 the data are available (see Table 1). Note that this criterion does not apply to O<sub>2</sub>, where only  
3 delayed mode data were selected in order to generate the pseudo-observations from  
4 CANYON-B neural network (see after). We removed data with missing location or time  
5 information and flagged as “Bad data” (flag =4). Depending on the parameter and the  
6 associated data mode, we also excluded data flagged as “potentially bad data” (flag=3) (see  
7 Table 1).

8  
9 Particulate Organic Carbon (POC) concentrations were derived from b<sub>bp</sub> observations. First,  
10 three consecutive low-pass filters were applied on the vertical profiles of b<sub>bp</sub> to remove  
11 spikes (Briggs et al., 2011); a 2-points running median followed by a 5-points running  
12 minimum and 5-points running maximum. Then, the filtered b<sub>bp</sub> profiles were converted into  
13 POC using a POC vs b<sub>bp</sub> relationship developed for the global ocean  
14 (<https://catalogue.marine.copernicus.eu/documents/QUID/CMEMS-MOB-QUID-015-010.pdf>) based on a global database of *in situ* POC and satellite b<sub>bp</sub> (Evers-King et al., 2017).  
15 This relationship,  $POC = 38687.27 * b_{bp}^{0.95}$ , developed for global applications, has been  
16 shown to outperform regional relationships, applied at global scales. Negative values resulting  
17 from this transformation were set to 0.

18  
19  
20 Finally, we complemented the existing BGC-Argo dataset with pseudo-observations of NO<sub>3</sub>,  
21 PO<sub>4</sub>, Si, and DIC concentrations as well as pH and pCO<sub>2</sub> using the CANYON-B neural  
22 network (Bittig et al., 2018). CANYON-B estimates vertical profiles of nutrients as well as  
23 the carbonate system variables from concomitant measurements of floats pressure,  
24 temperature, salinity and O<sub>2</sub> qualified in “Delayed” mode together with the associated  
25 geolocalization and date of sampling. The CANYON-B estimates of NO<sub>3</sub> and pH were  
26 merged with measured values on the rationale that CANYON-B estimates have RMS errors ( $NO_3 = 0.7 \mu mol kg^{-1}$ ,  $pH = 0.013$ ) (Bittig et al., 2018) that are of the same order of  
27 magnitude as those of the BGC-Argo observations errors ( $NO_3 = 0.5 \mu mol kg^{-1}$ ,  $pH = 0.07$ )  
28 (Mignot et al., 2019; Johnson et al., 2017).

29  
30  
31 Finally, we verified that the RMS errors of BGC-Argo data (both measured and from  
32 CANYON-B estimates) are lower than the RMS difference between the model and BGC-  
33 Argo data, so that the comparison of simulated properties with the BGC-Argo data leads to a  
34 meaningful evaluation of the model performance. We believe it is reasonable to draw

Deleted: parameter  
Formatted: Font colour: Text 1  
Deleted: quality of  
Formatted: Font colour: Text 1  
Deleted: that did not compromise too much  
Formatted: Font colour: Text 1  
Deleted: number of observations  
Formatted: Font colour: Text 1  
Formatted: Font colour: Text 1

Formatted: Indent: First line: 0 cm

Formatted: Indent: First line: 0 cm, Don't adjust space between Latin and Asian text, Don't adjust space between Asian text and numbers

Formatted: Font colour: Text 1

Formatted: Font colour: Text 1

Deleted: Then, the filtered b<sub>bp</sub> profiles were converted into POC using the relationship proposed by Cetinic et al. (2012), i.e.,  $POC = 35422 * b_{bp}^{-14.4}$ .

Formatted: Font colour: Text 1

Deleted: Finally, we complemented the existing BGC-Argo dataset with pseudo-observations of NO<sub>3</sub>, PO<sub>4</sub>, Si, and DIC concentrations as well as pH and pCO<sub>2</sub> using the CANYON-B neural network (Bittig et al., 2018). CANYON-B estimates vertical profiles of nutrients as well as the carbonate system variables from concomitant measurements of floats pressure, temperature, salinity and O<sub>2</sub> qualified in “Delayed” mode together with the associated geolocation and date of sampling.

1 conclusions on the model uncertainty from BGC-Argo data as long as the BGC-Argo errors  
2 are much lower than the model-observations RMS difference.

3 ▲  
4  
5 **b. CMEMS global BGC Model**  
6

7 The global model simulation used in this study (see Appendix A.1) originates from the Global  
8 Ocean hydrodynamic-biogeochemical model, implemented and operated by the Global  
9 Monitoring and Forecasting Center of the EU, the Copernicus Marine Environment  
10 Monitoring Service (CMEMS). It is based on the coupled NEMO–PISCES model and it is  
11 constrained by the assimilation of satellite Chla concentrations. The BGC model is forced  
12 offline by daily fields of ocean, sea ice and atmosphere. The ocean and sea ice forcing come  
13 from Mercator Ocean global high-resolution ocean model (Lellouche et al., 2018) that  
14 assimilates along-track altimeter data, satellite Sea Surface Temperature and Sea-Ice  
15 Concentration, and *in situ* temperature and salinity vertical profiles. The BGC model has a  
16 1/4° horizontal resolution, 50 vertical levels (with 22 levels in the upper 100 m, the vertical  
17 resolution is 1 m near the surface and decreases to 450 m resolution near the bottom). It  
18 produces daily outputs of Chla, NO<sub>3</sub>, PO<sub>4</sub>, Si, O<sub>2</sub>, pH, DIC and Alk, and weekly outputs of  
19 POC (resampled offline from weekly to daily frequency through linear interpolation) from  
20 2009 to 2017. Note that the method of linear resampling, while artificially increasing the  
21 number of data, could potentially bias the statistical results, especially in regions with poor  
22 data coverage. Following the approach of Gali et al. (2021), the POC simulated by the model  
23 corresponds to the sum of the two sizes classes of phytoplankton, the small detrital particles  
24 and microzooplankton modelled by PISCES. This particular combination of phytoplanktonic  
25 and non-phytoplanktonic organisms has been shown match the small POC observed by the  
26 floats (Gali et al., 2021). Partial pressures of CO<sub>2</sub> values are calculated offline from the  
27 modelled DIC, Alk, temperature and salinity data using the seacarb program for R  
28 (<https://CRAN.R-project.org/package=seacarb>). The Black Sea was not considered in the  
29 present analysis because the model solutions are of very poor qualities. Finally, the daily  
30 model outputs were collocated in time and the closest to the BGC-Argo floats positions, and  
31 they were interpolated to the sampling depth of the float observations. The characteristics of  
32 the model are further detailed in the appendix.  
33

Formatted: Font colour: Text 1

Formatted: Indent: First line: 0 cm

Formatted: Font colour: Text 1

Formatted: Font colour: Text 1

Deleted: 1m

Formatted: Font colour: Text 1

Deleted: 450m

Formatted: Font colour: Text 1

Deleted: The POC model used in this study corresponds to the sum two size classes of particulate organic matter modelled by PISCES (Aumont et al., 2015).

Formatted: Font colour: Text 1, English (US)

Formatted: Font colour: Text 1, English (US)

Formatted: Font colour: Text 1, English (US)

Formatted: Font colour: Text 1, English (US)

Formatted: Font colour: Text 1

Deleted: taken into account

Formatted: Font colour: Text 1

### 3. Metrics

In this section, we present 22 metrics for the assessment of a model simulation with BGC-Argo data. The metrics are associated with the air-sea CO<sub>2</sub> flux, the biological carbon pump, oceanic pH, oxygen levels and Oxygen minimum zones (OMZs). The metrics are described below and summarized in Table 2.

#### a. Air-sea CO<sub>2</sub> flux

The air-sea CO<sub>2</sub> flux is generally calculated following a bulk formulation (Wanninkhof, 2014),  $F_{CO_2} = k\alpha(p_{CO_2atm} - sp_{CO_2})$ , where  $F_{CO_2}$  is the air-sea CO<sub>2</sub> flux,  $\alpha$  is the CO<sub>2</sub> solubility in seawater,  $k$  is a gas transfer coefficient that depends on wind speed,  $sp_{CO_2}$  is the partial pressure of CO<sub>2</sub> at the ocean's surface, and  $p_{CO_2atm}$  is the partial pressure of CO<sub>2</sub> in the atmosphere. Among the uncertainties affecting the different components of the model CO<sub>2</sub> flux, BGC-Argo data can contribute to estimate that on  $sp_{CO_2}$ . Thus, the validation of  $p_{CO_2}$  plays a critical role to assess the skill of a BGC model in representing correctly the air-sea CO<sub>2</sub> flux.

Here,  $sp_{CO_2}$  is defined as the average of  $p_{CO_2}$  profile between the surface and the mixed layer depth (MLD). Following De Boyer et al. (2004), the MLD is computed as the depth at which the change in potential density from its value at 10 m exceeded 0.03 kg m<sup>-3</sup>. We verified that the MLD is correctly represented in the model -- the global bias between the model and the BGC-Argo observations is 0.3 m.

#### b. Oceanic pH

Ocean acidification is the decrease in oceanic pH due to the absorption of anthropogenic CO<sub>2</sub>. The acidification of the ocean is expected to impact primarily the surface oceanic waters as well as the 200-400 m layer (Kwiatkowski et al., 2020). Assessing how models correctly represent oceanic pH at the surface and in the 200-400 m layer is therefore critical if we aim to derive accurate climate projections on acidification. The surface ocean pH (spH) is defined

Deleted: 18 key  
Formatted: Indent: First line: 0 cm  
Formatted: Font colour: Text 1  
Deleted: ocean health and biogeochemical functioning  
Formatted: Font colour: Text 1  
Formatted: Font colour: Text 1

Formatted: Font colour: Text 1  
Formatted: Indent: First line: 0 cm  
Formatted: Font colour: Text 1  
Deleted: =  
Formatted: Font colour: Text 1  
Deleted:  $\alpha$ (  
Formatted: Font colour: Text 1  
Deleted:  $\alpha$   
Formatted: Font colour: Text 1  
Deleted:  
Formatted: Font colour: Text 1

Formatted: Indent: First line: 0 cm

Formatted: Font colour: Text 1

Formatted: Indent: First line: 0 cm

Formatted: Font colour: Text 1  
Formatted: Font colour: Text 1  
Formatted: Font colour: Text 1



1 as the average of pH profile between the surface and the base of the mixed layer and the pH in  
2 the 200-400 m layer (pH<sub>200-400</sub>) as the average of pH profile in this layer.

### 3 4 **c. Biological carbon pump**

5  
6 The biological carbon pump is the transformation of nutrients and dissolved inorganic carbon  
7 into organic carbon in the upper part of the ocean through phytoplankton photosynthesis and  
8 ~~the~~ subsequent transfer of this organic material into the deep ocean. The functioning of this  
9 pump relies on key pools of nutrients and carbon as well as several processes that control  
10 mass fluxes between the pools.

11  
12 The first level of assessment of a biological carbon pump simulated by a model consists in  
13 evaluating the different pools (or state variables) of the pump (Hipsey et al., 2020). In  
14 particular, the comparison of simulated surface nutrients (NO<sub>3</sub>, PO<sub>4</sub>, and Si), DIC, Chl<sub>a</sub> and  
15 POC with BGC-Argo observations gives an indirect evaluation of the model capability to  
16 capture key processes of the biological carbon pump in the ocean upper layer, such as primary  
17 production, respiration, and grazing. A second level assessment would be to directly compare  
18 these key processes with measured mass fluxes, but this assessment level is not addressed in  
19 this study. The surface nutrients, DIC, Chl<sub>a</sub> and POC (hereinafter denoted sNO<sub>3</sub>, sPO<sub>4</sub>, sSi,  
20 sDIC, sChl and sPOC) are calculated as the average concentrations in the mixed layer.

21  
22 Similarly, the assessment of the mesopelagic nutrients, DIC and POC concentration  
23 (hereinafter indicated with the subscript <sub>meso</sub>) provides an indirect evaluation of the key  
24 mesopelagic layer processes, such as export production, respiration, etc. The mesopelagic  
25 concentrations are calculated as the depth-averaged concentrations between the base of the  
26 mixed layer down to 1000 m.

27  
28 In stratified systems, a Chl<sub>a</sub> maximum (hereinafter denoted Deep Chlorophyll Maximum,  
29 DCM) is formed at the base of the euphotic layer (Barbieux et al., 2019; Cullen, 2015;  
30 Letelier et al., 2004; Mignot et al., 2014, 2011). It has been suggested that the DCM plays an  
31 important role in the synthesis of organic carbon by phytoplankton (Macías et al., 2014).  
32 DCMs are therefore important features to be assessed in BGC models with respect to  
33 processes involved in the biological carbon pump processes such as the primary production.

Formatted: Font colour: Text 1

Formatted: Indent: First line: 0 cm

Deleted: its

Formatted: Font colour: Text 1

Formatted: Font colour: Text 1

Deleted: A useful way to investigate the biological carbon pump is to look at the depth-averaged concentrations in nutrients (NO<sub>3</sub>, PO<sub>4</sub>, and Si), DIC, Chl<sub>a</sub> and POC computed from the surface down to the MLD, hereinafter denoted sNO<sub>3</sub>, sPO<sub>4</sub>, sSi, sDIC, sChl and sPOC. To assess the quantity of POC that is exported to the deep ocean, we compute the mesopelagic POC concentration (POC<sub>meso</sub>), which correspond to the depth-averaged POC concentrations between the base of the mixed layer down to 1000 m (Dall’Omo and Mork, 2014).  
→ At the base of the euphotic layer of

Formatted: Font colour: Text 1

Deleted: develops that generally escapes detection by remote sensing ...

Formatted: Font colour: Text 1

Formatted: Font colour: Text 1

Formatted: Font colour: Text 1

Deleted: . The DCM is therefore an important feature to be assessed in BGC models with respect to the production of organic carbon and more generally to the biological carbon pump. The depth and magnitude of DCM (H<sub>dc</sub> and Chl<sub>dc</sub>) are helpful metrics for the assessment of DCM dynamics. The depth of the DCM is calculated as the depth where the maximum of Chl<sub>a</sub> occurs in the profile with the criterion that H<sub>dc</sub> should be deeper than H. The magnitude of the DCM is computed at the value at H<sub>dc</sub>. Finally, the depth of nitracline (H<sub>nit</sub>) is also evaluated as it is an important driver for H<sub>dc</sub> and Chl<sub>dc</sub> (Barbieux et al., 2019; Herbland and Voituriez, 1979). Following Richardson and Bendtsen (2019), H<sub>nit</sub> was computed at the depth at which NO<sub>3</sub> = 1 μmol kg<sup>-1</sup>.

1 however the DCM layer generally escapes detection by remote sensing. Furthermore, DCM is  
2 also an emergent feature that develops in response to complex physical and biogeochemical  
3 interactions (Cullen, 2015). Thus, its evaluation provides critical information regarding the  
4 accuracy of the model in capturing complex patterns of key ecosystem processes. The depth  
5 and magnitude of DCM ( $H_{\text{dcm}}$  and  $\text{Chl}_{\text{dcm}}$ ) are helpful metrics for the assessment of DCM  
6 dynamics. The depth of the DCM is calculated as the depth where the maximum of  $\text{Chl}_a$   
7 occurs in the profile with the criterion that  $H_{\text{dcm}}$  should be deeper than the MLD. The  
8 magnitude of the DCM is computed at the value at  $H_{\text{dcm}}$ .

9  
10 The vertical supply of  $\text{NO}_3$  to the surface layers is a critical process of the biological carbon  
11 pump as  $\text{NO}_3$  is often depleted in the surface layers and is a limiting factor for phytoplankton  
12 growth in most oceanic regions. This  $\text{NO}_3$  vertical supply depends, among other factors, on  
13 the vertical gradient of  $\text{NO}_3$  (the nitracline), and, in particular, on its depth (the nitracline  
14 depth) (Cermeno et al., 2008; Omand and Mahadevan, 2015). Therefore, the comparison of  
15 the simulated nitracline depth with BGC-Argo observations allows for an indirect assessment  
16 of the model quality in reproducing vertical fluxes of  $\text{NO}_3$ . Following previous studies  
17 (Cermeno et al., 2008; Lavigne et al., 2013; Richardson and Bendtsen, 2019), the depth of the  
18 nitracline corresponds to the first depth where  $\text{NO}_3$  is detected. The detection threshold is set  
19 to  $1 \mu\text{mol kg}^{-1}$ , which corresponds to an upper estimate of BGC-Argo  $\text{NO}_3$  data accuracy  
20 (Johnson et al., 2017; Mignot et al., 2019).

#### 21 22 **d. Oxygen levels and oxygen minimum zones**

23  
24 Oxygens levels in the global and coastal waters have declined over the whole water column  
25 over the past decades (Schmidtko et al., 2017) and OMZs are expanding (Stramma et al.,  
26 2008). Assessing how models correctly represent ocean oxygen levels as well as the OMZs is  
27 therefore critical to monitor their change over time. Similarly to DCMs, the assessment of  
28 OMZs is also informative on how the model simulates emergent dynamics as OMZs originate  
29 from complex physical and biogeochemical interactions (Paulmier and Ruiz-Pino, 2009). We  
30 evaluate oxygen levels in 3 layers, at the surface, at 300 m and at 1000 m. The surface  $\text{O}_2$   
31 ( $s\text{O}_2$ ), important for the air-sea  $\text{O}_2$  flux, is defined as the average of  $\text{O}_2$  profile in the mixed  
32 layer. The oxygen at 300 m ( $\text{O}_{2\ 300}$ ), a depth where large areas of the global ocean have very  
33 low  $\text{O}_2$  (Breitburg et al., 2018), is defined as the average of  $\text{O}_2$  profile between 250 and 300

Formatted: Font colour: Text 1

Formatted: Line spacing: single, Don't adjust space between Latin and Asian text, Don't adjust space between Asian text and numbers

Formatted: Indent: First line: 0 cm, Don't adjust space between Latin and Asian text, Don't adjust space between Asian text and numbers

Formatted: Font colour: Text 1

Formatted: Font colour: Text 1

Formatted: Font colour: Text 1

Formatted: Font colour: Text 1

Deleted: . We evaluate oxygen levels in 3 layers, at the surface, at 300 m and at 1000 m.

Formatted: Font colour: Text 1

Formatted: Font colour: Text 1

Formatted: Font colour: Text 1

1 m. The deep oxygen content, ( $O_{2\ 1000}$ ), is defined as the average of  $O_2$  profile between 950 and  
2 1000 m. Finally, to characterize the OMZs, we evaluate the depth ( $H_{O_{2min}}$ ) and concentration  
3 ( $O_{2min}$ ) of  $O_2$  minimums.  $O_2$  level lower than  $80\ \mu\text{mol kg}^{-1}$  are used to characterize OMZs  
4 (Schmidtko et al., 2017).

#### 6 4. Diagnostic plots to display the BGC-Argo based metrics

8 Based upon the existing literature (e.g., Aumont et al., 2015; Cossarini et al., 2019; Doney et  
9 al., 2009; Dutkiewicz et al., 2015; Gutknecht et al., 2019; Salon et al., 2019; Séférian et al.,  
10 2013; Terzić et al., 2019), we propose 4 graphical representations that can be used to display  
11 the novel validation metrics and to assess the skill of a model in reproducing a particular  
12 process or variable: Taylor diagrams, scatterplots, spatial maps, and time series.

##### 14 a. Taylor diagram

16 Taylor diagrams are useful to display simultaneously information on model-data skill for a  
17 suite of metrics (Taylor, 2001). These diagrams combine the Pearson correlation coefficient  
18 ( $r$ ), root-mean-square difference (RMSD) and the model standard deviation (SD). In order to  
19 represent all metrics with different units into a single diagram, we use a normalized Taylor  
20 diagram (RMSD and the model SD are divided by the SD of the observations). In the  
21 diagram, the Pearson correlation coefficient between the model and the observations is related  
22 to the azimuthal angle. The normalized SDs are proportional to the radial distances from the  
23 origin. The observational reference is indicated along the x-axis and corresponds to the  
24 normalized SD and  $r=1$ . Finally, the normalized RMSD is proportional to the distance from  
25 the observational difference.

##### 27 b. Scatter/Density plots

29 In validation exercises, scatter plots are useful to identify relationships between the predicted  
30 and observed values. It is common to add a least squares regression line to quantify the  
31 strength of the linear relationship between the observed and predicted values. In those cases,  
32 when a large amount of data points has to be plotted (like in our study), the points overlap to a

Formatted: Font colour: Text 1

Formatted: Font colour: Text 1

Formatted: Font colour: Text 1

Formatted: Indent: First line: 0 cm

Formatted: Font colour: Text 1

Formatted: Indent: First line: 0 cm

Formatted: Font colour: Text 1

Formatted: Font colour: Text 1

Formatted: Indent: First line: 0 cm

Deleted: Scatter plots are also helpful to show other patterns in data, such as non-linear relationships, clusters of points and outliers.

Formatted: Font colour: Text 1

1 degree where it can be difficult to distinguish the relationship between the variables. To  
2 overcome this, scatter plots are displayed as density plots, where each axis is divided in  
3 several bins while the colour within each bin indicates the number of points.

4  
5 **c. Spatial maps**

6  
7 Spatial maps draw attention to the spatial distribution of a given metric. The maps are handy  
8 to determine if the model is skilled in reproducing global patterns, spatial gradients, and  
9 basins inter-difference. It is also helpful to display the BIAS and RMSD between predicted  
10 and observed values on a spatial map to quickly determine regions where the model  
11 uncertainty is the highest. Depending on the context, the comparison between the model and  
12 the observation can be performed either on a climatological level, or for a specific period  
13 (year, month, etc ..). In our case, the scarcity of observations imposes us to display all data  
14 (from 2009 to 2017; the period of analysis of the model simulation) in a climatological way if  
15 we want to highlight large scale patterns. To do so, the metrics from 2009 to 2017 are  
16 averaged in 4°x4° bins, bins excluding those with less than 4 points. The 4° distance is an  
17 upper estimate of the autocorrelation length scales for O<sub>2</sub>, nutrients, and pCO<sub>2</sub> (comprised  
18 between 300 and 400 km) between 20° and 40° of latitude in both hemispheres  
19 (Biogeochemical-Argo Planning Group, 2016). We also computed the BIAS and RMSD  
20 within each bin. Standard deviation can also be displayed on spatial maps as an indicator of  
21 the model skill in properly reproducing variability scales. For clarity, it is not shown in this  
22 study.

23  
24 **d. Seasonal time-series**

25  
26 Taylor diagrams, scatter plots and spatial maps are powerful diagnostics plots to evaluate the  
27 global skills of a model but understanding the causes of difference remains somewhat limited  
28 with these diagrams. Rather, the comparative analysis of seasonal time-series of multiple  
29 metrics and their inter-relationships is a powerful tool to highlight and to understand BGC  
30 processes. This is especially true for the biological carbon pump that has a strong seasonal  
31 variability due to the seasonal variation in sunlight, surface heating and surface wind  
32 (Williams and Follows, 2011). As a matter of fact, the analysis of seasonal dynamics in  
33 nutrients as well as in phyto- and zoo- plankton has a rich history for the development of

Deleted: a number of

Formatted: Font colour: Text 1

Deleted: Spatial maps

Spatial maps draw attention to the spatial distribution of a given metric. The maps are handy to determine if the model is skilled in reproducing global patterns, spatial gradients, and basins inter-difference. It is also helpful to display the BIAS and RMSD between predicted and observed values on a spatial map to quickly determine regions where the model uncertainty is the highest. Depending on the context, the comparison between the model and the observation can be performed either on a climatological level, or for a specific period (year, month, etc ..). In our case, the scarcity of observations imposes us to display all data (from 2009 to 2017; the period of analysis of the model simulation) in a climatological way if we want to highlight large scale patterns. To do so, the metrics from 2009 to 2017 are averaged in 4°x4° bins, bins with less than 4 points being not included. We also computed the BIAS and RMSD within each bin.

Formatted: Font colour: Text 1

Formatted: Indent: First line: 0 cm, Don't adjust space between Latin and Asian text, Don't adjust space between Asian text and numbers

Formatted: Font colour: Text 1

Formatted: Font colour: Text 1

1 BGC models (Evans and Parslow, 1985; Riley, 1946). In addition to the time series of  
2 metrics, we also display normalized skill scores such as percent BIAS and RMSD as a  
3 function of season in order to combine quantitative metrics with visual comparison.

## 5. Results: Application to CMEMS global model

7 Examples of the diagnostic plots described in section 4 in combination with the metrics  
8 defined in Section 3 are shown. The objective of this section is to illustrate the opportunities  
9 offered by the BGC-Argo data for evaluating global BGC model solutions, rather than to  
10 provide a full evaluation of the CMEMS global model. Consequently, for each diagnostic  
11 plot, we only present one detailed example. The density plots and spatial maps for all metrics  
12 are displayed in the Appendix section (Fig. A1-A44).

### a. Taylor diagram

16 The CMEMS global model skill is summarized in the normalized Taylor diagram (Fig. 2) and  
17 Table 3. The oxygen levels metrics ( $\text{SO}_2$ ,  $\text{O}_2$  300,  $\text{O}_2$  1000),  $\text{pH}_{200-400}$ , the average nutrients and  
18 DIC concentrations in the mixed layer and in the mesopelagic layer are particularly well  
19 represented in the model. The correlation coefficients are greater than 0.95, the predicted SDs  
20 are close the observed SDs and the normalized RMSDs are lower than 0.4. The OMZs as well  
21 as the depths of DCM and nitracline are reasonably well represented in the model, with  $r >$   
22 0.9 (OMZs) and  $r > 0.8$  (for  $H_{\text{nit}}$  and  $H_{\text{dcm}}$ ) and normalized RMSDs  $< 0.6$ . The variability in  
23 the predicted  $\text{O}_{2\text{min}}$  is however larger than the observed ones. Finally, the POC concentrations,  
24 the  $\text{Chl}a$  in the mixed layer and at the DCM as well as  $\text{spCO}_2$  and  $\text{spH}$  are the worst predicted  
25 metrics. The normalised RMSDs are greater than 0.7-0.8, and  $r$  is between 0.3 and 0.7.

27 The fact that surface nutrients are well represented in the model suggests that the model  
28 captures the combination of process rates that drive nutrients dynamics. Some of these  
29 process rates drive both the nutrients,  $\text{Chl}a$  and POC dynamics, but there are also rates that  
30 are specific to each state variable. This probably explains why  $\text{Chl}a$  and POC are not  
31 performing while the surface nutrients are well simulated. However, it must be recognised  
32 that without a direct assessment of the individual rates, we cannot verify this hypothesis.

33

- Deleted: model
- Formatted: Font colour: Text 1
- Formatted: Font colour: Text 1
- Formatted: Font colour: Text 1
- Formatted: Font colour: Text 1

- Formatted: Indent: First line: 0 cm
- Deleted: -based metrics
- Formatted: Font colour: Text 1
- Deleted: A36
- Formatted: Font colour: Text 1

- Deleted: →
- Formatted: Font colour: Text 1
- Deleted: 2).
- Formatted: Font colour: Text 1
- Formatted: Font colour: Text 1

- Deleted: RMSD is
- Formatted: Font colour: Text 1
- Formatted: Font colour: Text 1
- Deleted: 4
- Formatted: Font colour: Text 1
- Deleted: 6, and the amplitude of model variations is lower than the BGC-Argo observations
- Formatted: Font colour: Text 1
- Deleted: →

1 The representation of all metrics into a single Taylor diagram allows to rapidly evaluate the  
2 strengths and the weaknesses of a model simulation. For instance, the CMEMS global model  
3 is skilled in reproducing oxygen levels and the cycling of nutrients and DIC, but the  
4 representation of Chl<sub>a</sub>, POC, spCO<sub>2</sub> and spH needs to be improved.

### 6 b. Scatter/Density plots

7  
8 The density plots for all metrics are displayed in the Appendix section (Fig. A1-A22). Here,  
9 we detail only the density plot for O<sub>2min</sub> to illustrate the potential of such representations.

10  
11 Figure 3 shows the comparison between the observed and predicted O<sub>2min</sub> values. The  
12 regression line, the slope, and the intercept as well the coefficient of determination (R<sup>2</sup>) are  
13 indicated. Overall, the model and the float O<sub>2min</sub> are in good agreement with a slope close to 1  
14 and R<sup>2</sup> close to 0.8. There is however a positive offset of ~11 μmol kg<sup>-1</sup> across all O<sub>2min</sub> values  
15 suggesting that the modelled OMZs are on average too much oxygenated by a constant value.  
16 It is worth noting that the scatter around the regression line is larger for O<sub>2min</sub> > 50 μmol kg<sup>-1</sup>,  
17 which corresponds to the Atlantic OMZ around Cap Verde (Fig. A43). This suggests that the  
18 uncertainty in this OMZ is particularly high, as confirmed in Fig. A43.

### 20 c. Spatial maps

21  
22 The spatial maps for all metrics are displayed in the Appendix section (Fig. A23-A44), while  
23 we detail hereafter the spatial distribution of sChl.

24  
25 Figure 4 shows the spatial distribution of sChl estimated from the BGC-Argo floats (Fig. 4a),  
26 the model (Fig. 4b), the BIAS (Fig. 4c) and the RMSD (Fig. 4d). As already noticed in Fig. 1,  
27 the density of sChl observations is satisfactory for high latitude regions (latitudes > 50° N and  
28 S) whereas it is poor in subtropical gyres and the Equatorial band. Nevertheless, large scale  
29 patterns in sChl are still distinguishable in Fig. 1a, especially the juxtaposition of the high-  
30 latitudes-high- sChl regions with the low-latitudes-low- sChl regions. The model (Fig. 4b)  
31 exhibits large-scale, coherent patterns. However, the model tends to be lower than the BGC-  
32 Argo observations in the high-latitudes region and higher in the subtropical gyres (Fig. 4c).  
33 The RMS difference between the predicted and the observed values seems to be quite  
34 uniform, suggesting the uncertainty in model sChl is fairly constant in all oceanic basins.

Formatted: Font colour: Text 1

Deleted: in the mixed layer

Formatted: Font colour: Text 1

Formatted: Font colour: Text 1

Deleted: POC

Formatted: Font colour: Text 1

Deleted: A18

Formatted: Font colour: Text 1

Formatted: Indent: First line: 0 cm

Formatted: Indent: First line: 0 cm

Deleted: the

Formatted: Font colour: Text 1

Deleted: Archipelago

Formatted: Font colour: Text 1

Deleted: A35

Formatted: Font colour: Text 1

Deleted: A35

Formatted: Font colour: Text 1

Formatted: Indent: First line: 0 cm

Formatted: Font colour: Text 1

Deleted: A19-A36

Formatted: Font colour: Text 1

Formatted: Indent: First line: 0 cm

Formatted: Font colour: Text 1

Formatted: Font colour: Text 1

Formatted: Font colour: Text 1

Formatted: Font colour: Text 1

Formatted: Font colour: Text 1

Formatted: Font colour: Text 1

Formatted: Font colour: Text 1

#### d. Seasonal time-series

Two examples of BGC-Argo float seasonal time-series compared to the same time-series simulated by the model along the float trajectory are presented in Figs. 5 and 6. The two figures present a case study in the North Atlantic during the “spring bloom” and a case study in the South Pacific subtropical gyre.

Figure 5 compares the seasonal time series of MLD, sChl, sNO<sub>3</sub>, sSi and sPO<sub>4</sub> derived from the BGC-Argo floats observations (blue) and from the model simulation (yellow). To avoid relying only on visual inspection, the percent BIAS and percent RMSD are also represented for each metrics and for each season.

The seasonal cycles of MLD, sChl and nutrients are typical of the North Atlantic bloom dynamics (Dale et al., 1999; Mignot et al., 2018). The temporal dynamics of sChl and nutrients are well approximated by the model with the timings of minima, maxima and the onset of the bloom being correctly represented. The winter- sChl -minimum and winter-nutrients-maxima are also properly estimated by the model (Figs. 5g and h). However, the summer- sChl -maximum is underestimated and the summer- sNO<sub>3</sub> -minimum and summer-sPO<sub>4</sub> -minimum are overestimated (Fig. 5g). This is coherent with the negative BIASs observed in the spatial map of sChl in the North Atlantic (Fig. 4) and the positive BIAS in the spatial map of sNO<sub>3</sub> and sPO<sub>4</sub> in the North Atlantic (Figs. A27 and A28).

Figure 6 shows similar time series than Fig. 5 but for an oligotrophic environment in the South Pacific subtropical gyre. The time series of H<sub>DCM</sub> and Chl<sub>DCM</sub> are also shown as this gyre is characterized by a seasonal and permanent DCM (Mignot et al., 2011). The model correctly represents the seasonal cycle of sChl, H<sub>DCM</sub> and Chl<sub>DCM</sub>, which are characteristic of this region. The average percent RMSD for these three metrics is 17 %, 12 % and 16 % respectively. The more stable time series of sSi and sPO<sub>4</sub> are also well simulated by the model: the average percent RMSD being 19 % and 11 % respectively. Finally, sNO<sub>3</sub> are constantly underestimated by the model by an average negative BIAS of roughly 0.25 μmol kg<sup>-1</sup>.

- Deleted: An example
- Deleted: a
- Formatted: Font colour: Text 1
- Formatted: Indent: First line: 0 cm
- Deleted: a simulation of
- Formatted: Font colour: Text 1
- Formatted: Font colour: Text 1
- Formatted: Font colour: Text 1
- Deleted: is
- Formatted: Font colour: Text 1
- Deleted: Fig
- Formatted: Font colour: Text 1
- Deleted: for
- Formatted: Font colour: Text 1
- Formatted: Font colour: Text 1
- Deleted:
- Formatted: Font colour: Text 1
- Formatted: Font colour: Text 1
- Formatted: Indent: First line: 0 cm
- Deleted: cycle
- Formatted: Font colour: Text 1
- Deleted: is
- Formatted: Font colour: Text 1
- Formatted: Font colour: Text 1
- Formatted: Font colour: Text 1
- Deleted: In spring, phytoplankton concentration, as measured by
- Formatted: Font colour: Text 1
- Deleted: increases dramatically
- Formatted: Font colour: Text 1
- Deleted: it is accompanied by a consumption of inorganic
- Deleted: in the mixed layer. The increase in sChl stops when one or several nutrients become exhausted and the nutrients-Chla sys (... [1])
- Formatted: Font colour: Text 1
- Deleted: entrained in the surface layer driving an increase i (... [2])
- Formatted: Font colour: Text 1
- Formatted: Font colour: Text 1
- Deleted: .
- Formatted: Font colour: Text 1
- Deleted: while the summer- sSi -minimum is correctly repre (... [3])
- Formatted: Font colour: Text 1
- Deleted: A23
- Formatted: Font colour: Text 1
- Deleted: A24
- Formatted: Font colour: Text 1
- Deleted: The conjoint analysis of the seasonal times-series (... [4])
- Formatted: Font: 12 pt, Not Bold, Font colour: Text 1
- Formatted: Indent: First line: 1,27 cm

## 6. Perspectives: metrics relative to ocean optical properties

BGC-Argo floats equipped with sensors measuring the downward planar irradiance are essential observations to evaluate the performance of recently-developed BGC models that resolve the spectral and directional properties of the underwater light field. For several years, the number of BGC models coupled with a multispectral light module has been steadily increasing (Baird et al., 2016; Dutkiewicz et al., 2015; Gregg and Rousseaux, 2016; Lazzari et al., 2020; Skákala et al., 2020). Such models require dedicated observations and metrics to evaluate their skill in representing the ocean's optical properties of the ocean. Diffuse attenuation coefficient for downwelling irradiance ( $K_d$ ) is one of the most common properties to characterise the optical state of the ocean (Sosik, 2008). Values of  $K_d$  can be derived at three different wavelengths (380, 412, 490 nm) from the BGC-Argo floats observations. This metric also provides information about the constituents of seawater (Organelli 2017) (phytoplankton for  $K_d$  at 490 nm and coloured dissolved organic carbon for  $K_d$  at 380 nm and 412 nm) and is complementary to Chl $a$  measurements for the assessment of the modelled phytoplankton dynamics.

~~BGC-Argo floats equipped with optical sensors are available on the global ocean, but the global model used in this study does not resolve the spectral and directional properties of the underwater light field. Therefore, to show the potentiality of such comparison, we use a~~ model of the Mediterranean Sea equipped with a multispectral light module (Lazzari et al., 2020) (Appendix A.2). ~~The spatial distribution of  $K_d$  at 490 nm in the first optical depth estimated from the BGC-Argo floats and from the Mediterranean Sea model are shown in Fig. 7.~~ The BGC-Argo estimated  $K_d$  at 490 nm exhibits a basin-scale pattern, with high values in the North-Western Mediterranean Sea and lower values in the Eastern Mediterranean Sea, consistent with the spatial distribution of surface Chl $a$  in the Mediterranean Sea (Bosc et al., 2004). The model is able to reproduce the large-scale pattern of  $K_d$  at 490 nm, but it tends to underestimate  $K_d$  at 490 nm in the North-Western Mediterranean Sea; area where the RMSD is also the highest. The annual cycle of phytoplankton being largely influenced by a spring bloom in this region (Bosc et al., 2004; D'Ortenzio et al., 2014), we can speculate that the underestimation of  $K_d$  at 490 nm highlights a possible misrepresentation of the spring bloom in the model that yields to lower phytoplankton and Chl $a$  concentrations. ~~The comparison~~

Formatted: Font colour: Text 1

Formatted: Indent: First line: 0 cm

Formatted: Font colour: Text 1

Formatted: Font colour: Text 1

Formatted: Font colour: Text 1

Formatted: Font colour: Text 1

Deleted:

Formatted: Font colour: Text 1

Deleted: As an example

Formatted: Indent: First line: 0 cm

Formatted: Font colour: Text 1

Formatted: Font colour: Text 1

Deleted: spatial distribution of  $K_d$  at 490 nm in the first optical depth estimated from the BGC-Argo floats and from

Formatted: Font colour: Text 1

Formatted: Font colour: Text 1

Formatted: Font colour: Text 1

Deleted: ) are shown in Fig. 7.

Formatted: Font colour: Text 1

Formatted: Font colour: Text 1

Formatted: Font colour: Text 1

Formatted: Font colour: Text 1

Formatted: Font colour: Text 1

Formatted: Font colour: Text 1

Formatted: Font colour: Text 1

Formatted: Font colour: Text 1



1 [exercise performed in the Mediterranean Sea shows the added value of BGC-Argo optical](#)  
2 [data for the assessment of biogeochemical model dynamics at the global scale.](#)

### 3 ▲

## 4 7. Conclusion

5

6 Biogeochemical ocean models are powerful tools to monitor changes in marine ecosystems  
7 and ecosystem health due to human activities, make climate projections and help developing  
8 better strategies for mitigation. However, these models are subject to flaws and require  
9 rigorous validation processes to test their predictive skills. The model's evaluations have long  
10 been damped by the lack of *in situ* observations, which has certainly slowed the development  
11 and the improvement of BGC models. The [number](#) of observations collected by the BGC-  
12 Argo program is now greater than any other *in situ* data set (Claustre et al., 2020) and thus,  
13 offers new opportunities for the validation of BGC models.

14

15 In this study, we use the global data set of BGC-Argo observations to validate a state-of-the-  
16 art BGC model simulation. Our aim was to demonstrate the invaluable opportunities offered  
17 by the BGC-Argo observations for evaluating global BGC model solutions. To ease the  
18 comparison between model and observations at global scale, we proposed [22 assessment](#)  
19 [metrics, based on the model evaluation framework developed by Hipsey et al. \(Hipsey et al.,](#)  
20 [2020\). These metrics either evaluate the model state accuracy or the skill of the model in](#)  
21 [capturing emergent properties.](#) We did not propose BGC-Argo-based phenology metrics  
22 (Gittings et al., 2019), because the numbers of [observations](#) per month and per bin is still  
23 presently too low to derive such robust metrics. We suggested 4 diagnostic plots, which we  
24 believe are particularly suitable for displaying the metrics in support of [the](#) identification of  
25 model-data difference and subsequent analysis of model representativity. We also discuss the  
26 promising avenue of BGC-Argo-based metrics relative to optical properties in the ocean for  
27 the validation of the new generation of BGC model equipped with a multispectral light  
28 module.

29

30 We assumed that the differences between the observed and predicted BGC values were only  
31 attributable to the BGC model, PISCES. However, BGC models are coupled to ocean general  
32 circulation systems and the quality of the BGC predictions strongly depends on the accuracy  
33 of the physical properties that control the BGC state variables. In our case, the dynamical

Formatted: Font colour: Text 1

Formatted: Indent: First line: 0 cm

Deleted: amount

Formatted: Font colour: Text 1

Formatted: Font colour: Text 1

Formatted: Font colour: Text 1

Formatted: Font colour: Text 1

Formatted: Indent: First line: 0 cm

Deleted: 18 key metrics of ocean health and biogeochemical functioning. These metrics are either a depth-averaged quantity or correspond to the depth of a particular feature.

Formatted: Font colour: Text 1

Formatted: Font colour: Text 1

Formatted: Font colour: Text 1

Deleted: observation

Formatted: Font colour: Text 1

Deleted: ,

Formatted: Font colour: Text 1

Formatted: Font colour: Text 1

Formatted: Indent: First line: 0 cm

1 component has been extensively validated (Lellouche et al., 2018, 2013), and correctly  
2 represented variables that are constrained by observations (e. g., temperature and salinity).  
3 However, unconstrained variables in the physical system (e.g., vertical velocities) can  
4 generate unrealistic biases in various biogeochemical variables, especially in the Equatorial  
5 Belt area (Fennel et al., 2019; Park et al., 2018).

7 We have restricted the number of diagnostic plots as well the statistical indices to the ones  
8 that are most commonly used in the modelling community. More complex statistical  
9 indicators (Stow et al., 2009) can be computed with the proposed metrics, depending on the  
10 context and the skill level necessary. Likewise, similar or more elaborate diagrams can also be  
11 used, such as Target diagram (Salon et al., 2019), zonal mean diagrams (Doney et al., 2009),  
12 or interannual time series (Doney et al., 2009).

14 The comparison between BGC-Argo data and model simulations is not only beneficial for the  
15 modelling community but also for the BGC-Argo community. Observation System  
16 Simulation Experiments (OSSEs) are generally used to inform, *a priori*, observing network  
17 design (Ford, 2020). Here, we showed that the spatial maps of model-observations  
18 comparison are also informative *a posteriori*, with respect to the network design, as they  
19 highlight sensitive areas where BGC-Argo observations are critical and where sustained  
20 BGC-Argo observations are required to better constrain the model. These maps correspond to  
21 the regions where the model uncertainty (see RMSD spatial maps in Figs. A22-A44) is the  
22 highest, i.e., the Equatorial belt with respect to the carbonate system variables, the Southern  
23 Ocean with respect to the nutrients and the DCM variables, and the western boundary currents  
24 and OMZs with respect to oxygen.

25

Formatted: Font colour: Text 1  
Formatted: Font colour: Text 1

Formatted: Font colour: Text 1  
Formatted: Font colour: Text 1, English (US)

Deleted: In addition, BGC-Argo floats are not flawless (Roesler et al., 2017), and in some cases, the discrepancies observed between the floats and model data do not result from the model estimations alone. This is particularly true for the BGC-Argo estimates of Chla in the mixed layer that can be significantly biased due to non-photochemical chlorophyll fluorescence quenching (Xing et al., 2012) or regional variations in fluorescence of Chla vs Chla relationship (Roesler et al., 2017).

Formatted: Font colour: Text 1  
Formatted: Font colour: Text 1  
Formatted: Font colour: Text 1  
Formatted: Font colour: Text 1  
Formatted: Font colour: Text 1  
Formatted: Font colour: Text 1  
Formatted: Font colour: Text 1  
Formatted: Font colour: Text 1  
Formatted: Font colour: Text 1

Deleted: ,  
Formatted: Font colour: Text 1  
Formatted: Font colour: Text 1  
Formatted: Font colour: Text 1  
Formatted: Font colour: Text 1  
Deleted: is,  
Formatted: Font colour: Text 1  
Deleted: ,  
Formatted: Font colour: Text 1  
Deleted: it highlights  
Formatted: Font colour: Text 1  
Deleted: It corresponds  
Formatted: Font colour: Text 1  
Deleted: A19-A36  
Formatted: Font colour: Text 1  
Deleted: band  
Formatted: Font colour: Text 1  
Formatted: Font colour: Text 1

Deleted: .....Page Break.....  
Tables  
Table 1. Data mode and QC flags of the BGC-Argo observations used in this study.

1 **Tables**

2

3 **Table 1.** Data mode and QC flags of the BGC-Argo observations used in this study. In the  
 4 Argo data-system, the data are available in three data modes, “Real-Time”, ”Adjusted” and  
 5 ”Delayed”. See section 2a for a brief description of each data mode. The flags “3” and “4”  
 6 refers to “potentially bad data “ and “bad data”, respectively. See also Bittig et al. (2019), for  
 7 a more detailed description of Argo data modes and flags.

8

Parameter	Data mode	Data mode of associated pressure, temperature and salinity profiles	QC flags
Chla	Adjusted and Delayed	Real time, Adjusted and Delayed	<ul style="list-style-type: none"> <li>Real time: All flags except 4</li> <li>Adjusted or Delayed: All flags except 3 and 4</li> </ul>
O <sub>2</sub>	Delayed	Delayed	<ul style="list-style-type: none"> <li>All flags except 3 and 4</li> </ul>
NO <sub>3</sub>	Adjusted and Delayed	Real time, Adjusted and Delayed	<ul style="list-style-type: none"> <li>Real time: All flags except 4</li> <li>Adjusted or Delayed: All flags except 3 and 4</li> </ul>
pH	Adjusted and Delayed	Real time, Adjusted and Delayed	<ul style="list-style-type: none"> <li>Real time: All flags except 4</li> <li>Adjusted or Delayed: All flags except 3 and 4</li> </ul>
b <sub>bp</sub>	Real time and Delayed	Real time, Adjusted and Delayed	<ul style="list-style-type: none"> <li>Real time: All flags except 4</li> <li>Adjusted or Delayed (P,T,S): All flags except 3 and 4</li> </ul>

Formatted: Font colour: Text 1

Deleted: Date

Formatted: Font colour: Text 1

Formatted: Font colour: Text 1

Formatted: Font colour: Text 1

Formatted: Font colour: Text 1

Formatted: Font colour: Text 1

Formatted: Font colour: Text 1

1

- Adjusted or Delayed (b<sub>dp</sub>):  
All flags 4

Formatted: Font colour: Text 1

1  
2  
3  
4

**Table 2.** Assessment metrics used to assess the model simulation with BGC-Argo data . For each metric, the level of assessment, as described in Hipsey et al. (2020) is also indicated.

Process	Metric	Definition	units	Assessment level
Air-sea CO <sub>2</sub> flux	spCO <sub>2</sub>	Depth-averaged pCO <sub>2</sub> in the mixed layer	μatm	State variable
Oceanic pH	spH	Depth-averaged pH in the mixed layer	total	State variable
	pH <sub>200-400</sub>	Depth-averaged pH in the 200-400 m layer	total	State variable
Biological carbon pump	sChl	Depth-averaged Chl <sub>a</sub> in the mixed layer	mg m <sup>-3</sup>	State variable
	sNO <sub>3</sub>	Depth-averaged NO <sub>3</sub> in the mixed layer	μmol kg <sup>-1</sup>	State variable
	sPO <sub>4</sub>	Depth-averaged PO <sub>4</sub> in the mixed layer	μmol kg <sup>-1</sup>	State variable
	sSi	Depth-averaged Si in the mixed layer	μmol kg <sup>-1</sup>	State variable
	sDIC	Depth-averaged DIC in the mixed layer	μmol kg <sup>-1</sup>	State variable
	NO <sub>3</sub> <sub>meso</sub>	Depth-averaged NO <sub>3</sub> in the mesopelagic layer	μmol kg <sup>-1</sup>	State variable
	PO <sub>4</sub> <sub>meso</sub>	Depth-averaged PO <sub>4</sub> in the mesopelagic layer	μmol kg <sup>-1</sup>	State variable
	Si <sub>meso</sub>	Depth-averaged Si in the mesopelagic layer	μmol kg <sup>-1</sup>	State variable

Deleted: BGC-Argo metrics used to assess the model simulation

Formatted: Font colour: Text 1

Inserted Cells

Formatted Table

Formatted: Font colour: Text 1

Deleted: μ

Formatted: Font colour: Text 1

Formatted: Font colour: Text 1

Formatted: Font colour: Text 1

Formatted: Font colour: Text 1

Formatted: Font colour: Text 1

Formatted: Font colour: Text 1

Formatted: Font colour: Text 1

Formatted: Font colour: Text 1

	$DIC_{meso}$	Depth-averaged DIC in the mesopelagic layer	$\mu\text{mol kg}^{-1}$	State variable
▲	sPOC	Depth-averaged POC in the mixed layer	$\text{mg m}^{-3}$	State variable
▲	$POC_{meso}$	Depth-averaged POC in the mesopelagic layer	$\text{mg m}^{-3}$	State variable
▲	$Chl_{DCM}$	Magnitude of DCM	$\text{mg m}^{-3}$	Emergent property
▲	$H_{DCM}$	Depth of DCM	m	Emergent property
▲	$H_{nit}$	Depth of nitracline	m	Emergent property
▲	Oxygen levels and OMZs	Depth-averaged $O_2$ in the mixed layer	$\mu\text{mol kg}^{-1}$	State variable
▲	$O_{2\ 300}$	$O_2$ at 300 m	$\mu\text{mol kg}^{-1}$	State variable
▲	$O_{2\ 1000}$	$O_2$ at 1000 m	$\mu\text{mol kg}^{-1}$	State variable
▲	$O_{2min}$	value of $O_2$ minimum	$\mu\text{mol kg}^{-1}$	Emergent property
▲	$H_{O_{2min}}$	Depth of $O_2$ minimum	m	Emergent property

Formatted: Font colour: Text 1

Formatted Table

Inserted Cells

Formatted: Font colour: Text 1

Formatted: Font colour: Text 1

Formatted: Font colour: Text 1

Formatted: Font colour: Text 1

Formatted: Font colour: Text 1

Formatted: Font colour: Text 1

Formatted: Font colour: Text 1

Formatted: Font colour: Text 1

Formatted: Font colour: Text 1

1

2

1

2 **Table 3.** Global model skill assessment. The assessment metrics are defined in Table 2.

Metric	BGC- Argo mean	BGC- Argo SD	Model mean	Model SD	Bias	RMSD	Pearson correlation coefficient
spCO <sub>2</sub> (µatm)	374	29	370	28	-5	29	0.50
spH (total)	8.056	0.030	8.058	0.028	0.001	0.028	0.54
pH <sub>200-400</sub> (total)	7.933	0.125	7.949	0.114	0.016	0.038	0.96
log <sub>10</sub> (sChl (mg m <sup>-3</sup> ))	-0.7	0.7	-0.6	0.4	0.1	0.5	0.69
sNO <sub>3</sub> (µmol kg <sup>-1</sup> )	9.4	10.1	9.1	9.6	-0.3	2.5	0.97
sPO <sub>4</sub> (µmol kg <sup>-1</sup> )	0.75	0.64	0.81	0.62	0.07	0.15	0.98
sSi (µmol kg <sup>-1</sup> )	8.5	14.6	10.5	14.6	2.0	4.7	0.96
sDIC (µmol kg <sup>-1</sup> )	2077.0	69.7	2077.5	65.8	0.4	19.0	0.96
NO <sub>3</sub> <sub>meso</sub> (µmol kg <sup>-1</sup> )	20.6	9.6	19.9	8.7	-0.8	2.2	0.98
PO <sub>4</sub> <sub>meso</sub> (µmol kg <sup>-1</sup> )	1.50	0.7	1.5	0.6	0.0	0.1	0.98
Si <sub>meso</sub> (µmol kg <sup>-1</sup> )	30.0	28.8	30.7	26.9	0.7	4.6	0.99
DIC <sub>meso</sub> (µmol kg <sup>-1</sup> )	2170.5	57.2	2161.1	53.7	-9.4	15.8	0.98
log <sub>10</sub> (sPOC (mg m <sup>-3</sup> ))	1.73	0.29	1.55	0.27	-0.18	0.32	0.57
log <sub>10</sub> (POC <sub>meso</sub> (mg m <sup>-3</sup> ))	1.41	0.23	0.99	0.32	-0.42	0.53	0.35
Chl <sub>DCM</sub> (m)	-0.3	0.4	-0.4	0.2	-0.1	0.3	0.55
H <sub>DCM</sub> (m)	79	36	75	36	-3	21	0.84
H <sub>nit</sub> (m)	43	63	41	57	-2	27	0.89

sO <sub>2</sub> (μmol kg <sup>-1</sup> )	266.9	47.8	267.3	47.9	0.4	12.8	0.96
O <sub>2 300</sub> (μmol kg <sup>-1</sup> )	208.3	68.8	211.4	61.9	3.1	18.9	0.96
O <sub>2min</sub> (μmol kg <sup>-1</sup> )	208.3	68.8	211.4	61.9	3.1	18.9	0.96
H <sub>2</sub> O <sub>2min</sub> (m)	725	362	813	332	87	165	0.92

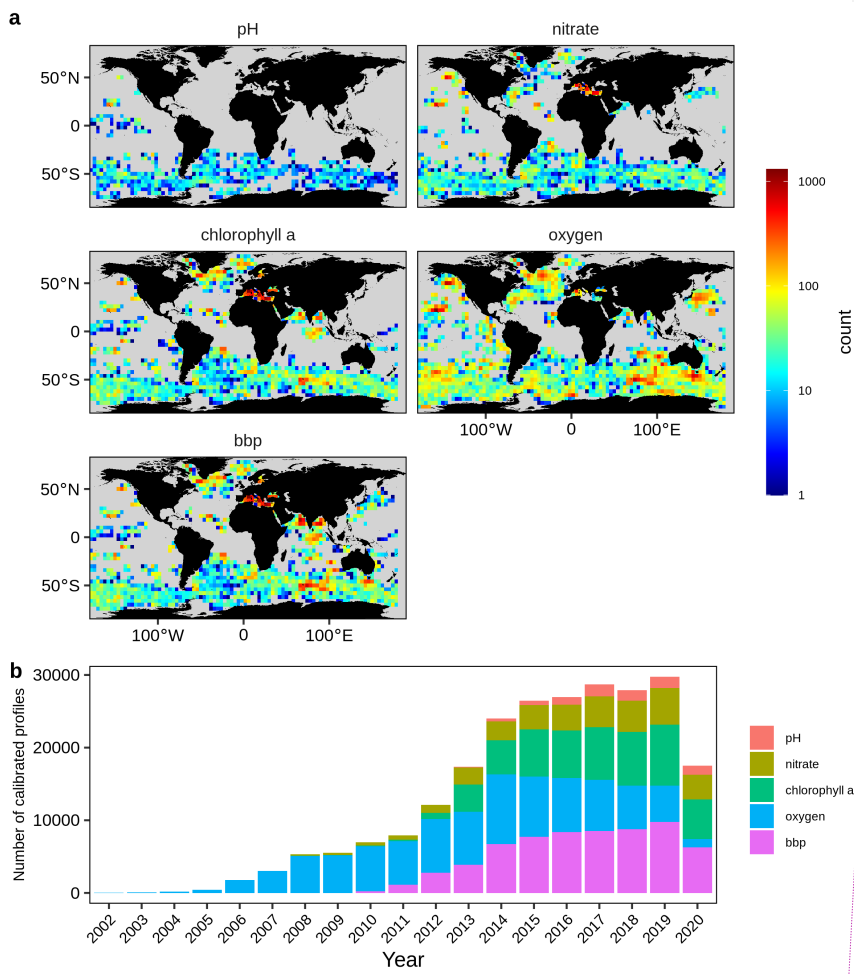
Formatted: Font colour: Text 1

- 1
- 2



1  
2  
3

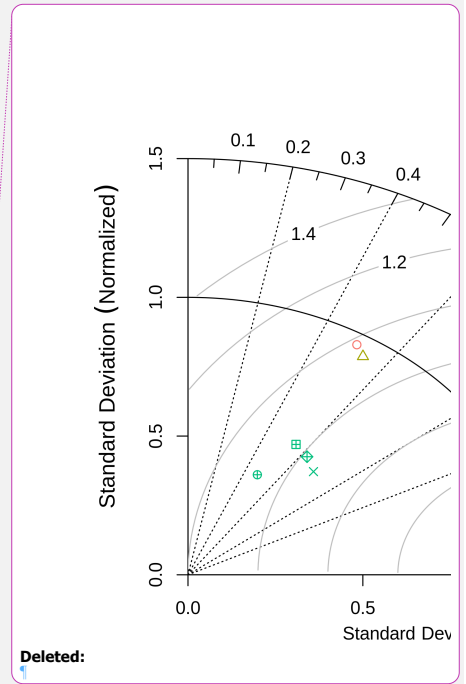
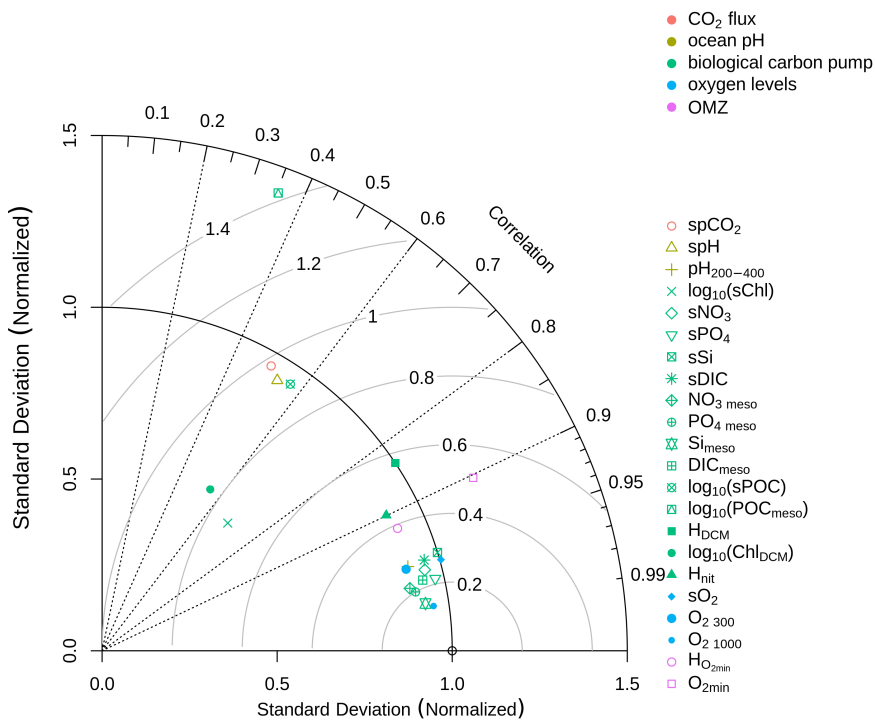
## Figures



4

5 **Figure 1.** Spatial and temporal coverage of quality-controlled BGC-Argo pH,  $\text{NO}_3^-$ , Chl $a$ ,  $\text{O}_2$ ,  
6 and  $\text{bbp}$  profiles. **(a)** Number of quality-controlled profiles for the entire period per 4°x4° bin.  
7 **(b)** Number of quality-controlled profiles per year.

Deleted:  
Formatted: Font colour: Text 1  
Deleted:  $\text{NO}_3^-$   
Deleted:  $\text{O}_2$

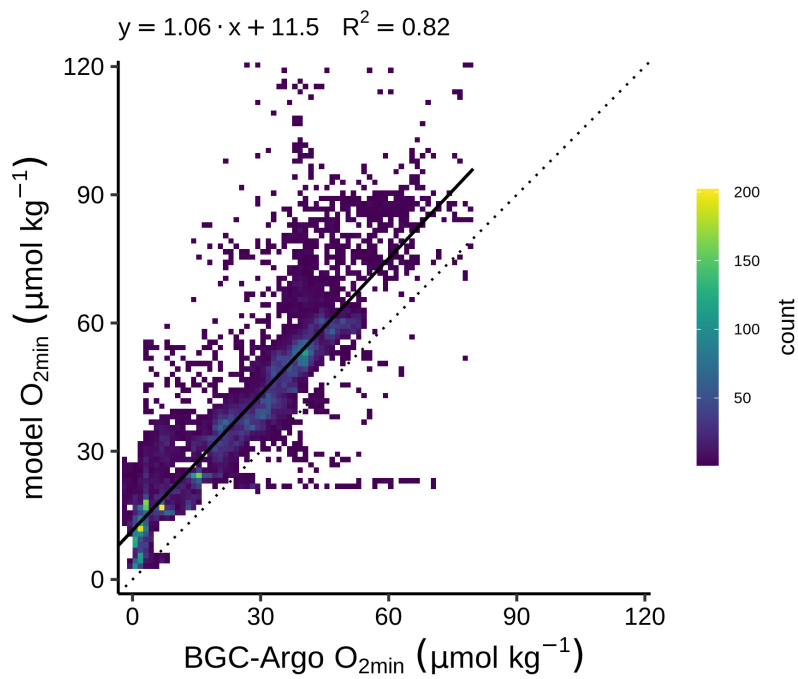


Deleted:

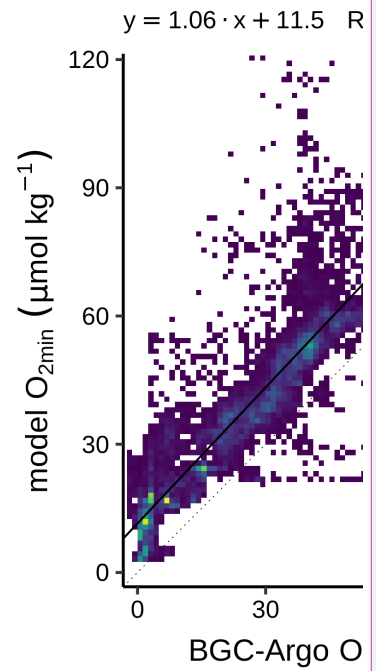
Formatted: Font colour: Text 1

1  
 2 **Figure 2.** Comparison of BGC-Argo floats' observations and model values for all metrics  
 3 using Taylor diagram. The symbols correspond to the metrics and the colours represent the  
 4 BGC processes with which they are associated. Note that the metrics calculated from the float  
 5 pH and NO<sub>3</sub> used both the direct observations of the floats and as well as the estimations from  
 6 CANYON-B. The metrics related to Chl<sub>a</sub> and POC, namely sChl, Chl<sub>DCM</sub>, sPOC, POC<sub>meso</sub>  
 7 were log<sub>10</sub>-transformed because they cover several orders of magnitude and they are  
 8 lognormally distributed. Observed DCMs and nitracline deeper than 250 m are not included.

9  
 10

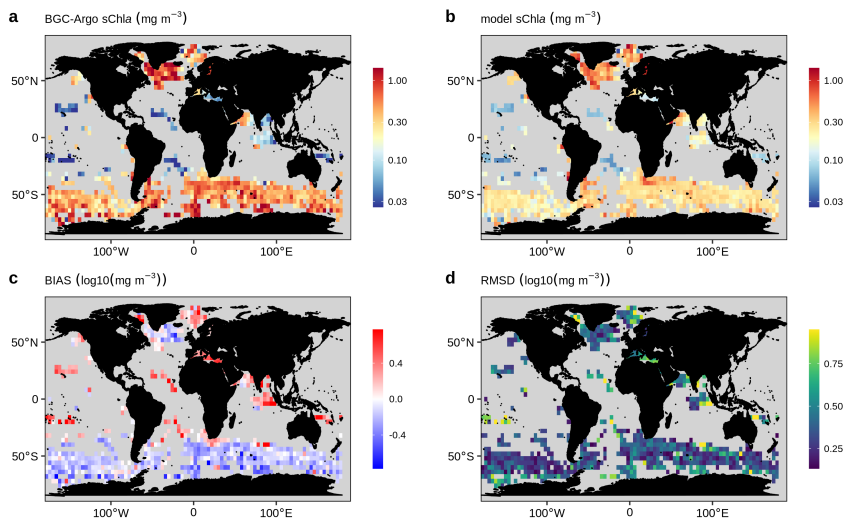


1  
 2 **Figure 3.** Density plots of BGC-Argo floats' observations and model  $O_{2min}$ . Each axis is  
 3 divided in 100 bins and the colour represents the number of points in each bin. The dashed  
 4 line represents the 1:1 line. The plain line represents the linear regression line between the  
 5 two data sets. The coefficients of the linear regression line (gain and offset) as well the  
 6 coefficient of determination ( $R^2$ ) are indicated on the top of the plot.



Deleted:

Formatted: Font colour: Text 1



1  
2  
3  
4  
5  
6  
7  
8

**Figure 4.** Spatial distribution maps of BGC-Argo floats' observations of sChl (a), model sChl (b), the BIAS (c) and the RMSD (d). The data are averaged in 4°x4° bins. Bins containing less than 4 points are excluded. The BIAS and RMSD are computed on the log<sub>10</sub>-transformed data to account that sChl covers several orders of magnitude and is lognormally distributed (Campbell, 1995).

Formatted: Font colour: Text 1  
Formatted: Font colour: Text 1

Formatted: Font colour: Text 1

Formatted: Font colour: Text 1

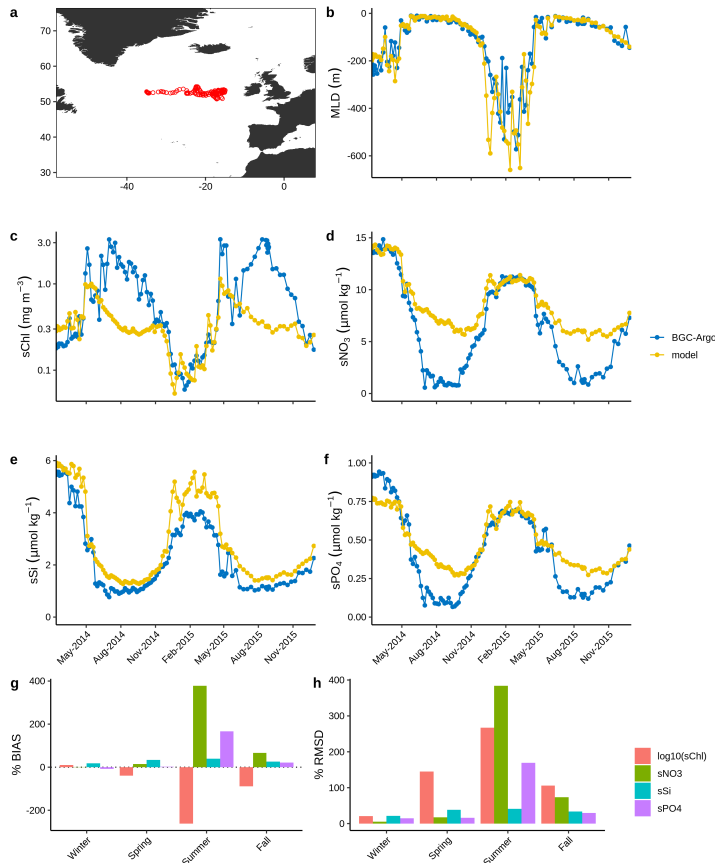
Deleted:

Formatted: Font colour: Text 1

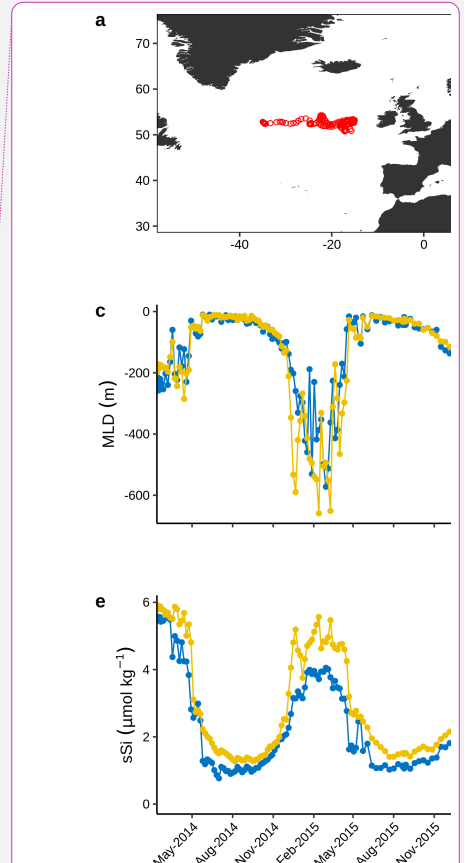
Formatted: Font colour: Text 1

Formatted: Font colour: Text 1

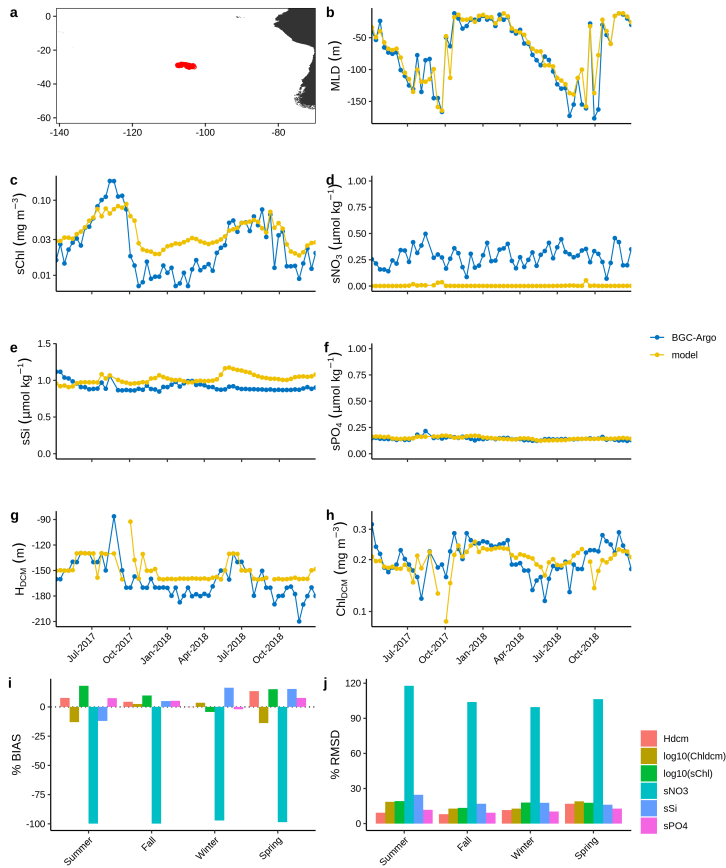
Formatted: Font colour: Text 1



1  
 2 **Figure 5.** (a) Float trajectory of a BGC-Argo float located in the North Atlantic (WMO  
 3 number: 5904479). Time series of (b), mixed layer depth, (c), sChl, (d), sNO<sub>3</sub>, (e), sSi, (f),  
 4 sPO<sub>4</sub> derived from the BGC-Argo floats observations (blue) and from the model simulation  
 5 (yellow). (g), Percent BIAS  $\left(100 \times \frac{\frac{1}{N} \sum_{i=1}^N (model_i - obs_i)}{|obs_i|}\right)$  and (h), percent RMSD  
 6  $\left(100 \times \sqrt{\frac{\frac{1}{N} \sum_{i=1}^N (model_i - obs_i)^2}{|obs_i|^2}}\right)$  as a function of season. The float sChl and sNO<sub>3</sub> are calculated  
 7 from the direct observations of the floats, whereas the float sSi and sPO<sub>4</sub> result from  
 8 CANYON-B predictions.  
 9

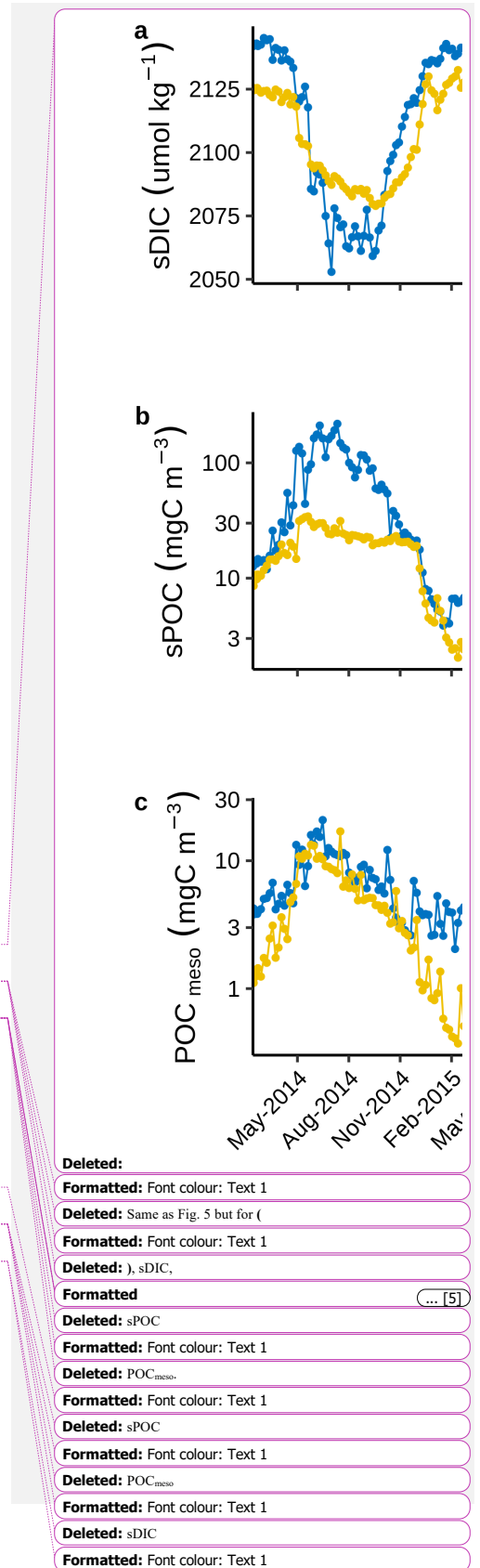


Deleted:  
 Formatted: Font colour: Text 1  
 Deleted: the  
 Formatted: Font colour: Text 1  
 Formatted: Font colour: Text 1  
 Deleted: 2014-2015 time  
 Formatted: Font colour: Text 1  
 Deleted: ,  
 Formatted: Font colour: Text 1  
 Formatted: Font colour: Text 1  
 Deleted:  
 Formatted: Font colour: Text 1  
 Formatted: Font colour: Text 1



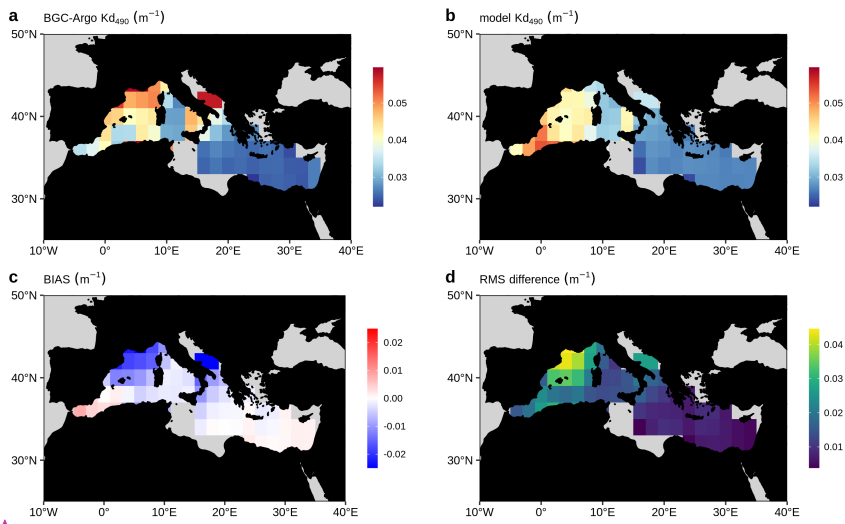
1  
 2 **Figure 6. a)** Float trajectory of a BGC-Argo float located in the South Pacific subtropical  
 3 gyre (WMO number: 5904479). Time series of **(b)**, mixed layer depth, **(c)**, sChl, **(d)**, sNO<sub>3</sub>,  
 4 **(e)**, sSi, **(f)**, sPO<sub>4</sub>, **(g)**, H<sub>DCM</sub>, **(h)**, Chl<sub>DCM</sub> derived from the BGC-Argo floats observations  
 5 (blue) and from the model simulation (yellow). Time series of **(i)**, percent BIAS  
 6  $\left(100 \times \frac{\frac{1}{N} \sum_{i=1}^N (model_i - obs_i)}{|obs_i|}\right)$  and **(j)** percent RMSD  $\left(100 \times \sqrt{\frac{\frac{1}{N} \sum_{i=1}^N (model_i - obs_i)^2}{|obs_i|^2}}\right)$ . The float  
 7 sChl, H<sub>DCM</sub>, Chl<sub>DCM</sub> and sNO<sub>3</sub> are calculated from the direct observations of the floats,  
 8 whereas the float sSi and sPO<sub>4</sub> result from CANYON-B predictions.

9



Deleted:  
 Formatted: Font colour: Text 1  
 Deleted: Same as Fig. 5 but for (  
 Formatted: Font colour: Text 1  
 Deleted: ), sDIC,  
 Formatted: ... [5]  
 Deleted: sPOC  
 Formatted: Font colour: Text 1  
 Deleted: POC<sub>meso</sub>,  
 Formatted: Font colour: Text 1  
 Deleted: sPOC  
 Formatted: Font colour: Text 1  
 Deleted: POC<sub>meso</sub>  
 Formatted: Font colour: Text 1  
 Deleted: sDIC  
 Formatted: Font colour: Text 1

1



2

3 **Figure 7.** Spatial distribution maps of BGC-Argo floats' observations  $K_d$  at 490 nm (a),  
4 modelled  $K_d$  at 490 nm from the Mediterranean BGC model (b), the BIAS (c) and the RMSD  
5 (d). The data are averaged in  $2^\circ \times 2^\circ$  bins. Bins containing less than 4 points are excluded.

6

7

8

Formatted: Font colour: Text 1

Formatted: Font colour: Text 1

Formatted: Font colour: Text 1

Formatted: Font colour: Text 1

1 **Appendix**

2

3 **A.1 The CMEMS global hydrodynamic-biogeochemical model**

4

5 The model used in this study features the offline coupled NEMO–PISCES model, with a 1/4°  
6 horizontal resolution 50 vertical levels (with 22 levels in the upper 100 m, the vertical  
7 resolution is 1m near the surface and decreases to 450m resolution near the bottom) and daily  
8 temporal resolution, covering the period from 2009 to 2017.

9

10 The biogeochemical model PISCES v2 (Aumont et al., 2015) is a model of intermediate  
11 complexity designed for global ocean applications, and is part of NEMO modelling platform.  
12 It features 24 prognostic variables and includes five nutrients that limit phytoplankton growth  
13 (nitrate, ammonium, phosphate, silicate and iron) and four living compartments: two  
14 phytoplankton size classes (nanophytoplankton and diatoms, resp. small and large) and two  
15 zooplankton size classes (microzooplankton and mesozooplankton, resp. small and large); the  
16 bacterial pool is not explicitly modelled. PISCES distinguishes three non-living detrital pools  
17 for organic carbon, particles of calcium carbonate and biogenic silicate. Additionally, the  
18 model simulates the carbonate system and dissolved oxygen. PISCES has been successfully  
19 used in a variety of biogeochemical studies, both at regional and global scale (Bopp et al.,  
20 2005; Gehlen et al., 2006, 2007; Gutknecht et al., 2019; Lefèvre et al., 2019; Schneider et al.,  
21 2008; Séférian et al., 2013; Steinacher et al., 2010; Tagliabue et al., 2010).

22

23 The dynamical component is the latest Mercator Ocean global 1/12° high-resolution ocean  
24 model system, extensively described and validated in Lellouche et al. (2013, 2018). This  
25 system provides daily and 1/4°-coarsened fields of horizontal and vertical current velocities,  
26 vertical eddy diffusivity, mixed layer depth, sea ice fraction, potential temperature, salinity,  
27 sea surface height, surface wind speed, freshwater fluxes and net surface solar shortwave  
28 irradiance that drive the transport of biogeochemical tracers. This system also features a  
29 reduced-order Kalman filter based on the Singular Evolutive Extended Kalman filter (SEEK)  
30 formulation introduced by Pham et al. (1998), that assimilates, on a 7-day assimilation cycle,  
31 along-track altimeter data, satellite Sea Surface Temperature and Sea-Ice Concentration from

Formatted: Indent: First line: 0 cm

Formatted: Font colour: Text 1

Formatted: Indent: First line: 0 cm

Formatted: Font colour: Text 1

Formatted: Font colour: Text 1

Formatted: Font colour: Text 1

Formatted: Indent: First line: 0 cm

Deleted: (2018, 2013).

Formatted: Font colour: Text 1

Formatted: Font colour: Text 1

Formatted: Font colour: Text 1



1 OSTIA, and *in situ* temperature and salinity vertical profiles from the CORA 4.2 *in situ*  
2 database.

3

4 In addition, the biogeochemical component of the coupled system also embeds a reduced  
5 order Kalman filter (similar to the above mentioned) that operationally assimilates daily L4  
6 remotely sensed surface chlorophyll

7 (<https://resources.marine.copernicus.eu/documents/QUID/CMEMS-GLO-QUID-001->

8 028.pdf). In parallel, a climatological-damping is applied to nitrate, phosphate, oxygen,

9 silicate - with World Ocean Atlas 2013 - to dissolved inorganic carbon and alkalinity – with

10 GLODAPv2 climatology (Key et al., 2015) - and to dissolved organic carbon and iron - with a

11 4000-year PISCES climatological run. This relaxation is set to mitigate the impact of the

12 physical data assimilation in the offline coupled hydrodynamic-biogeochemical system,

13 leading significant rises of nutrients in the Equatorial Belt area, and resulting in an unrealistic

14 drift of various biogeochemical variables e.g. chlorophyll, nitrate, phosphate (Fennel et al.,

15 2019; Park et al., 2018). The time-scale associated with this climatological damping is set to 1

16 year and allows a smooth constraint that has been shown to be efficient to reduce the model

17 drift.

18

## 19 **A.2 The Mediterranean Sea biogeochemical model MedBFM**

20

21 The Mediterranean Sea biogeochemical model MedBFM, is based on the system described in

22 Teruzzi et al. (2014) and Salon et al. (2019).

23

24 The physical forcing fields needed to compute the transport include the 3-d horizontal and

25 vertical current velocities, vertical eddy diffusivity, potential temperature, and salinity and 2-d

26 data surface data for wind stress. These forcing datasets are simulated by the Mediterranean

27 Sea Monitoring and Forecasting Centre (MED-MFC) in the Copernicus Marine Environmental

28 Monitoring Service (CMEMS, <http://marine.copernicus.eu>). The biogeochemical model is then

29 offline forced adopting the output computed by the CMEMS MED-MFC. In the present

30 application, we switched off the biogeochemical assimilation scheme that is currently used in

31 the operational MED-MFC system.

32

Formatted: Indent: First line: 0 cm

Formatted: Font colour: Text 1

Formatted: Font colour: Text 1

Formatted: Font colour: Text 1

Formatted: Font colour: Text 1

Formatted: Indent: First line: 0 cm

Formatted: Indent: First line: 0 cm

1 The light propagation is resolved coupling an atmospheric multispectral radiative transfer  
2 model (Lazzari et al., 2020) with an in-water radiative model (Dutkiewicz et al., 2015) featuring  
3 bands at 25 nm resolution in the UV and visible wavelengths.

4  
5 The horizontal resolution is approximately 6 km and there are 72 vertical levels with 3 m  
6 resolution at surface coarsening at 300 m for the deeper layers. The biogeochemical model here  
7 adopted (Biogeochemical Flux Model -- BFM -- ; (Vichi et al., 2015)) has been already applied  
8 to simulate primary producers biogeochemistry (Lazzari et al., 2012), alkalinity spatial and  
9 temporal variability (Cossarini et al., 2015), and CO<sub>2</sub> fluxes (Canu et al., 2015) for the  
10 Mediterranean Sea, and has been corroborated using *in situ* data for the operational purposes  
11 within CMEMS (Salon et al., 2019). The BFM model has been expanded in the present  
12 configuration adding the dynamics of coloured dissolved organic carbon (CDOM) by assuming  
13 a constant CDOM:DOC production ratio (i.e. 2%, as in (Dutkiewicz et al., 2015)). The  
14 absorption of CDOM, is described using reference absorption at 450 nm of 0.015 m<sup>2</sup>/mgC  
15 (Dutkiewicz et al., 2015) and an exponential slope of 0.017 nm<sup>-1</sup> (Babin et al., 2003; Organelli  
16 et al., 2014).

17 ▲  
18 **A.3 BGC-Argo K<sub>d</sub> estimates**

19 ▲  
20 The data used to compute the K<sub>d</sub> metrics are quality checked according to Organelli et al.  
21 (2017). Moreover, for the K<sub>d</sub> logarithmic interpolation, the following selection rules were  
22 applied: the profile must have at least 5 BGC Argo float sampling in the first optical depth, the  
23 gap between the two shallower acquisitions must be less than 10 meters, and there must be at  
24 least one measurement deeper than 15 meters.

25 ▲  
26 **A.4 Figures**

Formatted: Indent: First line: 0 cm

Formatted: Indent: First line: 0 cm

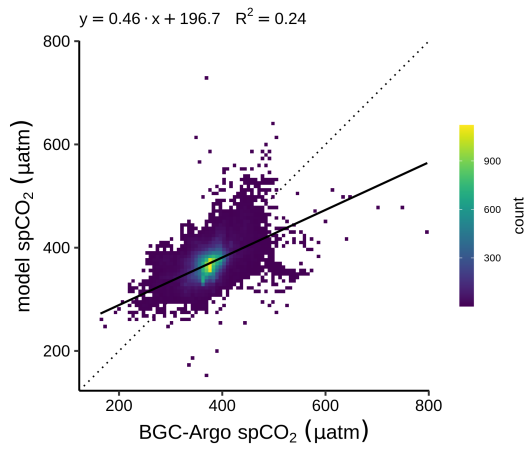
Field Code Changed

Formatted: Font colour: Text 1

Formatted: Font colour: Text 1

Formatted: Indent: First line: 0 cm

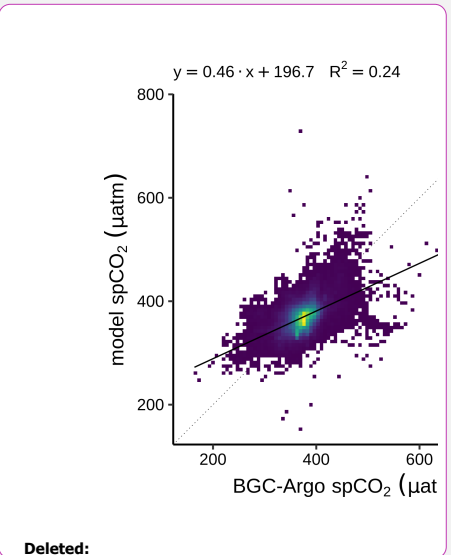
Formatted: Font colour: Text 1



1

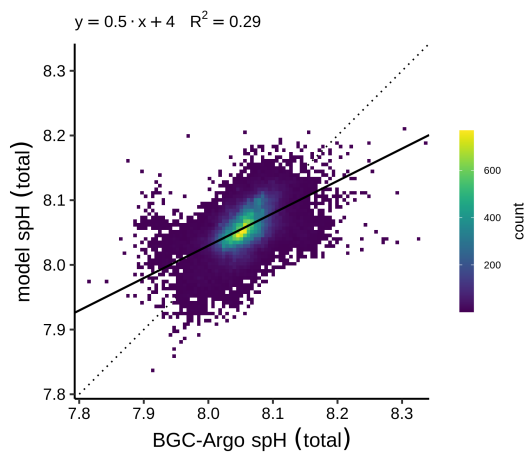
2 **Figure A1.** Same as Figure 3 but for spCO<sub>2</sub>.

3



**Deleted:**

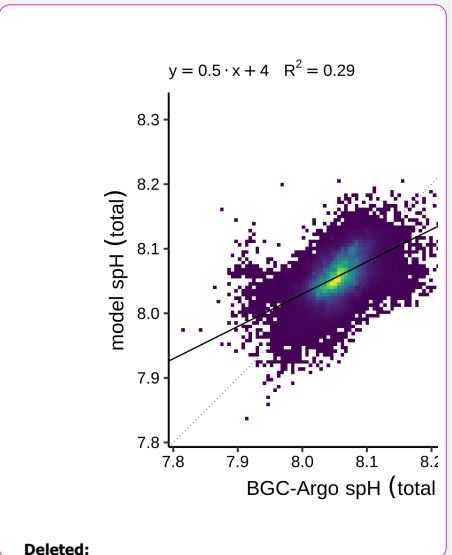
**Formatted:** Font colour: Text 1



4

5 **Figure A2.** Same as Figure 3 but for spH. Note that spH is calculated from both the direct  
6 observations of the floats and as well as the estimations from CANYON-B.

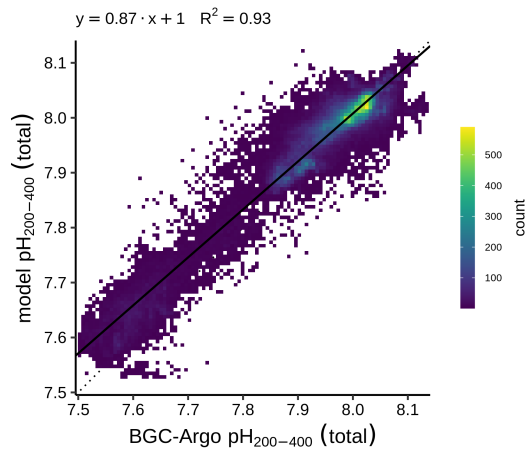
7



**Deleted:**

**Formatted:** Font colour: Text 1

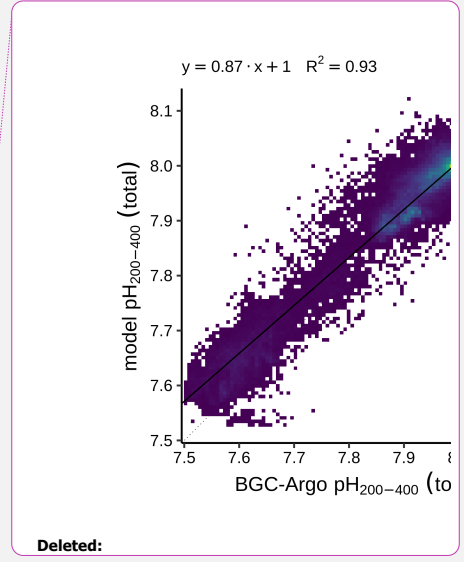
1



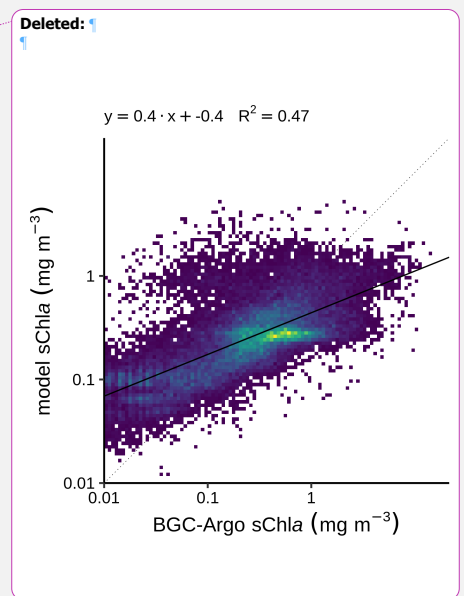
2

3 **Figure A3.** Same as Figure 3 but for pH<sub>200-400</sub>. Note that pH<sub>200-400</sub> is calculated from both the  
4 direct observations of the floats and as well as the estimations from CANYON-B.

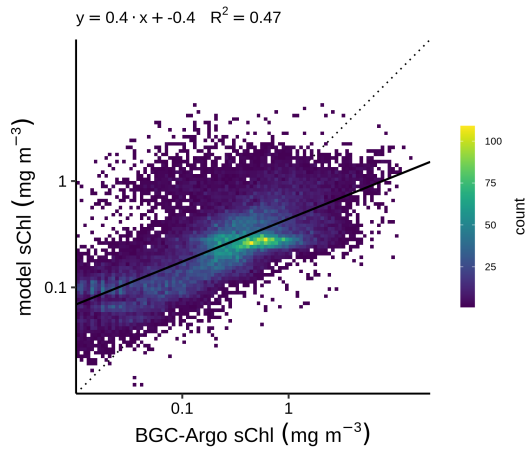
5



Formatted: Font colour: Text 1



1



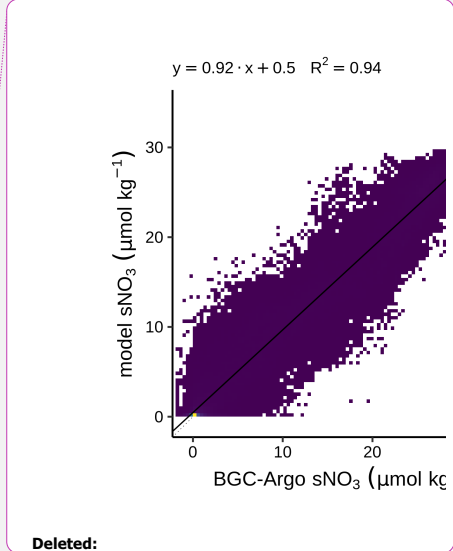
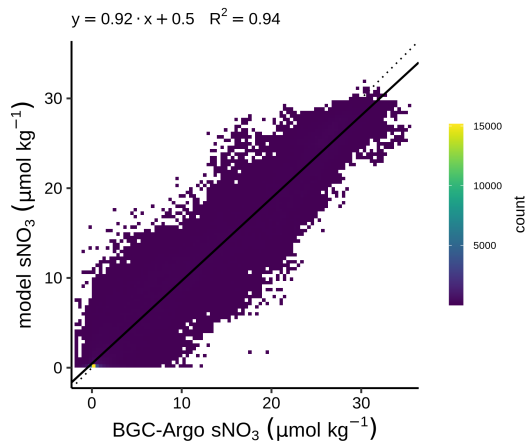
2

3 **Figure A4.** Same as Figure 3 but for sChl. Note that the least squares regression is computed  
 4 on the log<sub>10</sub>-transformed data to account that sChl covers several orders of magnitude and it is  
 5 lognormally distributed (Campbell, 1995). Data lower than 0.01 mg m<sup>-3</sup> are not included.

6

- Formatted: Font colour: Text 1
- Formatted: Font colour: Text 1
- Formatted: Font colour: Text 1
- Formatted: Font colour: Text 1
- Formatted: Font colour: Text 1

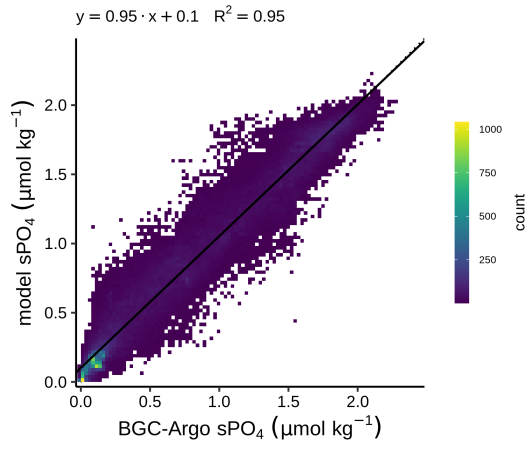
7



Deleted:

1 **Figure A5.** Same as Figure 3 but for sNO<sub>3</sub>. Note that sNO<sub>3</sub> is calculated from both the direct  
2 observations of the floats and as well as the estimations from CANYON-B.

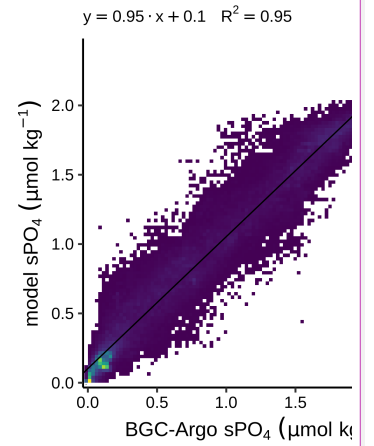
3  
4



5  
6  
7

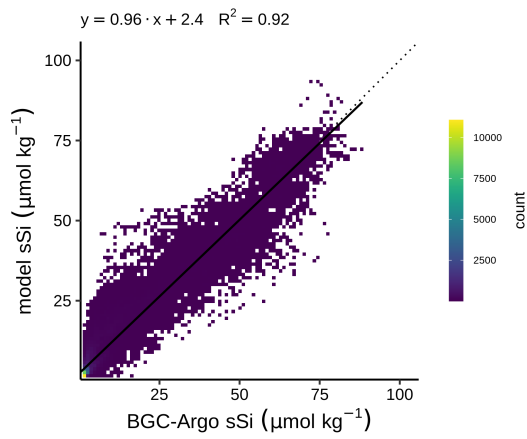
**Figure A6.** Same as Figure 3 but for sPO<sub>4</sub>.

Formatted: Font colour: Text 1



Deleted:

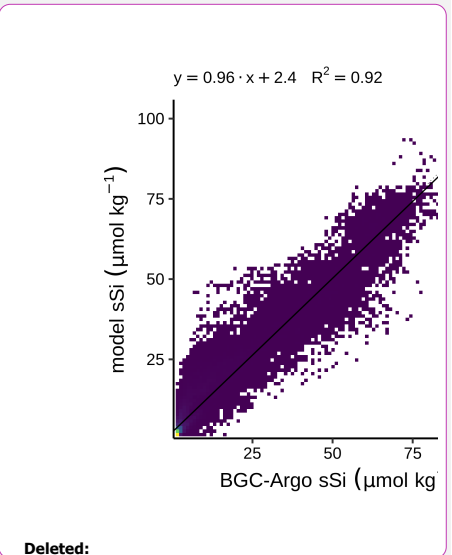
Formatted: Font colour: Text 1



1

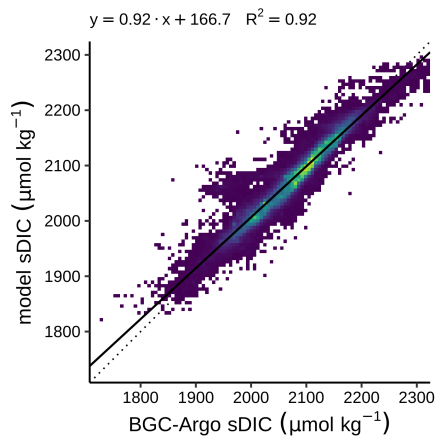
2 **Figure A7.** Same as Figure 3 but for sSi.

3



**Deleted:**

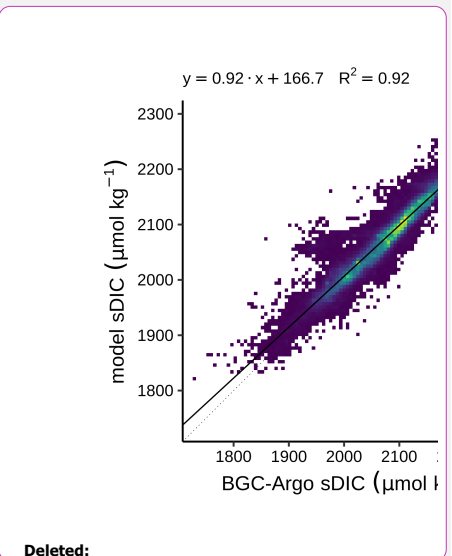
**Formatted:** Font colour: Text 1



4

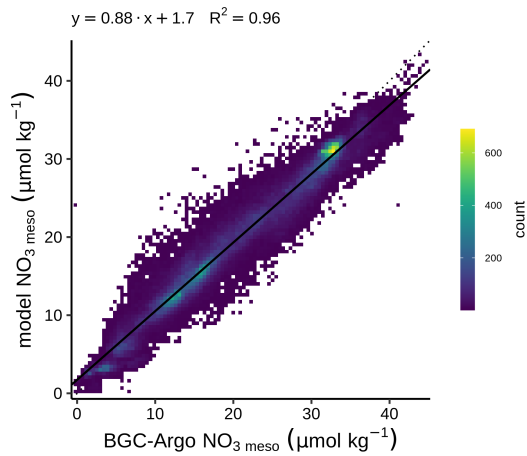
5 **Figure A8.** Same as Figure 3 but for sDIC.

6



**Deleted:**

**Formatted:** Font colour: Text 1



1  
2  
3  
4  
5

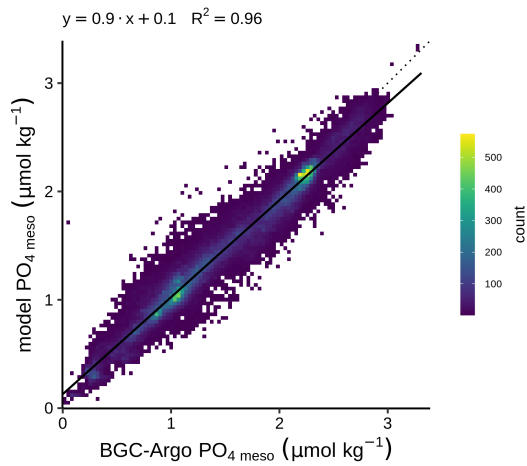
**Figure A9.** Same as Figure 3 but for  $\text{NO}_3$  meso. Note that  $\text{NO}_3$  meso is calculated from both the direct observations of the floats and as well as the estimations from CANYON-B.

Moved (insertion) [1]

Formatted: Font colour: Text 1

Formatted: Font: 12 pt, Font colour: Text 1

Formatted: Indent: Left: 0 cm, Border: Top: (No border), Bottom: (No border), Left: (No border), Right: (No border), Between : (No border)

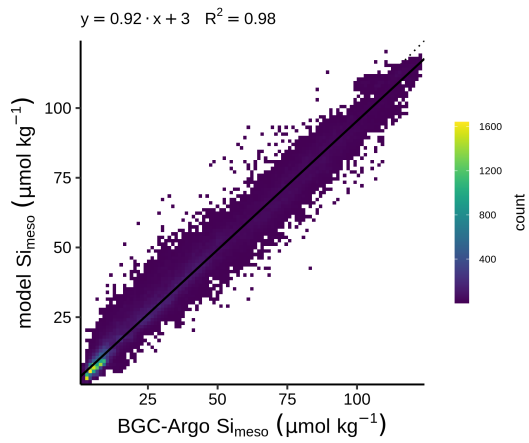


6  
7

**Figure A10.** Same as Figure 3 but for  $\text{PO}_4$  meso.



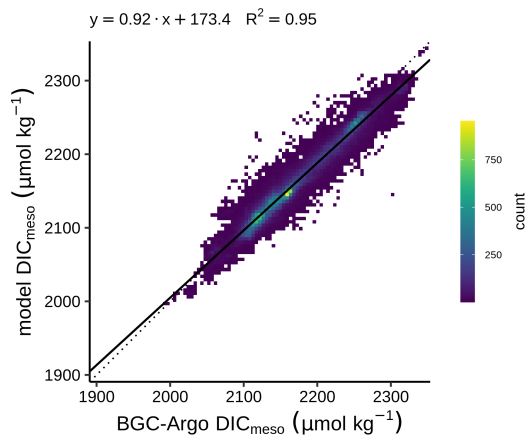
1



2

3 Figure A11. Same as Figure 3 but for  $\text{Si}_{\text{meso}}$ .

4



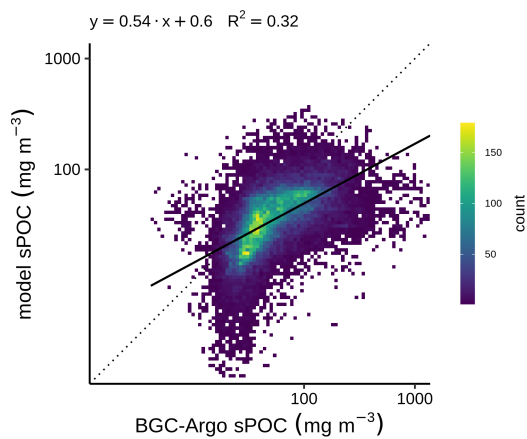
5

6 Figure A12. Same as Figure 3 but for  $\text{DIC}_{\text{meso}}$ .

7

Moved (insertion) [2]

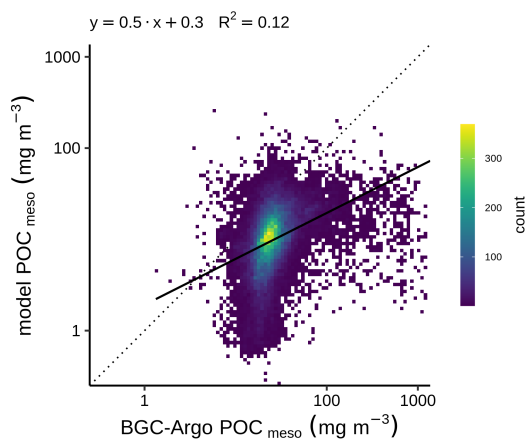
Formatted: Font colour: Text 1



1

2 **Figure A13.** Same as Figure 3 but for sPOC. Note that the least squares regression is  
 3 computed on the  $\log_{10}$ -transformed data to account that sPOC covers several orders of  
 4 magnitude and it is lognormally distributed (Campbell, 1995). Data lower than  $0.01 \text{ mg m}^{-3}$   
 5 are not included.

6



7

Moved (insertion) [3]

Formatted: Font colour: Text 1

Deleted:

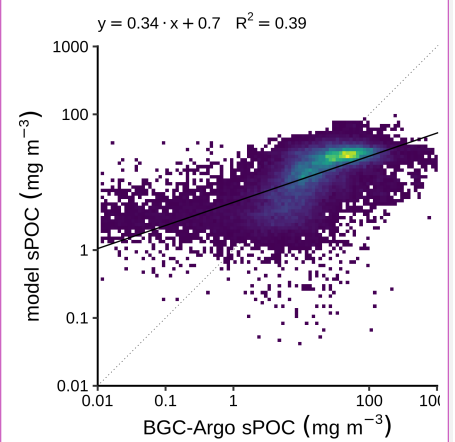
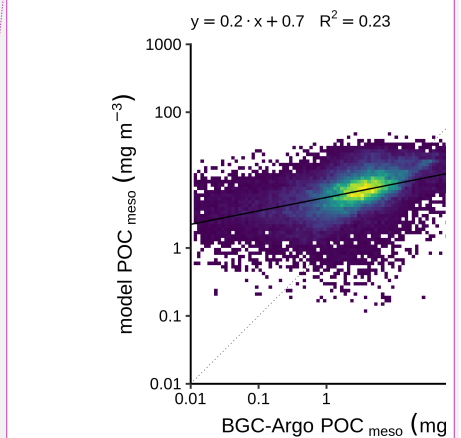


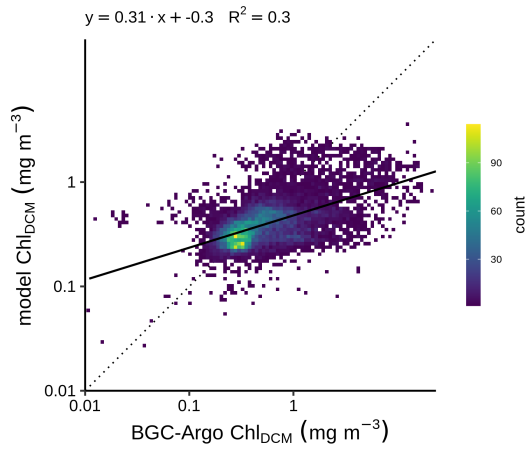
Figure A9.

Formatted: Font colour: Text 1

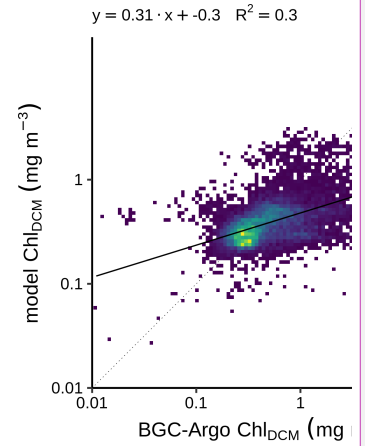


Deleted:

1 **Figure A14.** Same as Figure 3 but for  $\text{POC}_{\text{meso}}$ . Note that the least squares regression is  
 2 computed on the  $\log_{10}$ -transformed data to account that  $\text{POC}_{\text{meso}}$  covers several orders of  
 3 magnitude and it is lognormally distributed (Campbell, 1995). Data lower than  $0.01 \text{ mg m}^{-3}$   
 4 are not included.



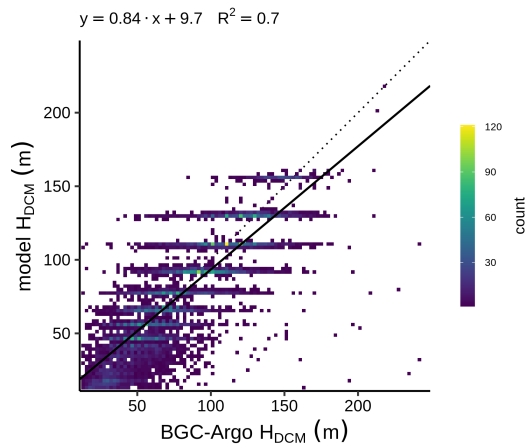
8  
 9 **Figure A15.** Same as Figure 3 but for  $\text{Chl}_{\text{DCM}}$ . Note that the least squares regression is  
 10 computed on the  $\log_{10}$ -transformed data to account that  $\text{Chl}_{\text{DCM}}$  covers several orders of  
 11 magnitude and it is lognormally distributed (Campbell, 1995). Data lower than  $0.01 \text{ mg m}^{-3}$   
 12 are not included. Observed DCMs deeper than 250 m are not included.



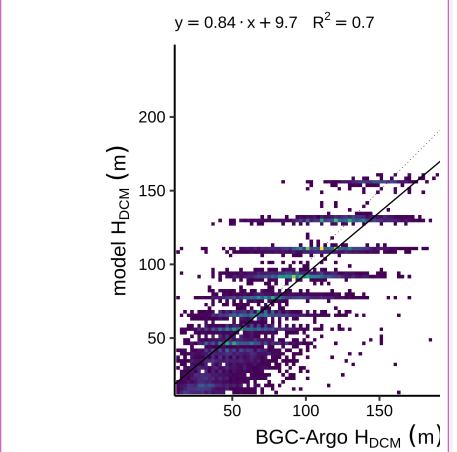
13  
 14  
 15

Deleted: A10  
 Formatted: Font colour: Text 1  
 Formatted: Font colour: Text 1

Deleted:  
 Formatted: Font colour: Text 1  
 Deleted: A11  
 Formatted: Font colour: Text 1



1  
2 **Figure A16.** Same as Figure 3 but for  $H_{DCM}$ . Observed DCMs deeper than 250 m are not  
3 included.

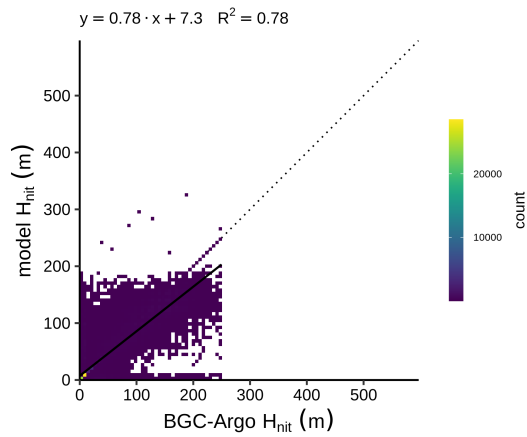


**Deleted:**

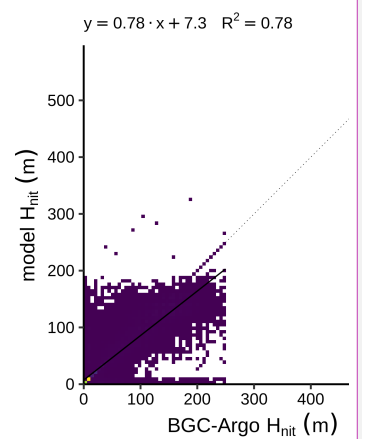
**Moved up [2]:** Figure A12. Same as Figure 3 but for

**Moved (insertion) [4]**

**Formatted:** Font colour: Text 1



4  
5 **Figure A17.** Same as Figure 3 but for  $H_{nit}$ . Observed nitracline deeper than 250 m are not  
6 included.  
7



**Deleted:**

**Moved up [3]:** Figure A13.

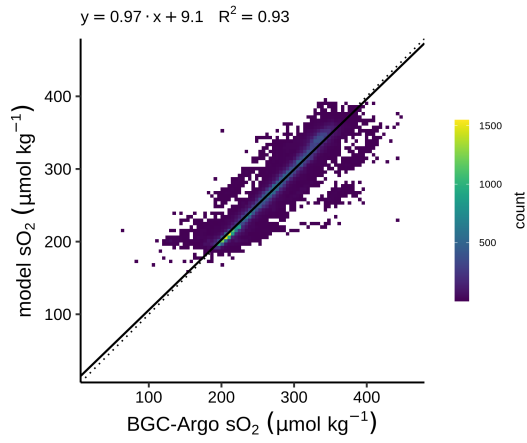
**Deleted:** Same as Figure 3

**Moved (insertion) [5]**

**Formatted:** Font colour: Text 1

**Formatted:** Font colour: Text 1

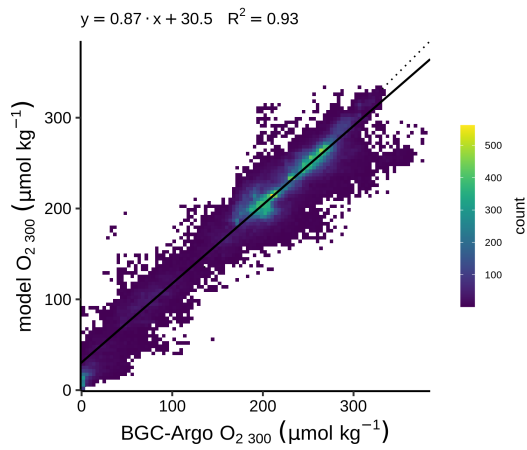
1



2

3 **Figure A18.** Same as Figure 3 but for sO<sub>2</sub>.

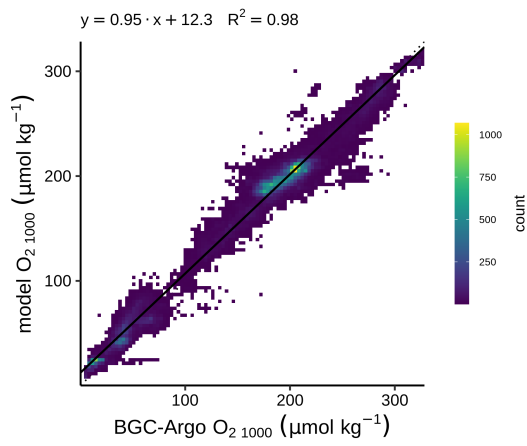
4



5

6 **Figure A19.** Same as Figure 3 but for O<sub>2</sub><sub>300</sub>.

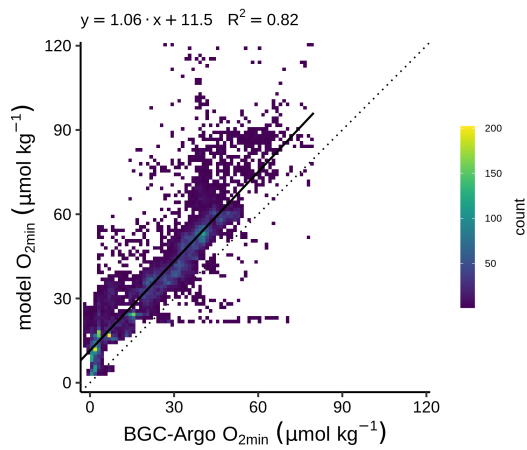
7



1

2 **Figure A20.** Same as Figure 3 but for  $O_2$  1000.

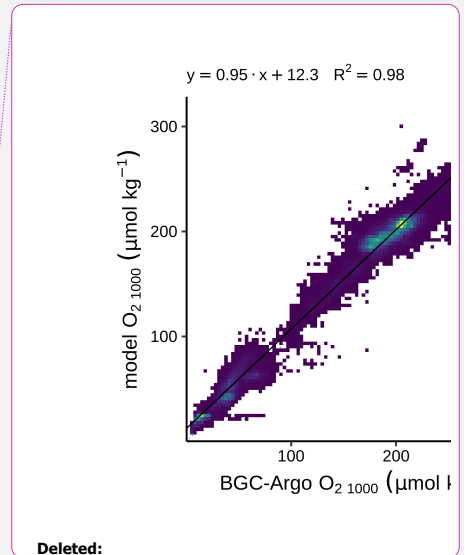
3



4

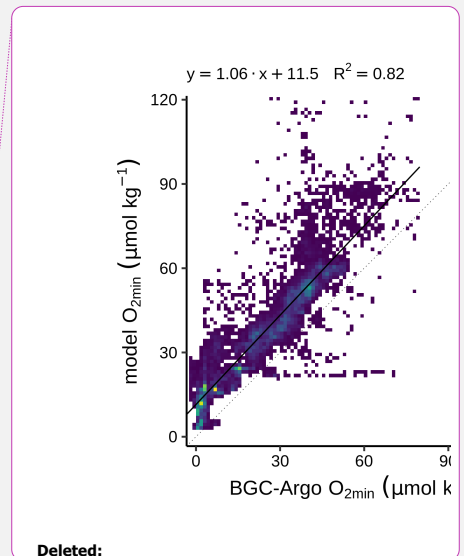
5 **Figure A21.** Same as Figure 3.

6



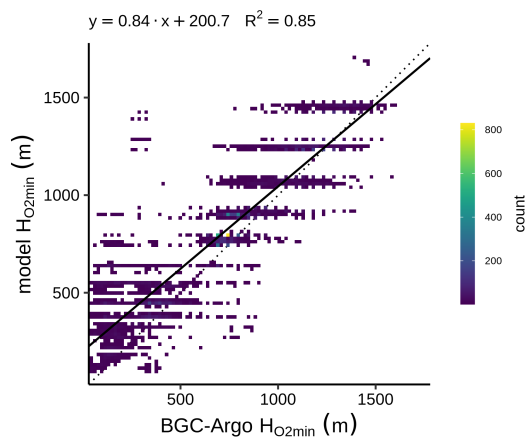
**Deleted:**

**Moved up [4]:** Figure A16. Same as Figure 3 but for  
**Formatted:** Font colour: Text 1



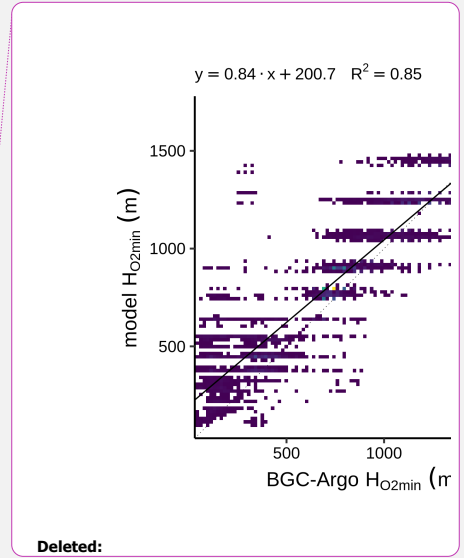
**Deleted:**

**Moved (insertion) [7]**  
**Formatted:** Font colour: Text 1  
**Moved up [5]:** Figure A17. Same as Figure 3  
**Formatted:** Font colour: Text 1



1  
2  
3

Figure A22. Same as Figure 3 but for  $H_{O_2min}$ .



**Deleted:**

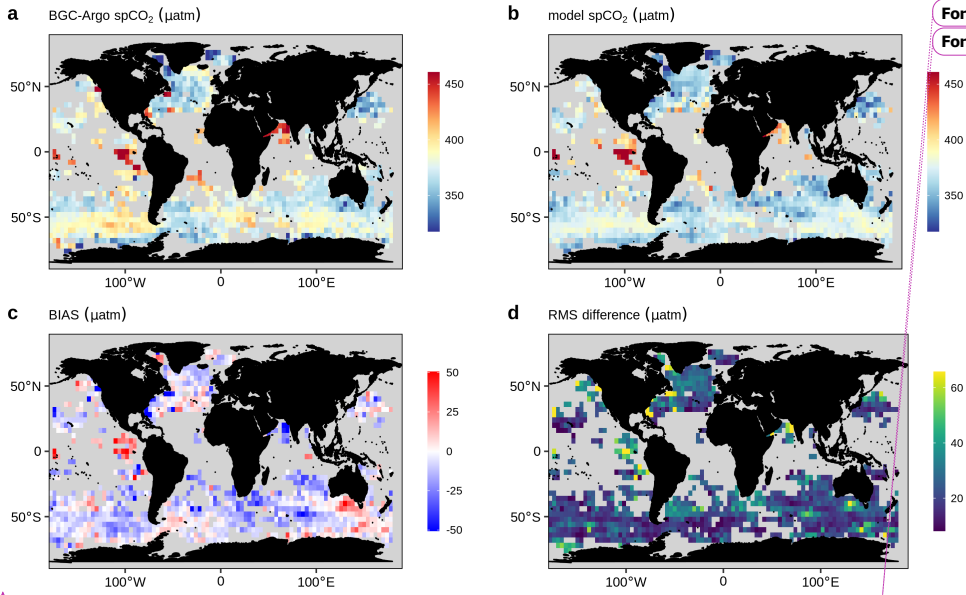
**Moved up [6]:** Figure A18. Same as Figure 3 but for

**Moved (insertion) [8]**

**Formatted:** Font colour: Text 1

**Formatted:** Font colour: Text 1

1



2

3 **Figure A23.** Same as Figure 4 but for spCO<sub>2</sub>.

4

5

6

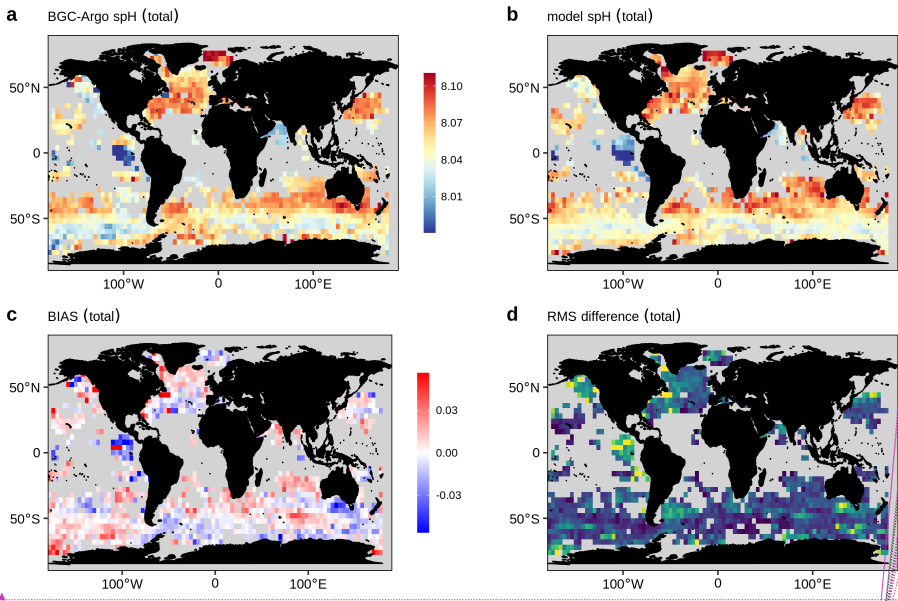
Formatted: Font colour: Text 1

Formatted: Font colour: Text 1

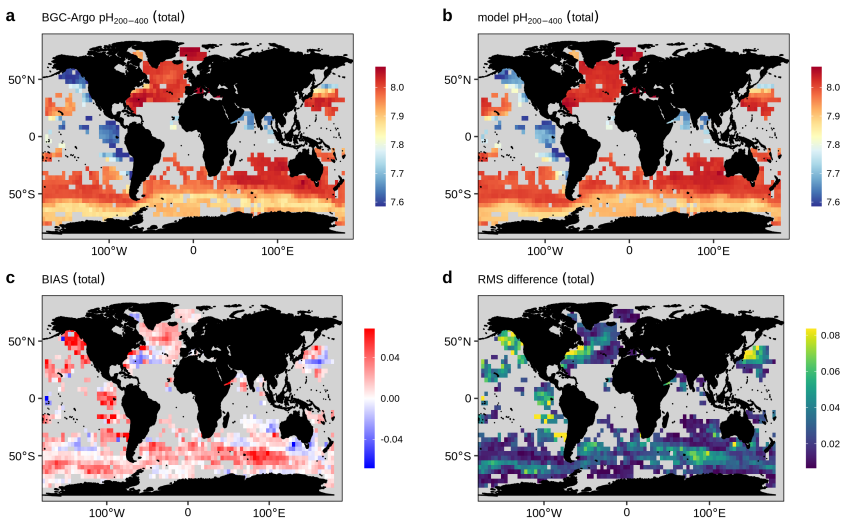
Deleted: A19

Formatted: Font colour: Text 1





1  
2 **Figure A24.** Same as Figure 4 but for spH. Note that spH is calculated from both the direct  
3 observations of the floats and as well as the estimations from CANYON-B.



4  
5

Formatted: Font colour: Text 1  
Formatted: Font colour: Text 1

8.10  
8.07

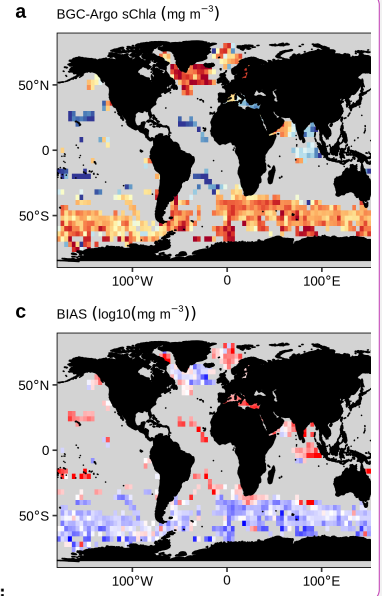
Formatted: Font colour: Text 1  
Moved up [7]: Figure A21.

Moved up [1]: is calculated from both the direct observations of the floats and as well as the estimations from CANYON-B.

Deleted: Same as Figure 4 but for pH<sub>200-400</sub>. Note that pH<sub>200-400</sub>

Moved up [8]: Figure A22.  
Deleted: A20

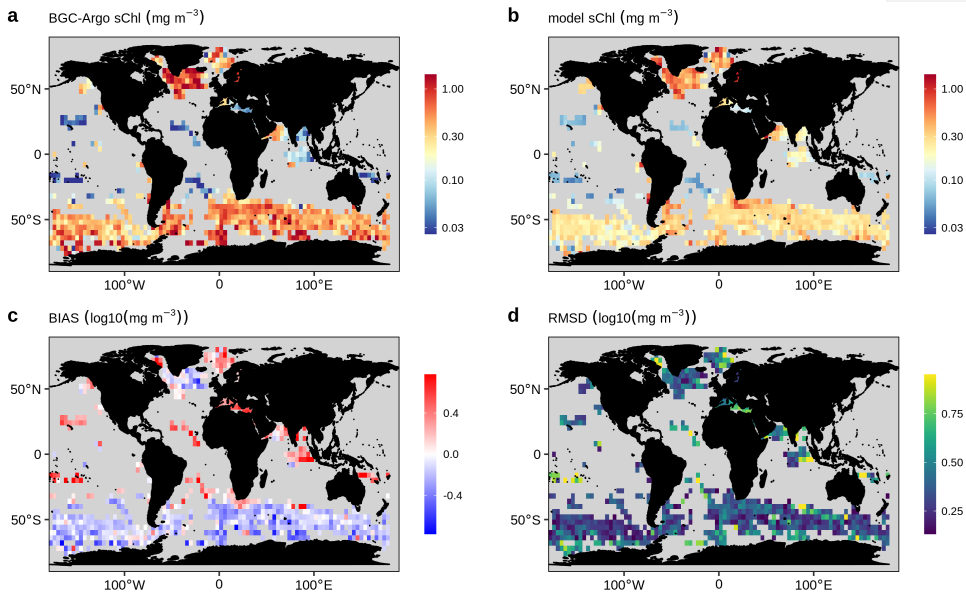
Deleted: is calculated from both the direct observations of the floats and as well as the estimations from CANYON-B. ... [6]



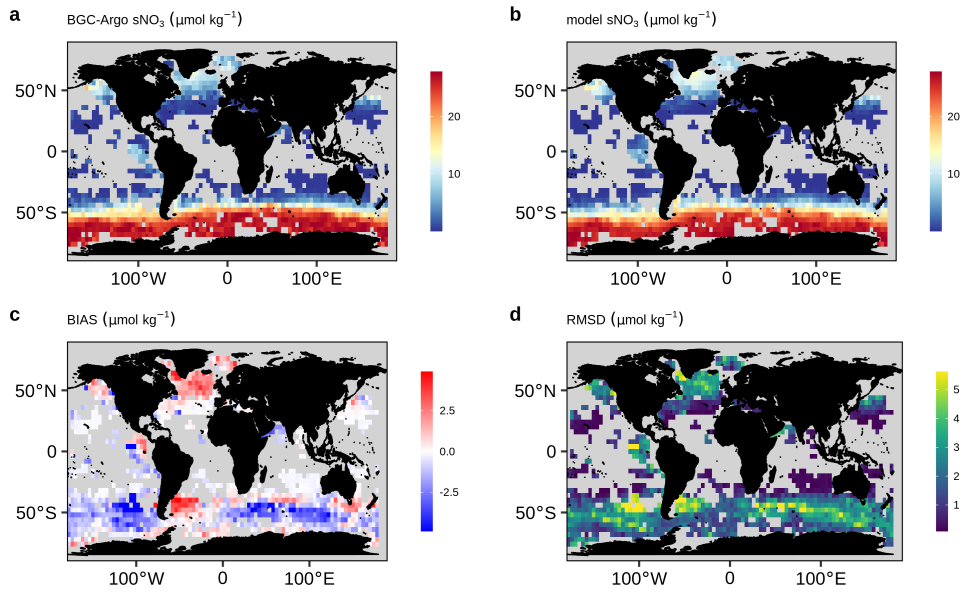
Deleted:  
Formatted: Font colour: Text 1  
Formatted: Font colour: Text 1  
Formatted: Font: 12 pt, Font colour: Text 1  
Formatted: Font colour: Text 1  
Deleted: Same as Figure 4. ... [7]

Formatted: Font colour: Text 1  
Formatted: Font: 16 pt, Font colour: Text 1  
Formatted: Indent: Left: 1,27 cm, Border: Top: (No border), Bottom: (No border), Left: (No border), Right: (No border), Between: (No border)

1 **Figure A25.** Same as Figure 4 but for  $\text{pH}_{200-400}$ . Note that  $\text{pH}_{200-400}$  is calculated from both the  
2 direct observations of the floats and as well as the estimations from CANYON-B.  
3  
4



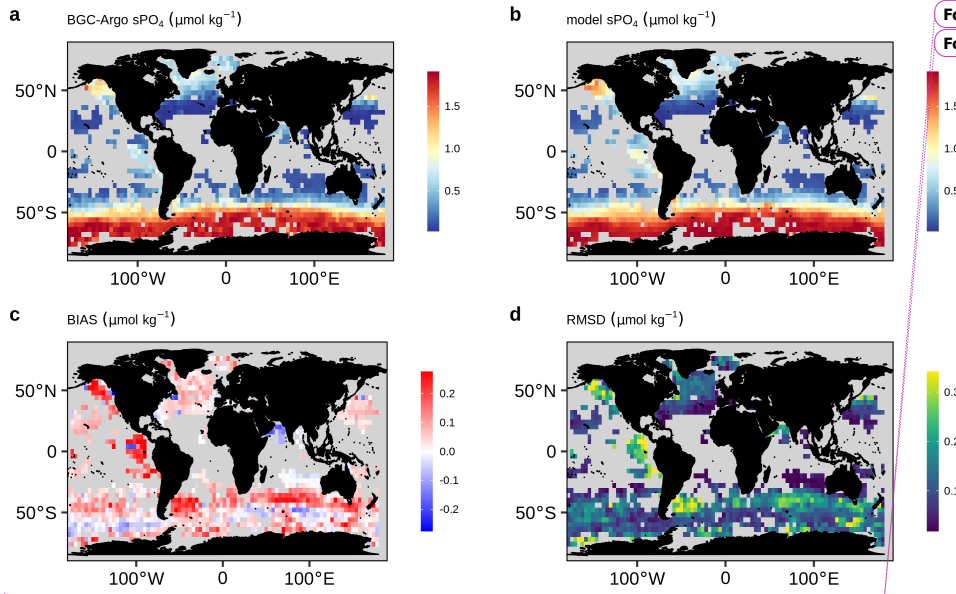
5  
6 **Figure A26.** Same as Figure 4.  
7  
8  
9



1  
2  
3  
4  
5  
6  
7

**Figure A27.** Same as Figure 4 but for  $sNO_3$ . Note that  $sNO_3$  is calculated from both the direct observations of the floats and as well as the estimations from CANYON-B.

Formatted: Font colour: Text 1



1  
2  
3  
4  
5  
6  
7

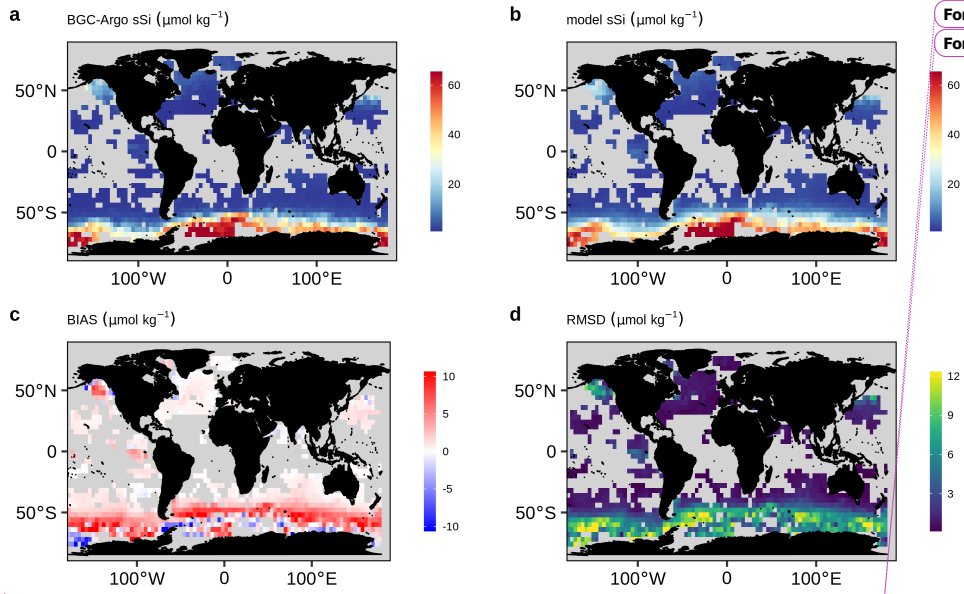
Figure A28. Same as Figure 4 but for sPO<sub>4</sub>.

Formatted: Font colour: Text 1

Formatted: Font colour: Text 1

Deleted: A24

Formatted: Font colour: Text 1

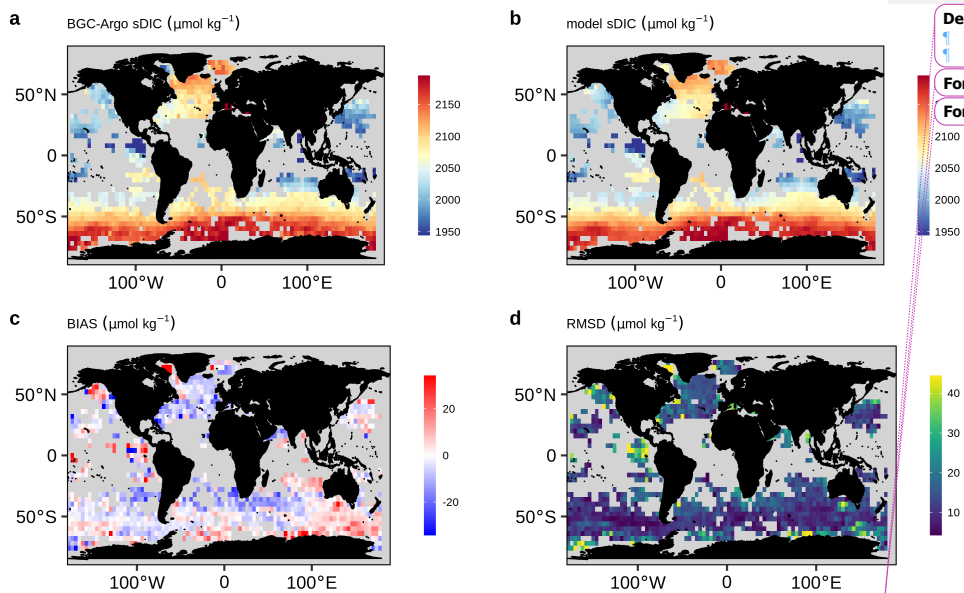


1  
2  
3  
4  
5  
6  
7

Figure A29. Same as Figure 4 but for sSi.

Formatted: Font colour: Text 1  
Formatted: Font colour: Text 1

Deleted: A25  
Formatted: Font colour: Text 1



1  
2  
3  
4

**Figure A30.** Same as Figure 4 but for sDIC.

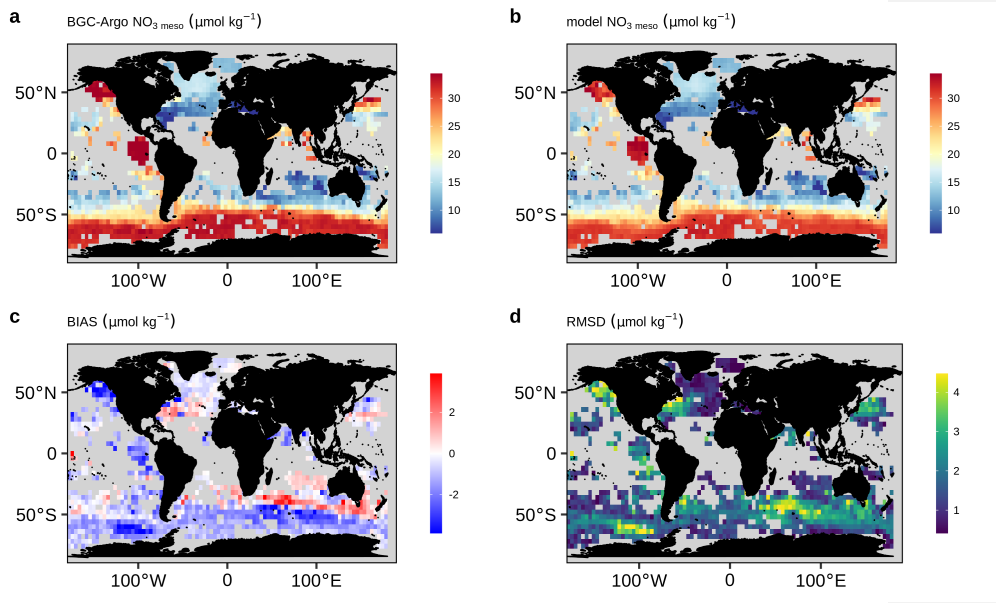
Deleted: ¶

Formatted: Font colour: Text 1

Formatted: Font colour: Text 1

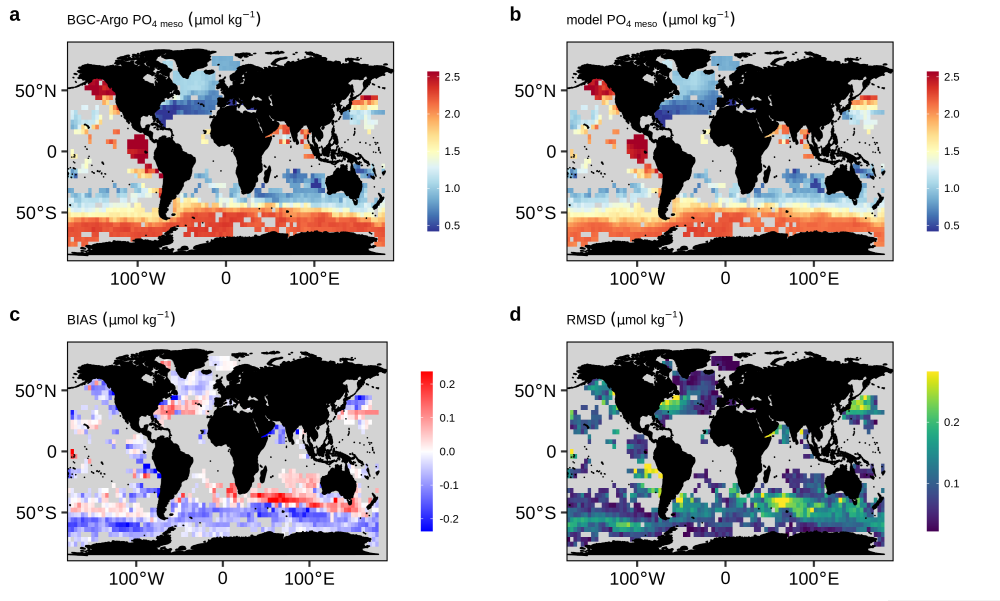
Deleted: A26

Formatted: Font colour: Text 1



1  
2  
3  
4  
5  
6  
7

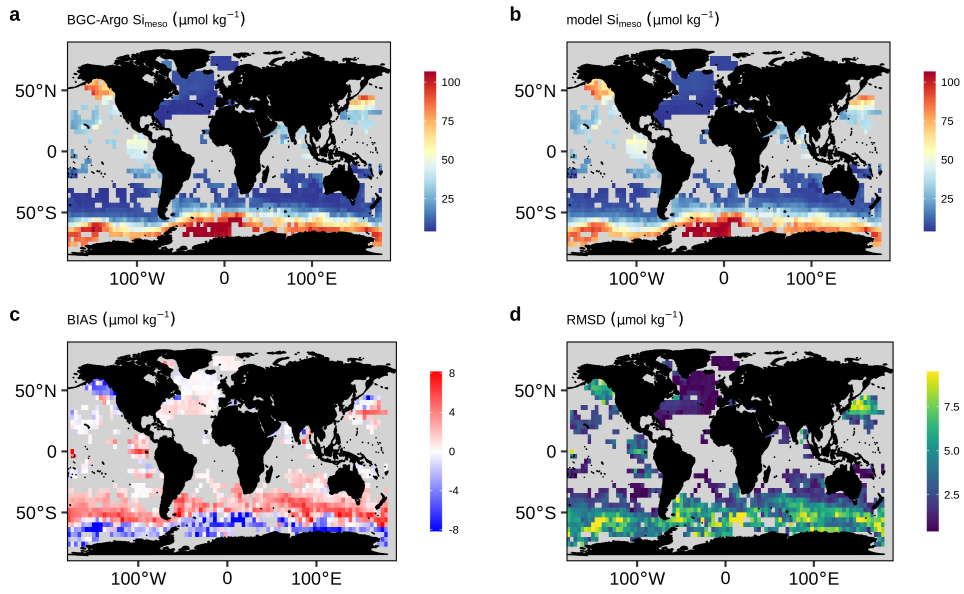
**Figure A31.** Same as Figure 4 but for  $\text{NO}_3_{\text{meso}}$ . Note that  $\text{NO}_3_{\text{meso}}$  is calculated from both the direct observations of the floats and as well as the estimations from CANYON-B.



1  
2  
3  
4  
5  
6  
7

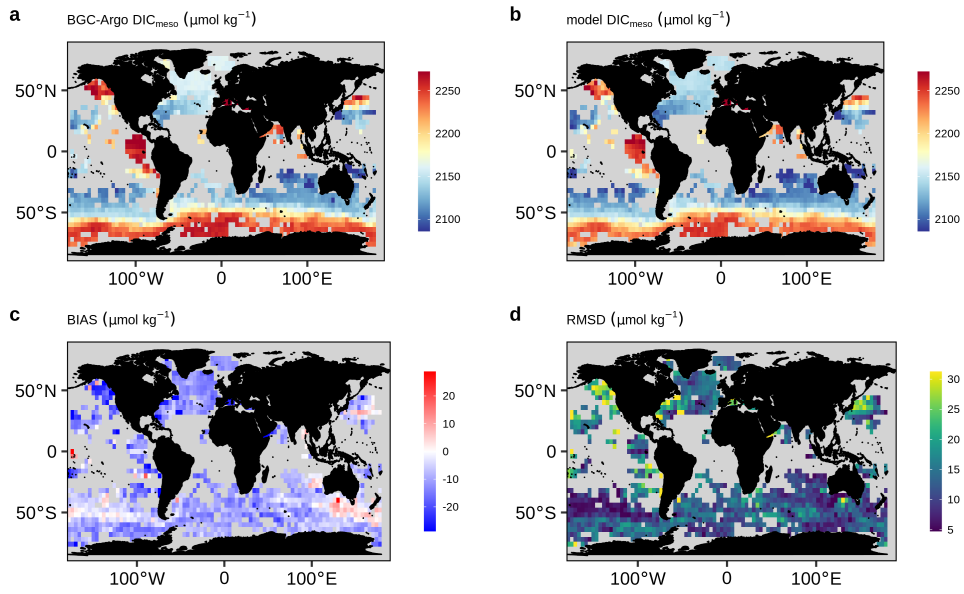
**Figure A32.** Same as Figure 4 but for  $\text{PO}_4$  meso.





1  
2  
3  
4  
5  
6  
7

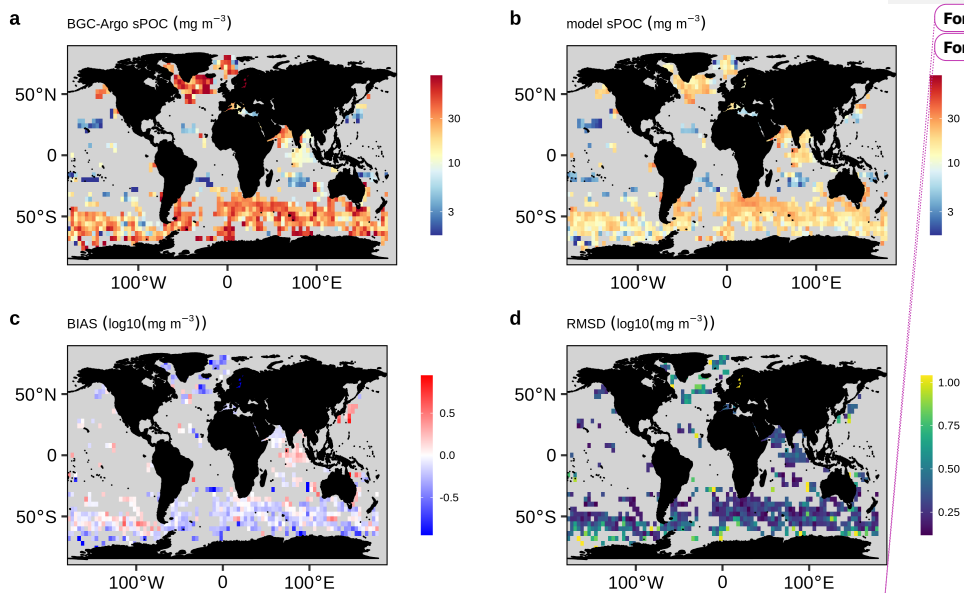
**Figure A33.** Same as Figure 4 but for  $Si_{meso}$ .



1  
2  
3  
4  
5

**Figure A34.** Same as Figure 4 but for  $\text{DIC}_{\text{meso}}$ .

Formatted: Font colour: Text 1



1  
2  
3  
4  
5  
6

**Figure A35.** Same as Figure 4 but for sPOC. The BIAS and RMSD are computed on the  $\log_{10}$ -transformed data to account that sPOC covers several orders of magnitude and it is lognormally distributed (Campbell, 1995).

Formatted: Font colour: Text 1

Formatted: Font colour: Text 1

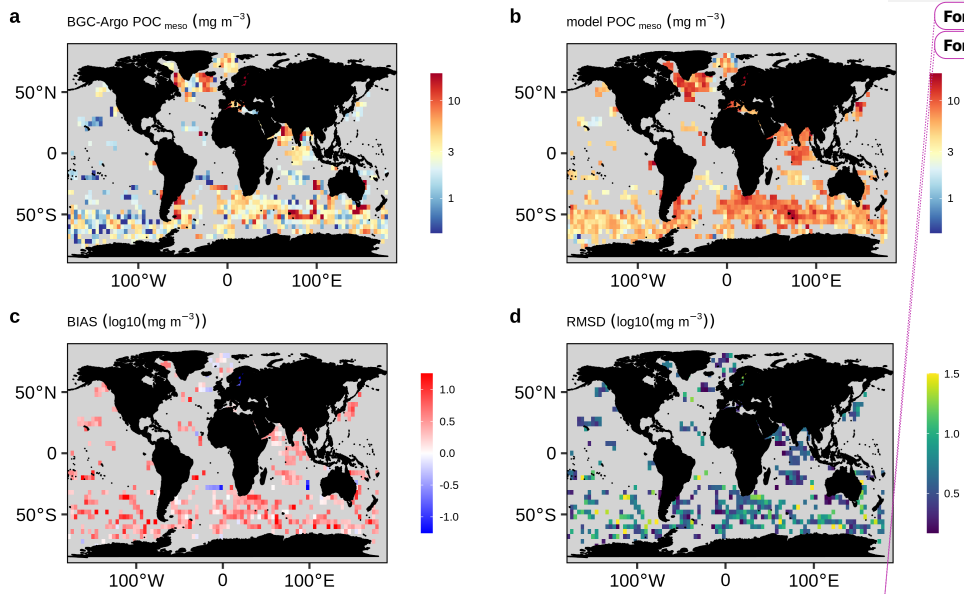
Deleted: A27

Formatted: Font colour: Text 1

Formatted: Font colour: Text 1

Formatted: Font colour: Text 1

Formatted: Font colour: Text 1

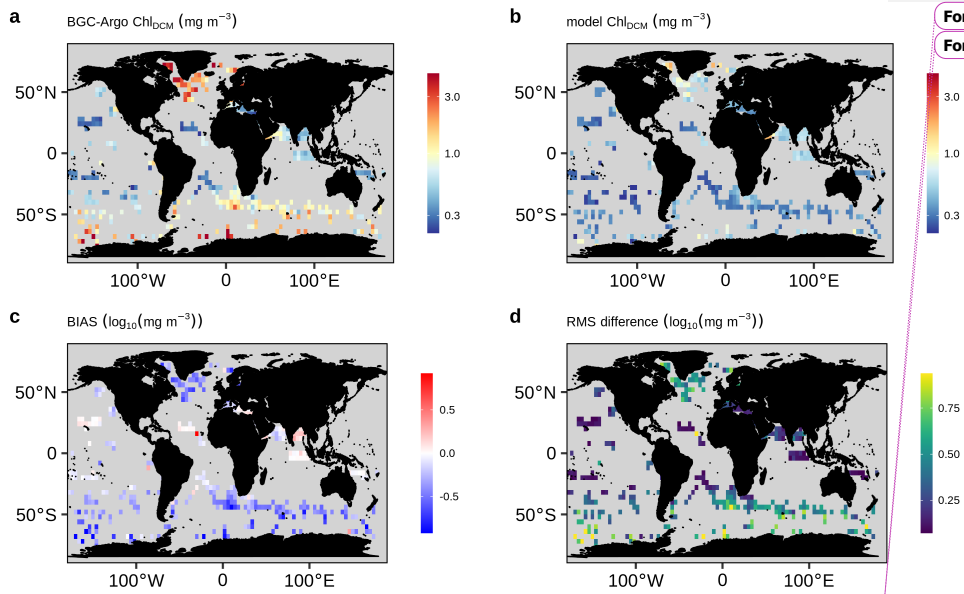


1  
2  
3  
4  
5  
6

**Figure A36.** Same as Figure 4 but for  $POC_{meso}$ . The BIAS and RMSD are computed on the  $\log_{10}$ -transformed data to account that  $POC_{meso}$  covers several orders of magnitude and it is lognormally distributed (Campbell, 1995).

Formatted: Font colour: Text 1  
Formatted: Font colour: Text 1

Deleted: A28  
Formatted: Font colour: Text 1  
Formatted: Font colour: Text 1  
Formatted: Font colour: Text 1  
Formatted: Font colour: Text 1



1  
2  
3  
4  
5  
6  
7  
8  
9

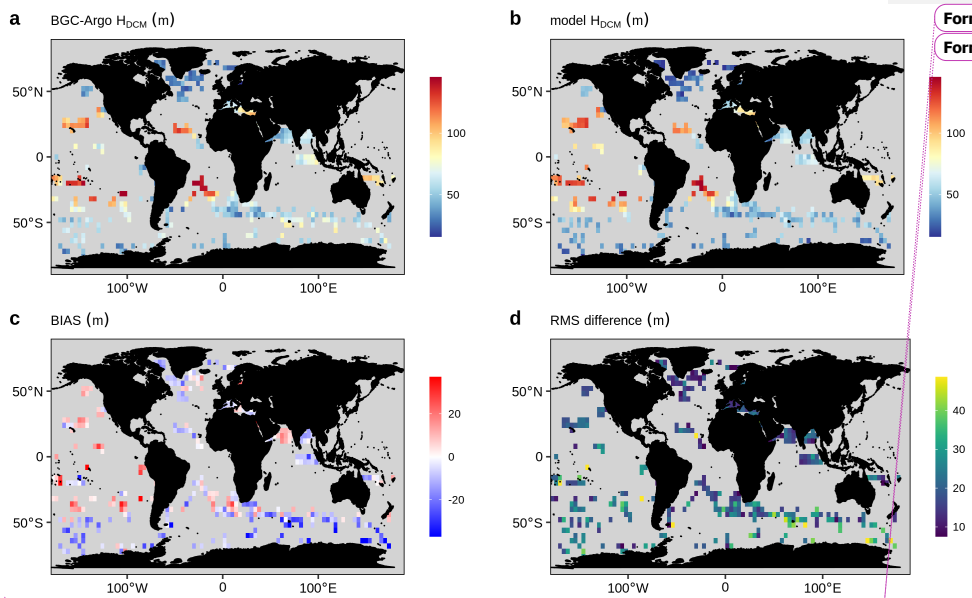
**Figure A37.** Same as Figure 4 but for  $\text{Chl}_{\text{DCM}}$ . Note that the BIAS and RMSD are computed on the  $\log_{10}$ -transformed data to account that  $\text{Chl}_{\text{DCM}}$  covers several orders of magnitude and it is lognormally distributed (Campbell, 1995).

Formatted: Font colour: Text 1

Formatted: Font colour: Text 1

Deleted: A29

Formatted: Font colour: Text 1



1  
 2 **Figure A38.** Same as Figure 4 but for  $H_{DCM}$ . Observed DCMs deeper than 250 m are not  
 3 included.

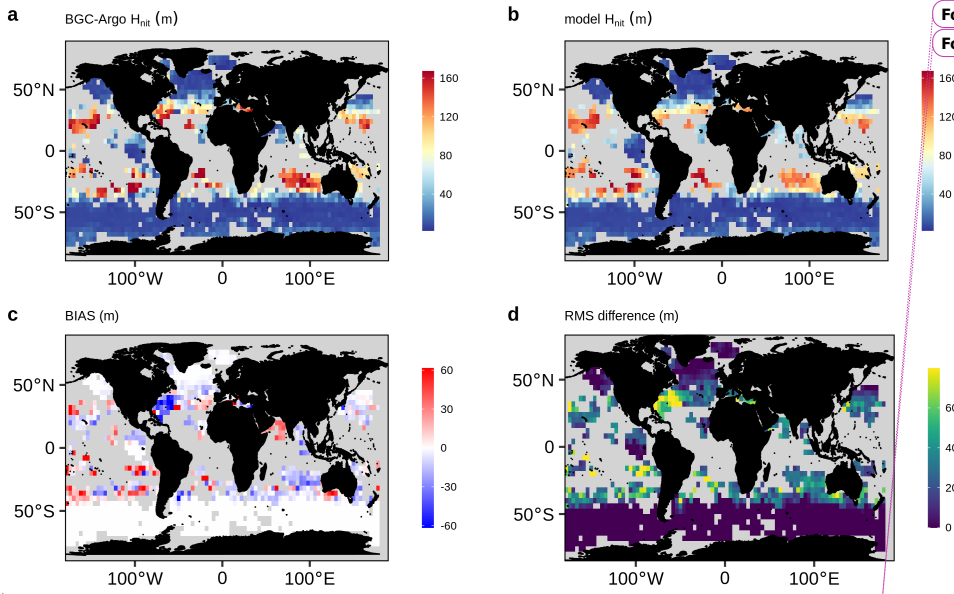
4  
 5  
 6

Formatted: Font colour: Text 1

Formatted: Font colour: Text 1

Deleted: A30

Formatted: Font colour: Text 1



1  
2  
3  
4  
5

**Figure A39.** Same as Figure 4 but for  $H_{nit}$ . Observed nitracline deeper than 250 m are not included.

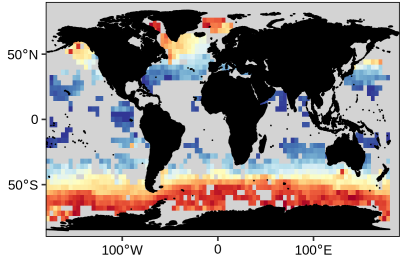
Formatted: Font colour: Text 1

Formatted: Font colour: Text 1

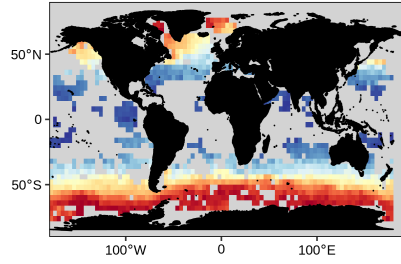
Deleted: A31

Formatted: Font colour: Text 1

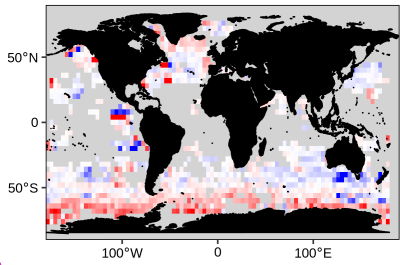
**a** BGC-Argo  $\text{sO}_2$  ( $\mu\text{mol kg}^{-1}$ )



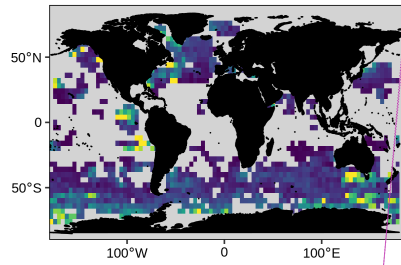
**b** model  $\text{sO}_2$  ( $\mu\text{mol kg}^{-1}$ )



**c** BIAS ( $\mu\text{mol kg}^{-1}$ )



**d** RMS difference ( $\mu\text{mol kg}^{-1}$ )



Formatted: Font colour: Text 1

Formatted: Font colour: Text 1

Deleted: A32

Formatted: Font colour: Text 1

1

2 **Figure A40.** Same as Figure 4 but for  $\text{sO}_2$ .

3

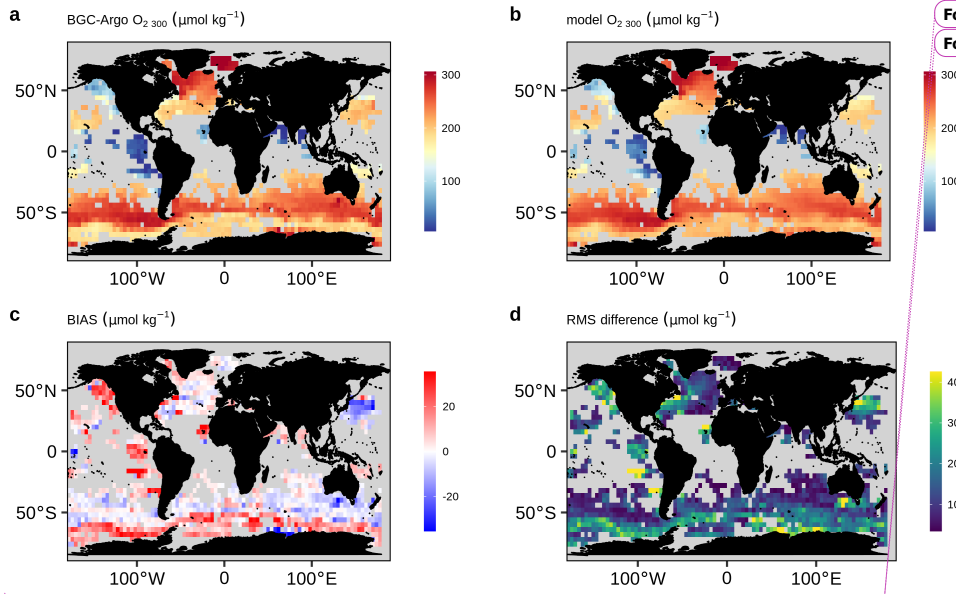
4

5

6

7





1  
2  
3  
4  
5  
6  
7

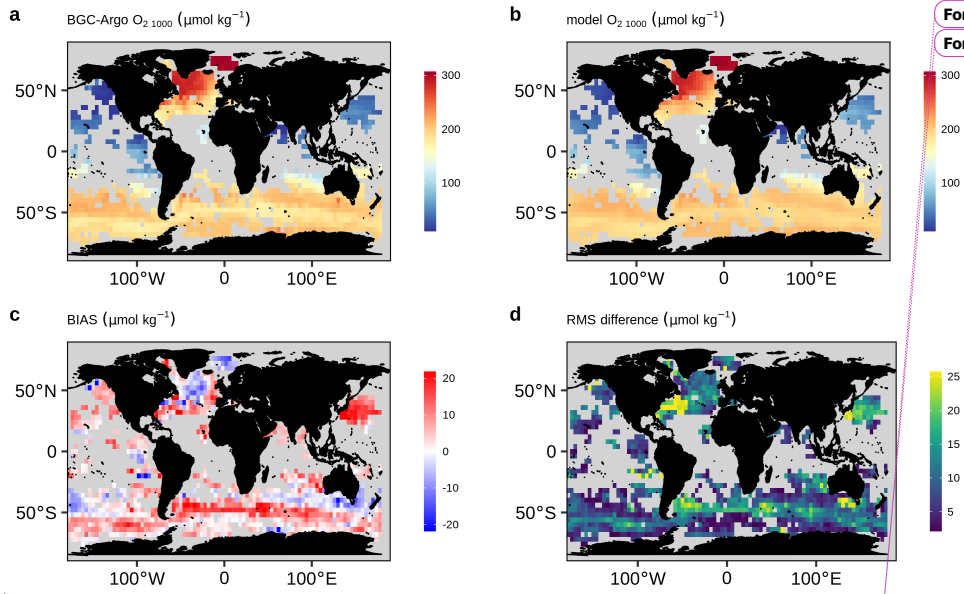
**Figure A41.** Same as Figure 4 but for  $O_{2\ 300}$ .

Formatted: Font colour: Text 1

Formatted: Font colour: Text 1

Deleted: A33

Formatted: Font colour: Text 1



1  
2  
3  
4  
5

Figure A42. Same as Figure 4 but for O<sub>2</sub> 1000.

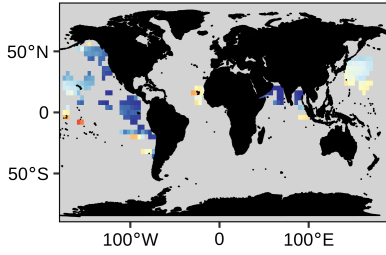
Formatted: Font colour: Text 1

Formatted: Font colour: Text 1

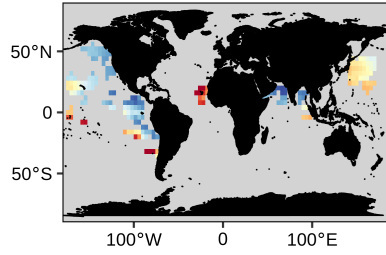
Deleted: A34

Formatted: Font colour: Text 1

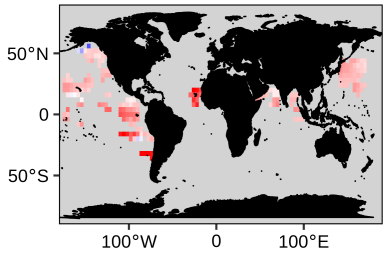
a BGC-Argo  $O_{2min}$  ( $\mu\text{mol kg}^{-1}$ )



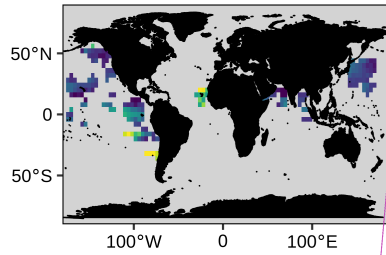
b model  $O_{2min}$  ( $\mu\text{mol kg}^{-1}$ )



c BIAS ( $\mu\text{mol kg}^{-1}$ )



d RMS difference ( $\mu\text{mol kg}^{-1}$ )



Formatted: Font colour: Text 1

Formatted: Font colour: Text 1

1

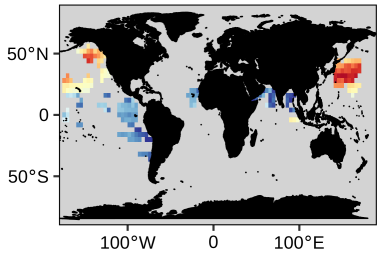
2 **Figure A43.** Same as Figure 4 but for  $O_{2min}$ .

Deleted: A35

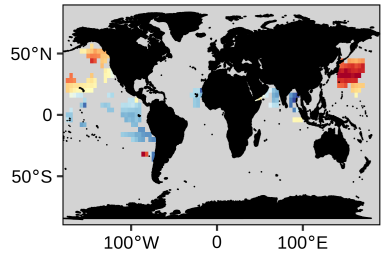
Formatted: Font colour: Text 1

3

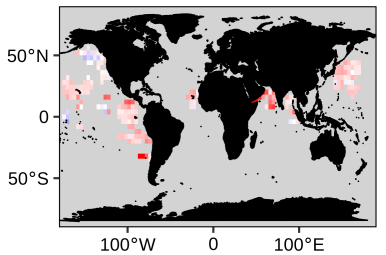
a BGC-Argo  $H_{O2min}$  (m)



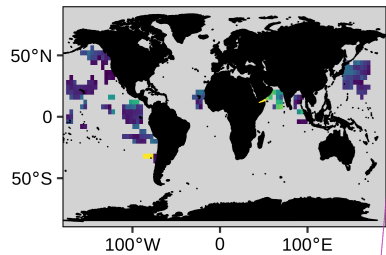
b model  $H_{O2min}$  (m)



c BIAS (m)



d RMS difference (m)



Formatted: Font colour: Text 1

Formatted: Font colour: Text 1

4

5 **Figure A44.** Same as Figure 4 but for  $H_{O2min}$ .

Deleted: A36

Formatted: Font colour: Text 1

1 **Data availability.** The BGC model data can be downloaded from the Copernicus Marine  
2 Environmental Monitoring Service  
3 ([https://resources.marine.copernicus.eu/?option=com\\_csw&view=details&product\\_id=GLOB](https://resources.marine.copernicus.eu/?option=com_csw&view=details&product_id=GLOB)  
4 [AL\\_ANALYSIS\\_FORECAST\\_BIO\\_001\\_028](https://resources.marine.copernicus.eu/?option=com_csw&view=details&product_id=GLOB)). The BGC-Argo data were downloaded from  
5 the Argo Global Data Assembly Centre in France (<ftp://ftp.ifremer.fr/argo/>).

6  
7 **Authors Contribution:** AM, GC, FD, SS and VT originated the study. AM, HC, FD, RS and  
8 VT designated the study. AM and RS process the BGC-Argo floats data. PL processed the  
9 BGC-Argo float in the Mediterranean Sea and run the Mediterranean BGC model. AM  
10 analysed the data. AM wrote the first draft of the manuscript. HC, GC, FD, EG, PL, CP,  
11 SS,RS,VT and AT contributed to the subsequent drafts. All authors read and approved the  
12 final draft.

13  
14 **Competing Interests:** The authors declare no competing financial interests.

15  
16 **Materials and correspondence:** Correspondence and request for material should be  
17 addressed to [mignot@mercator-ocean.fr](mailto:mignot@mercator-ocean.fr)

18  
19 **Acknowledgements:** This study has been conducted using the Copernicus Marine Service  
20 products (CMEMS). The BGC-Argo data were collected and made freely available by the  
21 International Argo program and the national programs that contribute to it  
22 (<https://www.argo.jcommops.org>). The Argo program is part of the Global Ocean Observing  
23 System. Part of this work was performed within the framework of the BIOOPTIMOD and  
24 MASSIMILI CMEMS Service Evolution Projects. This paper represents a contribution to the  
25 following research projects: NAOS (funded by the Agence Nationale de la Recherche in the  
26 framework of the French “Equipement d’avenir” program, grant ANR J11R107-F), remOcean  
27 (funded by the European Research Council, grant 246777), and the French Bio-Argo program  
28 (BGC-Argo France; funded by CNES-TOSCA, LEFE-GMMC).

29  
30

Formatted: Font colour: Text 1

Formatted: Font colour: Text 1

Formatted: Font colour: Text 1

Formatted: Font colour: Text 1

## 1 References

2

3 Aumont, O., Ethé, C., Tagliabue, A., Bopp, L., and Gehlen, M.: PISCES-v2: an ocean  
4 biogeochemical model for carbon and ecosystem studies, *Geosci. Model Dev.*, 8, 2465–2513,  
5 <https://doi.org/10.5194/gmd-8-2465-2015>, 2015.

Formatted: Font colour: Text 1

Deleted: .

Deleted: (8),

6 Babin, M., Stramski, D., Ferrari, G. M., Claustre, H., Bricaud, A., Obolensky, G., and  
7 Hoepffner, N.: Variations in the light absorption coefficients of phytoplankton, nonalgal  
8 particles, and dissolved organic matter in coastal waters around Europe, *J. Geophys. Res.*  
9 *Oceans*, 108, 2003.

Deleted: .

Deleted: (C7),

10 Baird, M. E., Cherukuru, N., Jones, E., Margvelashvili, N., Mongin, M., Oubelkheir, K.,  
11 Ralph, P. J., Rizwi, F., Robson, B. J., Schroeder, T., Skerratt, J., Steven, A. D. L., and Wild-  
12 Allen, K. A.: Remote-sensing reflectance and true colour produced by a coupled  
13 hydrodynamic, optical, sediment, biogeochemical model of the Great Barrier Reef, Australia:  
14 Comparison with satellite data, *Environ. Model. Softw.*, 78, 79–96,  
15 <https://doi.org/10.1016/j.envsoft.2015.11.025>, 2016.

Deleted: .

16 Barbieux, M., Uitz, J., Gentili, B., Pasqueron de Fommervault, O., Mignot, A., Poteau, A.,  
17 Schmechtig, C., Taillandier, V., Leymarie, E., Penker&apos;h, C.,  
18 D&apos;Ortenzio, F., Claustre, H., and Bricaud, A.: Bio-optical characterization of  
19 subsurface chlorophyll maxima in the Mediterranean Sea from a Biogeochemical-Argo float  
20 database, *Biogeosciences*, 16, 1321–1342, <https://doi.org/10.5194/bg-16-1321-2019>, 2019.

Deleted: .

Deleted: (6),

21 Biogeochemical-Argo Planning Group: The scientific rationale, design and implementation  
22 plan for a Biogeochemical-Argo float array, <https://doi.org/10.13155/46601>, 2016.

Deleted: .

23 Bittig, H. C., Steinhoff, T., Claustre, H., Fiedler, B., Williams, N. L., Sauzède, R., Körtzinger,  
24 A., and Gattuso, J.-P.: An alternative to static climatologies: robust estimation of open ocean  
25 CO<sub>2</sub> variables and nutrient concentrations from T, S, and O<sub>2</sub> data using Bayesian neural  
26 networks, *Front. Mar. Sci.*, 5, 328, 2018.

Deleted: .

27 Bittig, H. C., Maurer, T. L., Plant, J. N., Wong, A. P., Schmechtig, C., Claustre, H., Trull, T.  
28 W., Udaya Bhaskar, T. V. S., Boss, E., and Dall’Olmo, G.: A BGC-Argo guide: Planning,  
29 deployment, data handling and usage, *Front. Mar. Sci.*, 6, 502, 2019.

Deleted: .

30 Bopp, L., Aumont, O., Cadule, P., Alvain, S., and Gehlen, M.: Response of diatoms  
31 distribution to global warming and potential implications: A global model study, *Geophys.*  
32 *Res. Lett.*, 32, <https://doi.org/10.1029/2005GL023653>, 2005.

Deleted: .

Deleted: (19),

33 Bosc, E., Bricaud, A., and Antoine, D.: Seasonal and interannual variability in algal biomass  
34 and primary production in the Mediterranean Sea, as derived from 4 years of SeaWiFS  
35 observations, *Glob. Biogeochem. Cycles*, 18, <https://doi.org/10.1029/2003GB002034>, 2004.

Deleted: .

Deleted: (1),

36 Breitburg, D., Levin, L. A., Oschlies, A., Grégoire, M., Chavez, F. P., Conley, D. J., Garçon,  
37 V., Gilbert, D., Gutiérrez, D., Isensee, K., Jacinto, G. S., Limburg, K. E., Montes, I., Naqvi, S.  
38 W. A., Pitcher, G. C., Rabalais, N. N., Roman, M. R., Rose, K. A., Seibel, B. A., Telszewski,  
39 M., Yasuhara, M., and Zhang, J.: Declining oxygen in the global ocean and coastal waters,  
40 *Science*, 359, <https://doi.org/10.1126/science.aam7240>, 2018.

Deleted: .

Deleted: (6371),

1	Briggs, N., Perry, M. J., Cetinić, I., Lee, C., D'Asaro, E., Gray, A. M., and Rehm, E.: High-	Deleted: .
2	resolution observations of aggregate flux during a sub-polar North Atlantic spring bloom,	
3	Deep Sea Res. Part Oceanogr. Res. Pap., 58, 1031–1039,	Deleted: (10),
4	https://doi.org/10.1016/j.dsr.2011.07.007, 2011.	
5	Campbell, J. W.: The lognormal distribution as a model for bio-optical variability in the sea,	
6	J. Geophys. Res. Oceans, 100, 13237–13254, https://doi.org/10.1029/95JC00458, 1995.	Deleted: (C7),
7	Canu, D. M., Ghermandi, A., Nunes, P. A., Lazzari, P., Cossarini, G., and Solidoro, C.:	Deleted: .
8	Estimating the value of carbon sequestration ecosystem services in the Mediterranean Sea: An	
9	ecological economics approach, Glob. Environ. Change, 32, 87–95, 2015.	
10	Capuzzo, E., Lynam, C. P., Barry, J., Stephens, D., Forster, R. M., Greenwood, N.,	
11	McQuatters-Gollop, A., Silva, T., van Leeuwen, S. M., and Engelhard, G. H.: A decline in	Deleted: .
12	primary production in the North Sea over 25 years, associated with reductions in zooplankton	
13	abundance and fish stock recruitment, Glob. Change Biol., 24, e352–e364,	Deleted: (1),
14	https://doi.org/10.1111/gcb.13916, 2018.	
15	<u>Cermeno, P., Dutkiewicz, S., Harris, R. P., Follows, M., Schofield, O., and Falkowski, P. G.:</u>	Deleted: Cetinic, I., Perry
16	<u>The role of nutricline depth in regulating the ocean carbon cycle, Proc. Natl. Acad. Sci., 105,</u>	Deleted: J., Briggs, N. T., Kallin, E., D'Asaro, E. A.
17	<u>20344–20349, https://doi.org/10.1073/pnas.0811302106, 2008.</u>	Deleted: Lee, C. M.: Particulate organic
18	Claustre, H., Johnson, K. S., and Takeshita, Y.: Observing the Global Ocean with	Deleted: and inherent optical properties during 2008 North Atlantic Bloom Experiment, J. Geophys. Res.-Oceans, 117
19	Biogeochemical-Argo, Annu. Rev. Mar. Sci., 12, annurev-marine-010419-010956,	Deleted: 1029/2011JC007771, 2012
20	https://doi.org/10.1146/annurev-marine-010419-010956, 2020.	Deleted: .
21	Cossarini, G., Lazzari, P., and Solidoro, C.: Spatiotemporal variability of alkalinity in the	Deleted: (1),
22	Mediterranean Sea, Biogeosciences, 12, 1647–1658, https://doi.org/10.5194/bg-12-1647-	Deleted: .
23	2015, 2015.	Deleted: (6),
24	Cossarini, G., Mariotti, L., Feudale, L., Mignot, A., Salon, S., Taillandier, V., Teruzzi, A., and	Deleted: .
25	D'Ortenzio, F.: Towards operational 3D-Var assimilation of chlorophyll Biogeochemical-	
26	Argo float data into a biogeochemical model of the Mediterranean Sea, Ocean Model., 133,	
27	112–128, https://doi.org/10.1016/j.ocemod.2018.11.005, 2019.	
28	Crowder, L. B., Hazen, E. L., Avissar, N., Bjorkland, R., Latanich, C., and Ogburn, M. B.:	Deleted: .
29	The Impacts of Fisheries on Marine Ecosystems and the Transition to Ecosystem-Based	
30	Management, Annu. Rev. Ecol. Evol. Syst., 39, 259–278,	Deleted: (1),
31	https://doi.org/10.1146/annurev.ecolsys.39.110707.173406, 2008.	
32	Cullen, J. J.: Subsurface Chlorophyll Maximum Layers: Enduring Enigma or Mystery	
33	Solved?, Annu. Rev. Mar. Sci., 7, 207–239, https://doi.org/10.1146/annurev-marine-010213-	Deleted: (1),
34	135111, 2015.	
35	Dale, T., Rey, F., and Heimdal, B. R.: Seasonal development of phytoplankton at a high	Deleted: .
36	latitude oceanic site, Sarsia, 84, 419–435, 1999.	Deleted: (5–6),
37	Dall'Olmo, G. and Mork, K. A.: Carbon export by small particles in the Norwegian Sea,	
38	Geophys. Res. Lett., 41, 2921–2927, https://doi.org/10.1002/2014GL059244, 2014.	Deleted: (8),
39	Doney, S. C., Lima, I., Moore, J. K., Lindsay, K., Behrenfeld, M. J., Westberry, T. K.,	
40	Mahowald, N., Glover, D. M., and Takahashi, T.: Skill metrics for confronting global upper	Deleted: .

1 ocean ecosystem-biogeochemistry models against field and remote sensing data, *J. Mar. Syst.*,  
2 76, 95–112, <https://doi.org/10.1016/j.jmarsys.2008.05.015>, 2009.

3 D’Ortenzio, F., Lavigne, H., Besson, F., Claustre, H., Coppola, L., Garcia, N., Laes-Huon, A.,  
4 Le Reste, S., Malarde, D., Migon, C., Morin, P., Mortier, L., Poteau, A., Prieur, L.,  
5 Raimbault, P., and Testor, P.: Observing mixed layer depth, nitrate and chlorophyll  
6 concentrations in the northwestern Mediterranean: A combined satellite and NO<sub>3</sub> profiling  
7 floats experiment, *Geophys. Res. Lett.*, 41, 2014GL061020,  
8 <https://doi.org/10.1002/2014GL061020>, 2014.

9 Dutkiewicz, S., Hickman, A. E., Jahn, O., Gregg, W. W., Mouw, C. B., and Follows, M. J.:  
10 Capturing optically important constituents and properties in a marine biogeochemical and  
11 ecosystem model, *Biogeosciences*, 12, 4447–4481, <https://doi.org/10.5194/bg-12-4447-2015>,  
12 2015.

13 Eriksen, M., Lebreton, L. C. M., Carson, H. S., Thiel, M., Moore, C. J., Borerro, J. C.,  
14 Galgani, F., Ryan, P. G., and Reisser, J.: Plastic Pollution in the World’s Oceans: More than 5  
15 Trillion Plastic Pieces Weighing over 250,000 Tons Afloat at Sea, *PLoS ONE*, 9, e111913,  
16 <https://doi.org/10.1371/journal.pone.0111913>, 2014.

17 Evans, G. T. and Parslow, J. S.: A Model of Annual Plankton Cycles, *Biol. Oceanogr.*, 3,  
18 327–347, <https://doi.org/10.1080/01965581.1985.10749478>, 1985.

19 [Evers-King, H., Martinez-Vicente, V., Brewin, R. J. W., Dall’Olmo, G., Hickman, A. E.,](#)  
20 [Jackson, T., Kostadinov, T. S., Krasemann, H., Loisel, H., Röttgers, R., Roy, S., Stramski, D.,](#)  
21 [Thomalla, S., Platt, T., and Sathyendranath, S.: Validation and Intercomparison of Ocean](#)  
22 [Color Algorithms for Estimating Particulate Organic Carbon in the Oceans, \*Front. Mar. Sci.\*,](#)  
23 [4, 251, <https://doi.org/10.3389/fmars.2017.00251>, 2017.](#)

24 Fennel, K., Gehlen, M., Bresseur, P., Brown, C. W., Ciavatta, S., Cossarini, G., Crise, A.,  
25 Edwards, C. A., Ford, D., Friedrichs, M. A. M., Gregoire, M., Jones, E., Kim, H.-C.,  
26 Lamouroux, J., Murtugudde, R., Perruche, C., and the GODAE OceanView Marine  
27 Ecosystem Analysis and Prediction Task Team: Advancing Marine Biogeochemical and  
28 Ecosystem Reanalyses and Forecasts as Tools for Monitoring and Managing Ecosystem  
29 Health, *Front. Mar. Sci.*, 6, 89, <https://doi.org/10.3389/fmars.2019.00089>, 2019.

30 Ford, D.: Assimilating synthetic Biogeochemical-Argo and ocean colour observations into a  
31 global ocean model to inform observing system design, *Biogeochemistry: Open Ocean*,  
32 <https://doi.org/10.5194/bg-2020-152>, 2020.

33 Friedlingstein, P., Jones, M. W., O’Sullivan, M., Andrew, R. M., Hauck, J., Peters, G. P.,  
34 Peters, W., Pongratz, J., Sitch, S., Le Quéré, C., Bakker, D. C. E., Canadell, J. G., Ciais, P.,  
35 Jackson, R. B., Anthoni, P., Barbero, L., Bastos, A., Bastrikov, V., Becker, M., Bopp, L.,  
36 Buitenhuis, E., Chandra, N., Chevallier, F., Chini, L. P., Currie, K. I., Feely, R. A., Gehlen,  
37 M., Gilfillan, D., Gkritzalis, T., Goll, D. S., Gruber, N., Gutekunst, S., Harris, I., Haverd, V.,  
38 Houghton, R. A., Hurtt, G., Ilyina, T., Jain, A. K., Joetzjer, E., Kaplan, J. O., Kato, E., Klein  
39 Goldewijk, K., Korsbakken, J. I., Landschützer, P., Lauvset, S. K., Lefèvre, N., Lenton, A.,  
40 Lienert, S., Lombardozi, D., Marland, G., McGuire, P. C., Melton, J. R., Metzl, N., Munro,  
41 D. R., Nabel, J. E. M. S., Nakaoka, S.-I., Neill, C., Omar, A. M., Ono, T., Peregon, A.,  
42 Pierrot, D., Poulter, B., Rehder, G., Resplandy, L., Robertson, E., Rödenbeck, C., Séférian,  
43 R., Schwinger, J., Smith, N., Tans, P. P., Tian, H., Tilbrook, B., Tubiello, F. N., van der Werf,

Deleted: (1),

Deleted: .

Deleted: (18),

Deleted: .

Deleted: (14),

Deleted: .

Deleted: edited by H. G. Dam,

Deleted: (12),

Deleted: (3),

Deleted: .

Deleted: preprint,

Deleted: ..

1	G. R., Wiltshire, A. J., and Zaehle, S.: Global Carbon Budget 2019, <i>Earth Syst. Sci. Data</i> , <b>11</b> ,	Deleted: .
2	1783–1838, <a href="https://doi.org/10.5194/essd-11-1783-2019">https://doi.org/10.5194/essd-11-1783-2019</a> , 2019.	Deleted: (4),
3	<a href="#">Galí, M., Falls, M., Claustre, H., Aumont, O., and Bernardello, R.: Bridging the gaps between</a>	
4	<a href="#">particulate backscattering measurements and modeled particulate organic carbon in the ocean,</a>	
5	<a href="#">Biogeochemistry: Open Ocean</a> , <a href="https://doi.org/10.5194/bg-2021-201">https://doi.org/10.5194/bg-2021-201</a> , 2021.	
6	<a href="#">Gasparin, F., Cravatte, S., Greiner, E., Perruche, C., Hamon, M., Van Gennip, S., and</a>	
7	<a href="#">Lellouche, J.-M.: Excessive productivity and heat content in tropical Pacific analyses:</a>	
8	<a href="#">Disentangling the effects of in situ and altimetry assimilation</a> , <i>Ocean Model.</i> , <b>160</b> , 101768,	
9	<a href="https://doi.org/10.1016/j.ocemod.2021.101768">https://doi.org/10.1016/j.ocemod.2021.101768</a> , 2021.	
10	Gehlen, M., Bopp, L., Emprin, N., Aumont, O., Heinze, C., and Ragueneau, O.: Reconciling	Deleted: .
11	surface ocean productivity, export fluxes and sediment composition in a global	
12	biogeochemical ocean model, <i>Biogeosciences</i> , <b>3</b> , 521–537, <a href="https://doi.org/10.5194/bg-3-521-2006">https://doi.org/10.5194/bg-3-521-</a>	Deleted: (4),
13	2006, 2006.	
14	Gehlen, M., Gangstø, R., Schneider, B., Bopp, L., Aumont, O., and Ethe, C.: The fate of	Deleted: .
15	pelagic CaCO <sub>3</sub> production in a high CO <sub>2</sub> ocean: a model study, <i>Biogeosciences</i> , <b>4</b> , 505–519,	Deleted: (4),
16	<a href="https://doi.org/10.5194/bg-4-505-2007">https://doi.org/10.5194/bg-4-505-2007</a> , 2007.	
17	Gittings, J. A., Raitsos, D. E., Kheireddine, M., Racault, M.-F., Claustre, H., and Hoteit, I.:	Deleted: .
18	Evaluating tropical phytoplankton phenology metrics using contemporary tools, <i>Sci. Rep.</i> , <b>9</b> ,	Deleted: (1),
19	1–9, 2019.	
20	Gregg, W. W. and Rousseaux, C. S.: Directional and spectral irradiance in ocean models:	
21	effects on simulated global phytoplankton, nutrients, and primary production, <i>Front. Mar.</i>	
22	<i>Sci.</i> , <b>3</b> , 240, 2016.	
23	Gutknecht, E., Reffray, G., Mignot, A., Dabrowski, T., and Sotillo, M. G.: Modelling the	Deleted: .
24	marine ecosystem of Iberia-Biscay-Ireland (IBI) European waters for CMEMS operational	
25	applications, <i>Ocean Sci.</i> , <b>15</b> , 1489–1516, <a href="https://doi.org/10.5194/os-15-1489-2019">https://doi.org/10.5194/os-15-1489-2019</a> , 2019.	Deleted: (6),
26	<a href="#">Hipsey, M. R., Gal, G., Arhonditsis, G. B., Carey, C. C., Elliott, J. A., Frassl, M. A., Janse, J.</a>	Deleted: Herbland, A. and Voituriez, B.: Hydrological structure
27	<a href="#">H. de Mora, L., and Robson, B. J.: A system of metrics for the assessment and improvement</a>	analysis for estimating the primary production in the tropical Atlantic
28	<a href="#">of aquatic ecosystem models</a> , <i>Environ. Model. Softw.</i> , <b>128</b> , 104697,	Ocean, <i>J Mar Res</i> , <b>37</b> (1), 87–101, 1979.†
29	<a href="https://doi.org/10.1016/j.envsoft.2020.104697">https://doi.org/10.1016/j.envsoft.2020.104697</a> , 2020.	
30	Iida, Y., Takatani, Y., Kojima, A., and Ishii, M.: Global trends of ocean CO <sub>2</sub> sink and ocean	Deleted: .
31	acidification: an observation-based reconstruction of surface ocean inorganic carbon	
32	variables, <i>J. Oceanogr.</i> , 1–36, 2020.	
33	Johnson, Plant, J. N., Coletti, L. J., Jannasch, H. W., Sakamoto, C. M., Riser, S. C., Swift, D.	Deleted: .
34	D., Williams, N. L., Boss, E., Haëntjens, N., Talley, L. D., and Sarmiento, J. L.:	
35	Biogeochemical sensor performance in the SOCCOM profiling float array: SOCCOM	
36	BIOGEOCHEMICAL SENSOR PERFORMANCE, <i>J. Geophys. Res. Oceans</i> , <b>122</b> , 6416–	Deleted: (8),
37	6436, <a href="https://doi.org/10.1002/2017JC012838">https://doi.org/10.1002/2017JC012838</a> , 2017.	
38	Johnson, Plant, J. N., and Maurer, T. L.: Processing BGC-Argo pH data at the DAC level,	Deleted: .
39	<a href="#">2018a</a> .	Deleted: <a href="https://archimer.ifremer.fr/doc/00460/57195/">https://archimer.ifremer.fr/doc/00460/57195/</a> , last access: 22 April 2020a, 2018



1 Johnson, Pasquero De Fommervault, O., Serra, R., D'Ortenzio, F., Schmechtig, C., Claustre,  
2 H., and Poteau, A.: Processing Bio-Argo nitrate concentration at the DAC Level, **2018b**.

3 Key, R. M., Olsen, A., van Heuven, S., Lauvset, S. K., Velo, A., Lin, X., Schirnack, C.,  
4 Kozyr, A., Tanhua, T., and Hoppema, M.: Global Ocean Data Analysis Project, Version 2  
5 (GLODAPv2), Carbon Dioxide Information Analysis Center, Oak Ridge Nat Lab, 2015.

6 Kwiatkowski, L., Torres, O., Bopp, L., Aumont, O., Chamberlain, M., Christian, J. R., Dunne,  
7 J. P., Gehlen, M., Ilyina, T., John, J. G., Lenton, A., Li, H., Lovenduski, N. S., Orr, J. C.,  
8 Palmieri, J., Santana-Falcón, Y., Schwinger, J., Séférian, R., Stock, C. A., Tagliabue, A.,  
9 Takano, Y., Tjiputra, J., Toyama, K., Tsujino, H., Watanabe, M., Yamamoto, A., Yool, A.,  
10 and Ziehn, T.: Twenty-first century ocean warming, acidification, deoxygenation, and upper-  
11 ocean nutrient and primary production decline from CMIP6 model projections,  
12 *Biogeosciences*, **17**, 3439–3470, <https://doi.org/10.5194/bg-17-3439-2020>, 2020.

13 [Lavigne, H., D'Ortenzio, F., Migon, C., Claustre, H., Testor, P., d'Alcalá, M. R., Lavezza, R.,  
14 Houpert, L., and Prieur, L.: Enhancing the comprehension of mixed layer depth control on the  
15 Mediterranean phytoplankton phenology: Mediterranean Phytoplankton Phenology, J.  
16 \*Geophys. Res. Oceans\*, \*\*118\*\*, 3416–3430, <https://doi.org/10.1002/jgrc.20251>, 2013.](#)

17 Lazzari, Solidoro, C., Ibello, V., Salon, S., Teruzzi, A., Béranger, K., Colella, S., and Crise,  
18 A.: Seasonal and inter-annual variability of plankton chlorophyll and primary production in  
19 the Mediterranean Sea: a modelling approach, *Biogeosciences*, **9**, 217–233,  
20 <https://doi.org/10.5194/bg-9-217-2012>, 2012.

21 Lazzari, Solidoro, C., Salon, S., and Bolzon, G.: Spatial variability of phosphate and nitrate in  
22 the Mediterranean Sea: A modeling approach, *Deep Sea Res. Part Oceanogr. Res. Pap.*, **108**,  
23 39–52, <https://doi.org/10.1016/j.dsr.2015.12.006>, 2016.

24 Lazzari, Salon, S., Terzić, E., Gregg, W. W., D'Ortenzio, F., Vellucci, V., Organelli, E., and  
25 Antoine, D.: Assessment of the spectral downward irradiance at the surface of  
26 the Mediterranean Sea using the OASIM ocean-atmosphere radiative model,  
27 *Surface/Numerical Models/Mediterranean Sea/Air-sea fluxes/Oceanic ecosystems*,  
28 <https://doi.org/10.5194/os-2020-108>, 2020.

29 Lefèvre, N., Velede, D., Tyaquiça, P., Perruche, C., Diverrès, D., and Ibánhez, J. S. P.: Basin-  
30 Scale Estimate of the Sea-Air CO<sub>2</sub> Flux During the 2010 Warm Event in the Tropical North  
31 Atlantic, *J. Geophys. Res. Biogeosciences*, **124**, 973–986,  
32 <https://doi.org/10.1029/2018JG004840>, 2019.

33 Lellouche, Greiner, E., Le Galloudec, O., Garric, G., Regnier, C., Drevillon, M., Benkiran,  
34 M., Testut, C.-E., Bourdalle-Badie, R., Gasparin, F., Hernandez, O., Levier, B., Drillet, Y.,  
35 Remy, E., and Le Traon, P.-Y.: Recent updates to the Copernicus Marine Service global  
36 ocean monitoring and forecasting real-time 1/12° high-resolution system, *Ocean Sci.*, **14**,  
37 1093–1126, <https://doi.org/10.5194/os-14-1093-2018>, 2018.

38 Lellouche, J.-M., Le Galloudec, O., Drévillon, M., Régnier, C., Greiner, E., Garric, G., Ferry,  
39 N., Desportes, C., Testut, C.-E., Bricaud, C., Bourdallé-Badie, R., Tranchant, B., Benkiran,  
40 M., Drillet, Y., Daudin, A., and De Nicola, C.: Evaluation of global monitoring and  
41 forecasting systems at Mercator Océan, *Ocean Sci.*, **9**, 57–81, [https://doi.org/10.5194/os-9-57-](https://doi.org/10.5194/os-9-57-2013)  
42 2013, 2013.

Deleted: .

Deleted: <https://archimer.ifremer.fr/doc/00350/46121/>, last access:  
22 April 2020b, 2018

Deleted: .

Deleted: ..

Deleted: .

Deleted: (13),

Deleted: .

Deleted: (1),

Deleted: .

Deleted: .

Deleted: preprint,

Deleted: ..

Deleted: .

Deleted: (4),

Deleted: .

Deleted: (5),

Deleted: .

Deleted: (1),

1	Letelier, R. M., Karl, D. M., Abbott, M. R. and Bidigare, R. R.: Light driven seasonal	Deleted: .
2	patterns of chlorophyll and nitrate in the lower euphotic zone of the North Pacific	
3	Subtropical Gyre, <i>Limnol. Oceanogr.</i> , 49, 508–519, 2004.	Deleted: (2).
4	Lynch, D. R., McGillicuddy, D. J. and Werner, F. E.: Skill assessment for coupled	Deleted: .
5	biological/physical models of marine systems, <i>J. Mar. Syst.</i> , 1, 1–3, 2009.	Deleted: (76).
6	Macías, D., Stips, A. and Garcia-Gorritz, E.: The relevance of deep chlorophyll maximum in	Deleted: .
7	the open Mediterranean Sea evaluated through 3D hydrodynamic-biogeochemical coupled	
8	simulations, <i>Ecol. Model.</i> , 281, 26–37, 2014.	
9	Mignot, Claustre, H., Uitz, J., Poteau, A., D’Ortenzio, F. and Xing, X.: Understanding the	Deleted: .
10	seasonal dynamics of phytoplankton biomass and the deep chlorophyll maximum in	
11	oligotrophic environments: A Bio-Argo float investigation, <i>Glob. Biogeochem. Cycles</i> , 28,	Deleted: (8).
12	856–876, <a href="https://doi.org/10.1002/2013GB004781">https://doi.org/10.1002/2013GB004781</a> , 2014.	
13	Mignot, Ferrari, R. and Claustre, H.: Floats with bio-optical sensors reveal what processes	Deleted: .
14	trigger the North Atlantic bloom, <i>Nat. Commun.</i> , 9, <a href="https://doi.org/10.1038/s41467-017-02143-6">https://doi.org/10.1038/s41467-017-</a>	Deleted: (1).
15	02143-6, 2018.	
16	Mignot, A., Claustre, H., D’Ortenzio, F., Xing, X., Poteau, A. and Ras, J.: From the shape of	Deleted: .
17	the vertical profile of in vivo fluorescence to Chlorophyll-a concentration, <i>Biogeosciences</i> ,	
18	8, 2391–2406, <a href="https://doi.org/10.5194/bg-8-2391-2011">https://doi.org/10.5194/bg-8-2391-2011</a> , 2011.	Deleted: (8).
19	Mignot, A., D’Ortenzio, F., Taillandier, V., Cossarini, G. and Salon, S.: Quantifying	Deleted: .
20	Observational Errors in Biogeochemical-Argo Oxygen, Nitrate, and Chlorophyll <i>a</i>	
21	Concentrations, <i>Geophys. Res. Lett.</i> , 46, 4330–4337, <a href="https://doi.org/10.1029/2018GL080541">https://doi.org/10.1029/2018GL080541</a> ,	Deleted: (8).
22	2019.	
23	<a href="https://doi.org/10.5194/bg-12-3273-2015">Omand, M. M. and Mahadevan, A.: The shape of the oceanic nitracline, <i>Biogeosciences</i>, 12,</a>	
24	<a href="https://doi.org/10.5194/bg-12-3273-2015">3273–3287, https://doi.org/10.5194/bg-12-3273-2015, 2015.</a>	
25	Organelli, E., Bricaud, A., Antoine, D. and Matsuoka, A.: Seasonal dynamics of light	Deleted: .
26	absorption by chromophoric dissolved organic matter (CDOM) in the NW Mediterranean Sea	
27	(BOUSSOLE site), <i>Deep Sea Res. Part Oceanogr. Res. Pap.</i> , 91, 72–85, 2014.	
28	Organelli, E., Barbieux, M., Claustre, H., Schmechtig, C., Poteau, A., Bricaud, A., Boss, E.	Deleted: .
29	B., Briggs, N., Dall’Olmo, G. and d’Ortenzio, F.: Two databases derived from BGC-Argo	
30	float measurements for marine biogeochemical and bio-optical applications, <i>Earth Syst. Sci.</i>	
31	Data, 9, 861–880, 2017.	
32	Osman, M. B., Das, S. B., Trusel, L. D., Evans, M. J., Fischer, H., Grieman, M. M., Kipfstuhl,	Deleted: .
33	S., McConnell, J. R. and Saltzman, E. S.: Industrial-era decline in subarctic Atlantic	
34	productivity, <i>Nature</i> , 569, 551–555, <a href="https://doi.org/10.1038/s41586-019-1181-8">https://doi.org/10.1038/s41586-019-1181-8</a> , 2019.	Deleted: (7757).
35	Park, J.-Y., Stock, C. A., Yang, X., Dunne, J. P., Rosati, A., John, J. and Zhang, S.: Modeling	Deleted: .
36	Global Ocean Biogeochemistry With Physical Data Assimilation: A Pragmatic Solution to the	
37	Equatorial Instability, <i>J. Adv. Model. Earth Syst.</i> , 10, 891–906,	Deleted: (3).
38	<a href="https://doi.org/10.1002/2017MS001223">https://doi.org/10.1002/2017MS001223</a> , 2018.	
39	<a href="https://doi.org/10.1002/2009JC006800">Paulmier, A. and Ruiz-Pino, D.: Oxygen minimum zones (OMZs) in the modern ocean, <i>Prog.</i></a>	
40	<a href="https://doi.org/10.1002/2009JC006800"><i>Oceanogr.</i>, 80, 113–128, 2009.</a>	

1 [Plant, J. N., Johnson, K. S., Sakamoto, C. M., Jannasch, H. W., Coletti, L. J., Riser, S. C., and](#)  
2 [Swift, D. D.: Net community production at Ocean Station Papa observed with nitrate and](#)  
3 [oxygen sensors on profiling floats, \*Glob. Biogeochem. Cycles\*, 30, 859–879,](#)  
4 <https://doi.org/10.1002/2015GB005349>, 2016.

5 Richardson, K. and Bendtsen, J.: Vertical distribution of phytoplankton and primary  
6 production in relation to nutricline depth in the open ocean, *Mar. Ecol. Prog. Ser.*, 620, 33–46,  
7 <https://doi.org/10.3354/meps12960>, 2019.

8 Riley, G.: Factors Controlling Phytoplankton Populations on Georges Bank, *J. Mar. Res.*, 6,  
9 54–73, 1946.

10 [Roxy, M. K., Modi, A., Murtugudde, R., Valsala, V., Panickal, S., Prasanna Kumar, S.,](#)  
11 [Ravichandran, M., Vichi, M., and Lévy, M.: A reduction in marine primary productivity](#)  
12 [driven by rapid warming over the tropical Indian Ocean, \*Geophys. Res. Lett.\*, 43, 826–833,](#)  
13 <https://doi.org/10.1002/2015GL066979>, 2016.

14 [Salon, S., Cossarini, G., Bolzon, G., Feudale, L., Lazzari, P., Teruzzi, A., Solidoro, C., and](#)  
15 [Crise, A.: Novel metrics based on Biogeochemical Argo data to improve the model](#)  
16 [uncertainty evaluation of the CMEMS Mediterranean marine ecosystem forecasts, \*Ocean Sci.\*,](#)  
17 [15, 997–1022, https://doi.org/10.5194/os-15-997-2019](https://doi.org/10.5194/os-15-997-2019), 2019.

18 Sauzède, R., Bittig, H. C., Claustre, H., Pasqueron de Fommervault, O., Gattuso, J.-P.,  
19 Legendre, L., and Johnson, K. S.: Estimates of Water-Column Nutrient Concentrations and  
20 Carbonate System Parameters in the Global Ocean: A Novel Approach Based on Neural  
21 Networks, *Front. Mar. Sci.*, 4, <https://doi.org/10.3389/fmars.2017.00128>, 2017.

22 Schartau, M., Wallhead, P., Hemmings, J., Löptien, U., Kriest, I., Krishna, S., Ward, B. A.,  
23 Slawig, T., and Oschlies, A.: Reviews and syntheses: parameter identification in marine  
24 planktonic ecosystem modelling, *Biogeosciences*, 14, 1647–1701, [https://doi.org/10.5194/bg-](https://doi.org/10.5194/bg-14-1647-2017)  
25 [14-1647-2017](https://doi.org/10.5194/bg-14-1647-2017), 2017.

26 Schmechtig, C., Poteau, A., Claustre, H., D’Ortenzio, F., and Boss, E.: Processing bio-Argo  
27 chlorophyll-A concentration at the DAC level, Ifremer, <https://doi.org/10.13155/39468>, 2015.

28 Schmechtig, C., Claustre, H., Poteau, A., and D’Ortenzio, F.: Bio-Argo quality control  
29 manual for the Chlorophyll-A concentration, Ifremer, <https://doi.org/10.13155/35385>, 2018.

30 Schmidtko, S., Stramma, L., and Visbeck, M.: Decline in global oceanic oxygen content  
31 during the past five decades, *Nature*, 542, 335–339, <https://doi.org/10.1038/nature21399>,  
32 2017.

33 Schneider, B., Bopp, L., Gehlen, M., Segsneider, J., Frölicher, T. L., Cadule, P.,  
34 Friedlingstein, P., Doney, S. C., Behrenfeld, M. J., and Joos, F.: Climate-induced interannual  
35 variability of marine primary and export production in three global coupled climate carbon  
36 cycle models, *Biogeosciences*, 5, 597–614, <https://doi.org/10.5194/bg-5-597-2008>, 2008.

37 Séférian, R., Bopp, L., Gehlen, M., Orr, J. C., Ethé, C., Cadule, P., Aumont, O., Salas y  
38 Méliá, D., Voltaire, A., and Madec, G.: Skill assessment of three earth system models with  
39 common marine biogeochemistry, *Clim. Dyn.*, 40, 2549–2573,  
40 <https://doi.org/10.1007/s00382-012-1362-8>, 2013.

Deleted: (1),

Deleted: Roesler, C., Uitz, J., Claustre, H., Boss, E., Xing, X., Organelli, E., Briggs, N., Bricaud, A., Schmechtig, C., Poteau, A., D’Ortenzio, F., Ras, J., Drapeau, S., Haëntjens, N. and Barbioux, M.: Recommendations for obtaining unbiased chlorophyll estimates from in situ chlorophyll fluorometers: A global analysis of WET Labs ECO sensors, *Limnol. Oceanogr. Methods*, 15(6), 572–585, <https://doi.org/10.1002/lom3.10185>, 2017.

Deleted: .

Deleted: (2),

Deleted: Russell, J. L., Kamenkovich, I., Bitz, C., Ferrari, R., Gille, S. T., Goodman, P. J., Hallberg, R., Johnson, K., Khazmutdinova, K. and Marinov, I.: Metrics for the evaluation of the Southern Ocean in coupled climate models and earth system models, *J. Geophys. Res. Oceans*, 123(5), 3120–3143, 2018.

Deleted: .

Deleted: (4),

Deleted: .

Deleted: .

Deleted: (6),

Deleted: .

Deleted: .

Deleted: .

Deleted: .

Deleted: .

Deleted: (7641),

Deleted: .

Deleted: (2),

Deleted: .

Deleted: (9–10),

1	Skákala, J., Bruggeman, J., Brewin, R. J. W., Ford, D. A., and Ciavatta, S.: Improved	Deleted: .
2	Representation of Underwater Light Field and Its Impact on Ecosystem Dynamics: A Study in	
3	the North Sea, <i>J. Geophys. Res. Oceans</i> , 125, <a href="https://doi.org/10.1029/2020JC016122">https://doi.org/10.1029/2020JC016122</a> , 2020.	Deleted: (7).
4	<a href="#">Snowden, D., Tsonos, V. M., Handegard, N. O., Zarate, M., O'Brien, K., Casey, K. S.,</a>	
5	<a href="#">Smith, N., Sagen, H., Bailey, K., Lewis, M. N., and Arms, S. C.: Data Interoperability</a>	
6	<a href="#">Between Elements of the Global Ocean Observing System, <i>Front. Mar. Sci.</i>, 6, 442,</a>	
7	<a href="https://doi.org/10.3389/fmars.2019.00442">https://doi.org/10.3389/fmars.2019.00442</a> , 2019.	
8	Sosik, H. M.: Characterizing seawater constituents from optical properties, <i>Real-Time Coast.</i>	
9	<i>Obs. Syst. Ecosyst. Dyn. Harmful Algal Blooms</i> Ed. Babin M Roesler CS Cullen JJ	
10	UNESCO, 281–329, 2008.	
11	Steinacher, M., Joos, F., Frölicher, T. L., Bopp, L., Cadule, P., Cocco, V., Doney, S. C.,	Deleted: .
12	Gehlen, M., Lindsay, K., Moore, J. K., Schneider, B., and Segschneider, J.: Projected 21st	Deleted: (3).
13	century decrease in marine productivity: a multi-model analysis, <i>Biogeosciences</i> , 7, 979–	
14	1005, <a href="https://doi.org/10.5194/bg-7-979-2010">https://doi.org/10.5194/bg-7-979-2010</a> , 2010.	
15	Stow, C. A., Jolliff, J., McGillicuddy, D. J., Doney, S. C., Allen, J. I., Friedrichs, M. A. M.,	Deleted: .
16	Rose, K. A., and Wallhead, P.: Skill assessment for coupled biological/physical models of	Deleted: (1–2).
17	marine systems, <i>J. Mar. Syst.</i> , 76, 4–15, <a href="https://doi.org/10.1016/j.jmarsys.2008.03.011">https://doi.org/10.1016/j.jmarsys.2008.03.011</a> , 2009.	
18	Stramma, L., Johnson, G. C., Sprintall, J., and Mohrholz, V.: Expanding Oxygen-Minimum	Deleted: .
19	Zones in the Tropical Oceans, <i>Science</i> , 320, 655–658,	Deleted: (5876).
20	<a href="https://doi.org/10.1126/science.1153847">https://doi.org/10.1126/science.1153847</a> , 2008.	
21	Tagliabue, A., Bopp, L., Dutay, J.-C., Bowie, A. R., Chever, F., Jean-Baptiste, P., Bucciarelli,	Deleted: .
22	E., Lannuzel, D., Remenyi, T., Sarthou, G., Aumont, O., Gehlen, M., and Jeandel, C.:	Deleted: (4).
23	Hydrothermal contribution to the oceanic dissolved iron inventory, <i>Nat. Geosci.</i> , 3, 252–256,	
24	<a href="https://doi.org/10.1038/ngeo818">https://doi.org/10.1038/ngeo818</a> , 2010.	
25	Taylor, K. E.: Summarizing multiple aspects of model performance in a single diagram, <i>J.</i>	Deleted: (D7).
26	<i>Geophys. Res. Atmospheres</i> , 106, 7183–7192, <a href="https://doi.org/10.1029/2000JD900719">https://doi.org/10.1029/2000JD900719</a> , 2001.	
27	Teruzzi, A., Dobricic, S., Solidoro, C., and Cossarini, G.: A 3-D variational assimilation	Deleted: .
28	scheme in coupled transport-biogeochemical models: Forecast of Mediterranean	
29	biogeochemical properties: 3D-VAR IN BIOGEOCHEMICAL MODELS, <i>J. Geophys. Res.</i>	
30	<i>Oceans</i> , 119, 200–217, <a href="https://doi.org/10.1002/2013JC009277">https://doi.org/10.1002/2013JC009277</a> , 2014.	Deleted: (1).
31	Terzić, E., Lazzari, P., Organelli, E., Solidoro, C., Salon, S., D'Ortenzio, F., and Conan, P.:	Deleted: .
32	Merging bio-optical data from Biogeochemical-Argo floats and models in marine	
33	biogeochemistry, <i>Biogeosciences</i> , 16, 2527–2542, <a href="https://doi.org/10.5194/bg-16-2527-2019">https://doi.org/10.5194/bg-16-2527-2019</a> ,	Deleted: (12).
34	2019.	
35	Thierry, V. and Bittig, H.: Argo quality control manual for dissolved oxygen concentration,	
36	2018.	
37	Thierry, V., Bittig, H., Gilbert, D., Kobayashi, T., Kanako, S., and Schmid, C.: Processing	Deleted: .
38	Argo oxygen data at the DAC level, Ifremer, <a href="https://doi.org/10.13155/39795">https://doi.org/10.13155/39795</a> , 2018.	Deleted: ..

1 Tuan Pham, D., Verron, J., and Christine Roubaud, M.: A singular evolutive extended  
2 Kalman filter for data assimilation in oceanography, *J. Mar. Syst.*, 16, 323–340,  
3 [https://doi.org/10.1016/S0924-7963\(97\)00109-7](https://doi.org/10.1016/S0924-7963(97)00109-7), 1998.

4 Vichi, M., Lovato, T., Lazzari, P., Cossarini, G., Gutierrez, E., Mattia, G., Masina, S.,  
5 McKiver, W. J., Pinardi, N., and Solidoro, C.: The Biogeochemical Flux Model (BFM):  
6 Equation Description and User Manual, BFM version 5.1, BFM Report series N. 1, Release  
7 1.1, July 2015, Bologna, Italy, 104pp, 2015.

8 Wanninkhof, R.: Relationship between wind speed and gas exchange over the ocean revisited:  
9 Gas exchange and wind speed over the ocean, *Limnol. Oceanogr. Methods*, 12, 351–362,  
10 <https://doi.org/10.4319/lom.2014.12.351>, 2014.

11 Ward, B. A., Friedrichs, M. A. M., Anderson, T. R., and Oschlies, A.: Parameter optimisation  
12 techniques and the problem of underdetermination in marine biogeochemical models, *J. Mar.*  
13 *Syst.*, 81, 34–43, <https://doi.org/10.1016/j.jmarsys.2009.12.005>, 2010.

14 Williams, R. G. and Follows, M. J.: *Ocean dynamics and the carbon cycle: Principles and*  
15 *mechanisms*, Cambridge University Press, 2011.

16 Wong, Keeley, Robert, Carval, Thierry, and Argo Data Management Team,: *Argo Quality*  
17 *Control Manual for CTD and Trajectory Data*, <https://doi.org/10.13155/33951>, 2015.

18 [Yang, B., Fox, J., Behrenfeld, M. J., Boss, E. S., Haëntjens, N., Halsey, K. H., Emerson, S.](#)  
19 [R., and Doney, S. C.: In Situ Estimates of Net Primary Production in the Western North](#)  
20 [Atlantic With Argo Profiling Floats, \*J. Geophys. Res. Biogeosciences\*, 126,](#)  
21 <https://doi.org/10.1029/2020JG006116>, 2021.

22 ▲

**Deleted:** .

**Deleted:** (3–4),

**Deleted:** .

**Deleted:** ..

**Deleted:** (6),

**Deleted:** .

**Deleted:** (1–2),

**Deleted:** ..

**Deleted:** .

**Deleted:** Xing, X., Claustre, H., Blain, S., D’Ortenzio, F., Antoine, D., Ras, J. and Guinet, C.: Quenching correction for in vivo chlorophyll fluorescence acquired by autonomous platforms: A case study with instrumented elephant seals in the Kerguelen region (Southern Ocean): Quenching correction for chlorophyll fluorescence, *Limnol. Oceanogr. Methods*, 10(7), 483–495, <https://doi.org/10.4319/lom.2012.10.483>, 2012.

**Formatted:** Font colour: Text 1

**Page 15: [1] Deleted    Alexandre Mignot    01/10/2021 16:10:00**

▼

**Page 15: [2] Deleted    Alexandre Mignot    01/10/2021 16:10:00**

▼

**Page 15: [3] Deleted    Alexandre Mignot    01/10/2021 16:10:00**

▼

**Page 15: [4] Deleted    Alexandre Mignot    01/10/2021 16:10:00**

▼

**Page 30: [5] Formatted    Alexandre Mignot    01/10/2021 16:10:00**

Font: Not Bold, Font colour: Text 1

**Page 30: [5] Formatted    Alexandre Mignot    01/10/2021 16:10:00**

Font: Not Bold, Font colour: Text 1

**Page 49: [6] Deleted    Alexandre Mignot    01/10/2021 16:10:00**

▼

**Page 49: [7] Deleted    Alexandre Mignot    01/10/2021 16:10:00**

▼